AMMRC TR80-30

TRANSPIRATION-COOLED NOSETIP DEVELOPMENT

June 1980

N. C. CAMPBELL
G. F. PITTINATO
M. T. MARTIN

McDonnell Douglas Astronautics Company
5301 Bolsa Avenue
Huntington Beach, California 92647

FINAL REPORT   DAA G46-78-C-0034

A

Prepared for

ARMY MATERIALS AND MECHANICS RESEARCH CENTER
Watertown, Massachusetts 02172

80 8 14 036

SECURITY CLASSIFICATION OF THIS PAGE (When Data Entered)

REPORT DOCUMENTATION PAGE	READ INSTRUCTIONS BEFORE COMPLETING FORM

1. REPORT NUMBER	2. GOVT ACCESSION NO.	3. RECIPIENT'S CATALOG NUMBER
AMMRC TR8030	AD-A087 837	

4. TITLE (and Subtitle)	5. TYPE OF REPORT & PERIOD COVERED
Transpiration-Cooled Nosetip Development	Final Report, July 1978 to January 1980
	6. PERFORMING ORG. REPORT NUMBER

7. AUTHOR(s)	8. CONTRACT OR GRANT NUMBER(s)
N. C. Campbell M. T. Martin G. F. Pittinato	DAAG46-78-C-0034

9. PERFORMING ORGANIZATION NAME AND ADDRESS	10. PROGRAM ELEMENT, PROJECT, TASK AREA & WORK UNIT NUMBERS
McDonnell Douglas Astronautics Company 5301 Bolsa Avenue Huntington Beach, CA 92647	D/A Proj: 1W162113A661 AMCMS Code: 612113.11.07000

11. CONTROLLING OFFICE NAME AND ADDRESS	12. REPORT DATE
Army Materials & Mechanics Research Center Watertown, MA 02172	June 1980
	13. NUMBER OF PAGES

14. MONITORING AGENCY NAME & ADDRESS(if different from Controlling Office)	15. SECURITY CLASS. (of this report)
	Unclassified
	15a. DECLASSIFICATION/DOWNGRADING SCHEDULE N/A

16. DISTRIBUTION STATEMENT (of this Report)

Approved for public release; distribution unlimited

17. DISTRIBUTION STATEMENT (of the abstract entered in Block 20, if different from Report)

18. SUPPLEMENTARY NOTES

19. KEY WORDS (Continue on reverse side if necessary and identify by block number)

Nosetips	Fabrication
Cooling	Interceptors
Transpiration	

20. ABSTRACT (Continue on reverse side if necessary and identify by block number)

A 316L stainless steel transpiration-cooled nosetip for a high-performance missile system was designed and fabricated using powder metallurgy techniques. The geometry of the nosetip was established, and permeability requirements were analytically defined. A parametric study of subscale billets determined permeability as a function of powder size and sintering temperature. Near-net-shape billets were fabricated, and machining procedures for the porous material were established. A comparison was made between the actual and calculated gas

20. Abstract (Continued)

flow through the nosetip over its entire surface. Two nosetips were success-
fully tested in a thermal environment approximating the flight environment
at the Edward's Air Force Base Rocket Propulsion Laboratory (RPL). Tests were
conducted at 0-degree and 10-degree angles of attack.

FOREWORD

This final Technical Report was prepared by McDonnell Douglas Astronautics Company, Huntington Beach, California under Contract Number DAAC46-78-C-0034 for the Army Materials and Mechanics Research Center (AMMRC), Watertown, Massachusetts. The work is part of the program on Development of Hardened ABM Materials, Mr. John Dignam, Program Manager. The AMMRC Technical Supervisor is Mr. Lewis R. Aronin.

The program at McDonnell Douglas Astronautics Company was under the direction of Dr. N. C. Campbell, Program Manager, with Mr. G. F. Pittinato as Principal Investigator, and Mr. M. T. Martin as Coinvestigator. Mr. G. P. Johnson conducted the ground test at the Air Force Rocket Propulsion Laboratory. Appreciation is expressed to Mr. S. Miller for his assistance in machining the nosetips and the following companies for their participation in this program: Vac-Hyd Processing Corporation, EDM Laboratories, Radcliffe Engineering, Acurex, Hoeganaes, and the Air Force Flight Dynamics Laboratory.

iii

CONTENTS

v

MCDONNELL DOUGLAS

Section 1
INTRODUCTION

Endohoming interceptor missiles utilizing optical sensors have been shown to require gaseous-transpiration-cooled nosetips in order to avoid boundary layer contamination above the sensor window which would result in sensor performance degradation. The requirement of a contaminant-free boundary layer for optical transmission limits the selection of coolant to helium or nitrogen. A typical endohoming interceptor with a sensor window and transpiration-cooled nosetip is schematically shown in Figure 1-1.
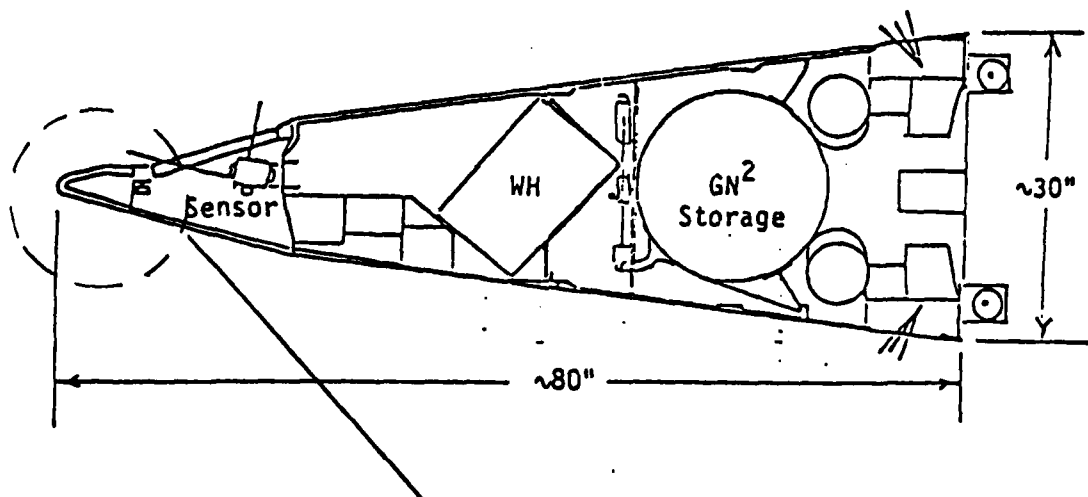
Figure 1-1. Typical Endohoming Interceptor

A drawing of the 3/4-scale nosetip that was used in the Endohoming Technology Ground Test Program in October, 1977 (BMDATC contract DASG60-76-C-0031) is shown in Figure 1-2. Current endohoming nosetip specifications include a hemispherical tip with a one inch nose radius followed by a conical section of up to 7.5 inches in length with a semivertex angle of 15 degrees. The flat optical window immediately aft of the nosetip may subtend a 120 degree circumferenced angle, thus necessitating a flat region on the nosetip to permit forward viewing.

1
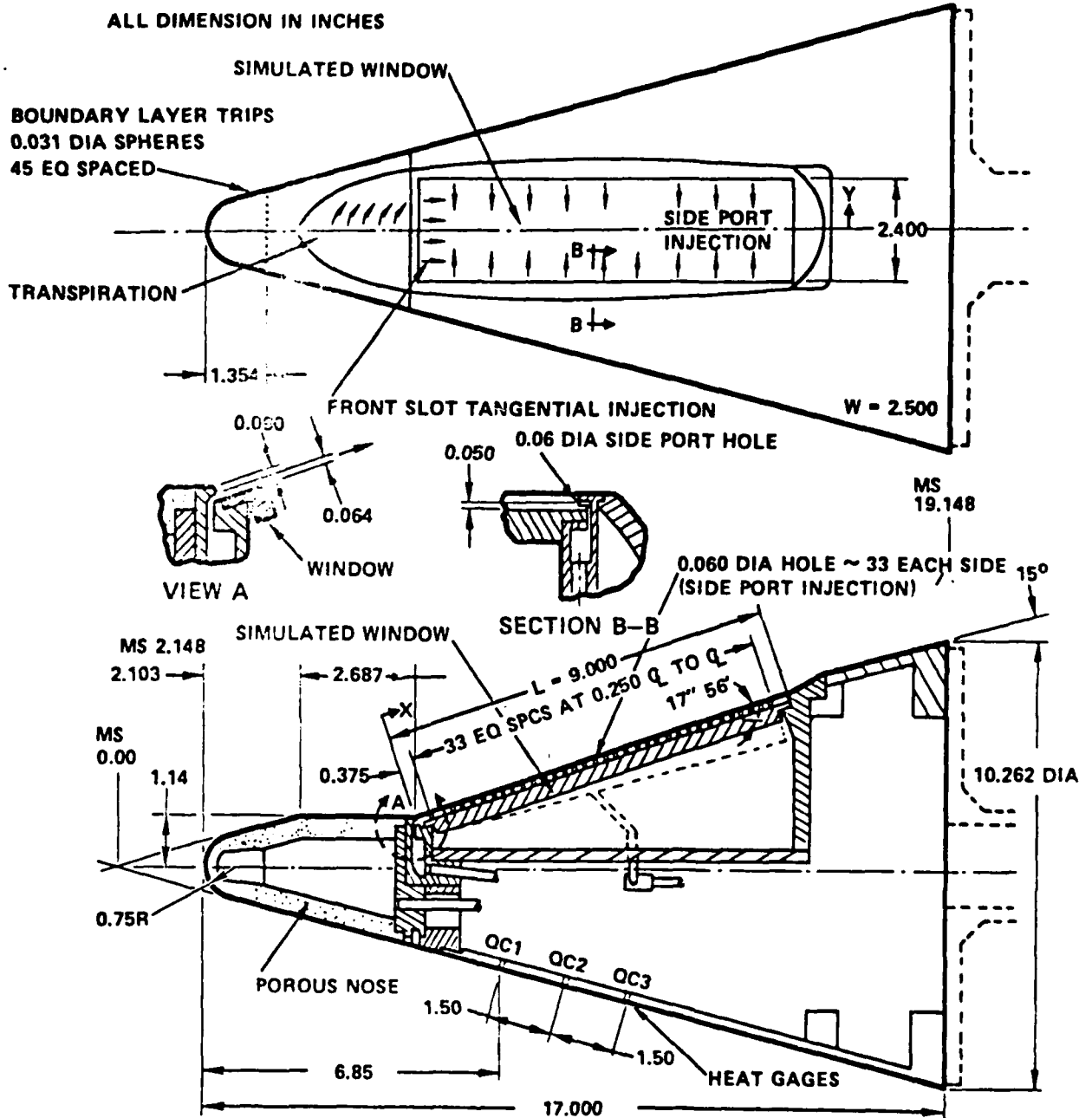
Figure 1-2. Sketch of Endohoming Model Showing Coolant Injection Method

Previous MDAC attempts to fabricate 3/4-size porous stainless steel nosetips by powder metallurgy resulted in a high scrap rate because of cracks that formed in the sintered billets. These cracks were believed to be related to the powder compaction and sintering processes. Thus it was the primary objective of the present program to study the feasibility of developing a full-scale, porous stainless steel, gas-transpiration-cooled nosetip for an endohoming interceptor missile. The development program consisted of an analytical effort to define the nosetip configuration and coolant requirements, a material development effort to obtain reproducible nosetips, and a ground test of the nosetips in the thermodynamic environment of a rocket exhaust facility.

MCDONNELL DOUGLAS

Section 2
NOSETIP DEFINITION

The definition of coolant requirements for a transpiration nosetip
consists of three steps: (1) calculation of the heating and pressure distribu-
tion on the nosetip given the vehicle altitude, velocity, angle-of-attack, and
external nosetip shape; (2) calculation of the theoretical coolant flux
(lb/ft^2-sec) required at each point on the nosetip to maintain a specified
surface temperature; and (3) calculation of the coolant flux distribution
about the nosetip resulting from the coolant flow across the porous nosetip
under a local pressure gradient.

At some point on the nosetip surface an exact match between coolant
delivered across the porous media and theoretically required coolant exists.
At all other points on the nosetip, the coolant delivered through the nosetip
meets or exceeds the required amount.

2.1 AERODYNAMIC HEATING

Aerodynamic heating and pressure distribution about the nosetip were cal-
culated employing MDAC computer program H586. Heat transfer rates were com-
puted using the following methods:

(1) Stagnation point -- Hoshizaki[2-1]
(2) Other nosetip points
     laminar flow -- Lees[2-2]
     turbulent flow -- Detra and Hidalgo[2-3]

Transition was conservatively assumed to occur at a Reynolds number of 100.
Thus, turbulent flow was predicted for all but the immediate vicinity of the
stagnation point. Output of the computer program included the aerodynamic heat
transfer coefficient as well as recovery and wall enthalpies and local surface
pressure for various specified locations about the nosetip as a function of
altitude, velocity, and angle-of-attack. This data was used to calculate theo-
retical coolant flux requirements. The theoretical coolant flux is that flux
which will maintain the nosetip surface temperature at a selected value.

5

2.2 THEORETICAL COOLANT REQUIREMENT

The effectiveness of transpiration as a cooling mechanism arises from two considerations: (1) the coolant's ability to absorb energy as it passes through the matrix and into the boundary layer, and (2) the reduction of the heat flux reaching the surface by an alteration of the properties of the boundary layer.

To illustrate these points, consider the energy balance illustrated in the adjoining sketch.
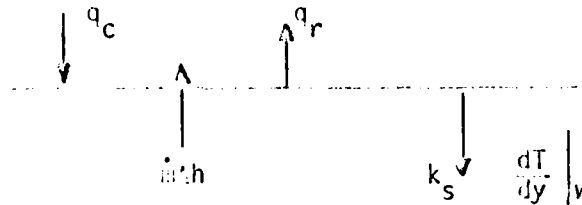
For steady state,

$$q_c - q_r = k_s \left. \frac{dT}{dy} \right|_w - \dot{m}\Delta h \qquad \text{Equation 2-1}$$

where

q_c = convective heat flux at the surface including the effects of blowing.

q_r = net radiation from the surface (neglecting any gas radiation)

$k_s \left. dT/dy \right|_w$ = energy conducted into the surface

h = energy absorbed by the coolant per lb. of coolant

m = mass flux of coolant

Let us now consider each of the terms in Equation 2-1.

The convective heat flux to a surface in the absence of blowing can be written

$$q_o = h_o \left(T_e + r \frac{U_e^2}{2C_p} - T_w \right) \qquad \text{Equation 2-2}$$

$$= \frac{h_o}{C_p} \left(C_p T_e + r \frac{U_e^2}{2} - C_p T_w \right)$$

6

where

h_o = heat transfer coefficient

r = recovery factor

Equation 2-2 can be written in terms of enthalpies as

$$\dot{q}_o = N_{c_o} (H_r - H_w)$$ Equation 2-3

where N_{c_o} = h/C_p = $\rho_e u_e St_o$

H_r = recovery enthalpy

H_w = surface enthalpy

St_o = no blowing Stanton number

In the case where blowing is present, Equation 2-3 can be assumed to take the form

$$q_c = N_{c_o} (\frac{N_c}{N_{c_o}}) (H_r - H_w) = N_c (H_r - H_w)$$ Equation 2-4

where N_c/N_{c_o} represents the reduction in the heat transfer coefficient due to the alteration of the boundary layer properties caused by the injectant fluid.

The main difficulty of the transpiration problem resides in an accurate description of the dependence of Stanton number (or N_c/N_{c_o}) upon coolant flow rates, coolant properties, and aerodynamic parameters. Correlations for the determination of N_c/N_{c_o} have been obtained by Arne[2-4] and used in the MARCAS[2-5] program. These correlations will be used in the present report.

For the injection of foreign gas into air, the correlation has been written in terms of the specific heat ratio

$$(\frac{C_{p_i}}{C_{p_e}})^n$$

where C_{p_i} is the specific heat for the injectant at the surface temperature and C_{p_e} is the specific heat at the outer edge of the boundary layer.

7

The correlation for Nc/Nc_o is written as (2-2)

$$\frac{N_c}{N_{c_o}} = 1 - L \frac{\dot{m}}{N_{c_o}}$$

Equation 2-5

where L is a function of both the parameter $\dot{m}/Nc_o$ and the specific heat ratio. For laminar flow

$$L_L = 0.68 \left(\frac{\bar{c}_p}{c_{p_e}}\right)^{0.4} - 0.08 \left(\frac{\bar{c}_p}{c_{p_e}}\right)^{0.4} \frac{\dot{m}}{N_{c_o}}$$

Equation 2-6

while for turbulent flow

$$L_T = 0.36 \left(\frac{\bar{c}_p}{c_{p_e}}\right)^{0.8} - 0.0649 \left(\frac{\bar{c}_p}{c_{p_e}}\right)^{1.6} \frac{\dot{m}}{N_{c_o}}$$

Equation 2-7

$$+ 0.0078 \left(\frac{\bar{c}_p}{c_{p_e}}\right)^{2.4} \left(\frac{\dot{m}}{N_{c_o}}\right)^2 - 0.00095 \left(\frac{\bar{c}_p}{c_{p_e}}\right)^{3.2} \left(\frac{\dot{m}}{N_{c_o}}\right)^3$$

$$+ 0.000085 \left(\frac{\bar{c}_p}{c_{p_e}}\right)^{4.0} \left(\frac{\dot{m}}{N_{c_o}}\right)^4 - 0.000003 \left(\frac{\bar{c}_p}{c_{p_e}}\right)^{4.8} \left(\frac{\dot{m}}{N_{c_o}}\right)^5$$

2.3 COOLANT ENERGY ABSORPTION

The term ΔH in Equation 2-1 represents the enthalpy change of the coolant gas between its storage condition and condition at the surface. This enthalpy change includes not only the sensible heat and heat of vaporization, but also the effects of the heat of reaction between the coolant gas and the freestream air, if any.

For a non-reacting case in which the coolant is stored as a gas:

$$\boxed{(N_{c_o} - L\dot{m}) \Delta H - \sigma \varepsilon T_2^4 = \dot{m}[\lambda + c_{p_v}(T_2 - T_1)]}$$

Equation 2-8

Theoretical coolant fluxes are calculated employing Equation 2-8 together with Equations 2-6 and 2-7.

8

2.4 COOLANT FLOW IN A POROUS MEDIA

The permeability of a porous material is a measure of its fluid conductivity.[2-6] A coefficient, K, which characterizes material permeability was originally defined by Darcy in the following equation for one-dimensional flow of fluids through a porous medium:

$$G = - K \frac{\rho}{\mu} \frac{dP}{dx} \qquad \text{Equation 2-9}$$

where p = pressure (lb/in^2)

x = thickness (in)

μ = viscosity $(lb\text{-}sec)/in^2$

ρ = density (lb_m/in^3)

G = mass flux $(lb_m/in^2\text{-}sec)$

K = Darcy's constant, a material property expressed in units of in^2

Equation 2-9 states that the mass flux of gas passing through a permeable material is proportional to the pressure gradient, and assumes that laminar-viscous flow exists through the matrix. This assumption is valid only for very low flow rates and a single permeability constant, K, can be calculated to characterize the material's permeability in this flow regime.

For low flow rates Equation 2-9 can be integrated for isothermal gaseous flow to give

$$G = \frac{K \Delta (P^2)}{2ZRTL\mu} \qquad \text{Equation 2-10}$$

where

$\Delta(P^2) = P^2$ upstream $- P^2$ downstream = upstream pressure squared minus downstream pressure squared

T = coolant gas temperature

Z = compressibility factor

L = specimen thickness

R = gas constant

G = coolant flux

μ = coolant (gas) viscosity

9

2.5 CALCULATIONAL PROCEDURE

In order to determine the actual coolant flux about the nosetip, the following procedure is adopted for a single permeability nosetip:

A. Determine heat transfer and pressure distribution about the nosetip with computer program H586.

B. Determine theoretical mass flux distribution using the equations previously described.

C. For a selected permeability, determine the critical point on the hemisphere or cone where the delivered flux will just match the theoretical flux required. This point is usually the point of maximum heating on the hemisphere or the cone. (Nosetip thickness must be considered in this determination.)

D. Using Equation 2-10, the specified permeability, the theoretical coolant flux and the nosetip thickness at the critical location on the nosetip, calculate the internal nosetip pressure.

E. Using the determined internal nosetip pressure, Equation 2-10, and the various surface pressures and nosetip thicknesses, calculate the actual coolant flux distribution about the nosetip.

F. Integrate the flux distribution over the nosetip surface area to obtain coolant flow rate for the specified permeability.

The above procedure, slightly modified, was used to evaluate dual permeability nosetips. A dual permeability nosetip is one in which two permeabilities are used; one for the hemisphere and a second for the cone. Dual permeability nosetips have the advantage of using less coolant than single permeability tips. The procedure for evaluating dual permeability nosetips begins with steps A and B above. Step C, however, is as follows: for a selected cone permeability, determine the critical point on the cone where the delivered flux will just match the theoretical flux required. Since the cone has a constant wall thickness, this point will be the point of maximum heating rate. Calculate the internal nosetip pressure corresponding to this location. Next determine the hemisphere permeability using the calculated internal pressure and the critical location on the hemisphere. Steps D through F are the same for a single permeability except that a different permeability is used in each of the hemisphere and cone calculations.

2.6 NOSETIP PERMEABILITY SELECTION

MDAC has defined permeabilities, coolant (nitrogen) flow rates to maintain a 340°F wall temperature and internal nosetip pressures in this program for three endohoming interceptor missions (50 Kft intercept at 10 Kft/sec, 100 Kft intercept at 10 ft/sec corresponding to a Minuteman defense, and 100 Kft intercept at 20 Kft/sec corresponding to a SAC defense). The hemisphere internal geometry was that found optimum in previous MDAC reentry vehicle transpiration nosetip applications with water coolant. Cone thickness was set at 0.6 inch.

Table 2-1 summarizes the results. Cases 1 through 4 and 7 through 9 show that nosetips optimized for each particular angle of attack show a constant internal pressure with angle of attack (α) because the pressure is set by the geometry and permeability of the hemisphere. The coolant rate increases with α because the cone windward ray is hotter at angle of attack. Higher cone permeability requirements (less flow resistance) reflect the need for higher coolant rates on the cone at angle of attack.

An operational nosetip will be flown over a range of angles of attack during a mission. Thus the $\alpha = 15^\circ$ nosetip was applied to the $\alpha = 0^\circ$ environment (case 5) and the $\alpha = 0^\circ$ nosetip was applied to the $\alpha = 15^\circ$ environment (case 6). Case 5 shows a significant penalty in coolant rate over the optimized $\alpha = 0^\circ$ case (case 1) and more significantly to the optimized $\alpha = 15^\circ$ nosetip applied at $\alpha = 15^\circ$ (case 4). It should be noted that the amount of coolant stored on board the interceptor must correspond to the worst case. Case 6 shows less coolant penalty but moderate increase in internal pressure.

Cases 10 and 11 show the same trends as cases 5 and 6, respectively, but at 100 Kft intercept altitude.

The permeabilities used in the above analyses are sufficiently tight that external pressure distribution a.ong and about the cone do not affect the flow distribution. (Flow rate is proportional to internal pressure squared minus external pressure squared.) This greatly simplifies design calculations.

Cases 12 and 13 were done to show the impact of an order of magnitude "looser nosetip", i.e., permeability equals 1×10^{-10} in^2. Since $\alpha = 15^\circ$ is the worse case environment, runs were made only at this condition. Comparison of cases 12 with 4 for permeability optimized to the $\alpha = 15^\circ$ environment and

11

Table 2-1. Permeability Selection Tradeoffs (Cases 1 Through 15)

Case	Altitude Kft	Velocity Kft/sec	Angle of Attack Degrees	Hemisphere Permeability In²	Cone Permeability In²	Internal Pressure, psi	Coolant Rate lb/sec
1	50	10	0	10^{-11}	10^{-11}	1138	1.43
2			5	10^{-11}	1.4×10^{-11}	1138	1.89
3			10	10^{-11}	1.7×10^{-11}	1138	2.23
4			15	10^{-11}	2.2×10^{-11}	1138	2.55
5	50	10	0	10^{-11}	2.2×10^{-11}	1138	2.92
6	50	10	15	10^{-11}	10^{-11}	1686	2.76
7	100	10	0	10^{-11}	10^{-11}	469	0.232
8			10	10^{-11}	1.63×10^{-11}	469	0.336
9			15	10^{-11}	2×10^{-11}	469	0.399
10	100	10	0	10^{-11}	2×10^{-11}	469	0.430
11	100	10	15	10^{-11}	10^{-11}	664	0.430
12	50	10	15	10^{-10}	1.89×10^{-10}	404	2.55
13	50	10	15	10^{-10}	10^{-10}	532	2.73
14	100	20	15	10^{-10}	1.68×10^{-10}	323	1.66
15	100	20	15	10^{-10}	10^{-10}	418	1.76

cases 13 and 6 for the single permeability nosetips show a reduction in internal pressure and no change in coolant rate. Thus coolant rate is uneffected by permeability change because the cone contribution to coolant rate is set to the same value by internal pressure selection and the relatively small surface area of the hemisphere does not contribute significantly to total coolant.

As was the case with the 1×10^{-11} in^2 permeability, coolant distribution along and about the cone was nearly constant, thus simplifying design.

Finally, the coolant rate and internal pressure were calculated for a high velocity environment representative of a possible SAC defense (100 Kft intercept at 20 Kft/sec). This is a non-stressing environment compared to the 50 Kft intercept/10 Kft/sec velocity case.

Figures 2-1 to 2-5 show coolant distributions, total coolant rate and required internal pressure for the conditions studied. Asterisks denote the point(s) on the nosetip where delivered coolant flux matches the thermodynamically required coolant flux. The delivered flux exceeds the required flux at all other points.

Previous experience has shown that permeabilities tighter than 1×10^{-12} in^2 are difficult to achieve. Parts sintered to achieve this permeability often become fully densified (no flow). Experience also shows that permeabilities looser than 1×10^{-9} in^2 are low in strength with a rough surface finish which increases boundary layer heating. Therefore, the range of permeabilities considered was limited to these values.

Cases 16-21 were run assuming a single permeability for both hemisphere and cone since the cases run earlier showed no significant benefit of using dual rather than single permeability. Table 2-2 tabulates the results and Figure 2-6 shows the results graphically together with the single permeability cases from Table 2-1. It is seen that at permeabilities between 3×10^{-10} and 1×10^{-9} in^2 flow rate increases rapidly with permeability.

At all single permeabilities equal to or less than 3×10^{-10} in^2, the nosetip location where the theoretical and actual coolant flux are equal was on the cone. At single permeabilities greater than 3×10^{-10} in^2, the critical point was on the hemisphere. When the critical point occurs on the cone, little excess coolant is used on the cone but coolant wastage occurs on the rela-
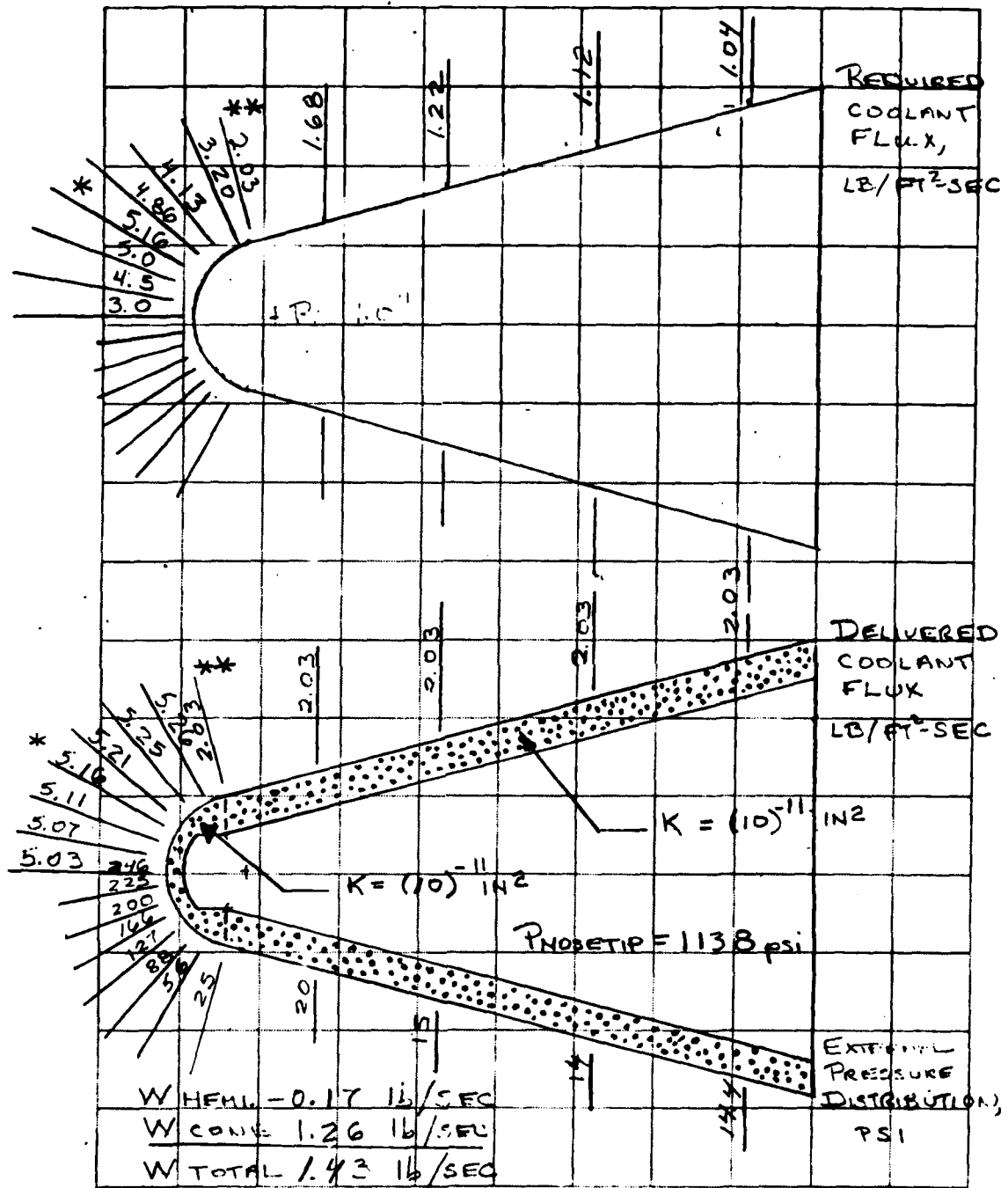
13

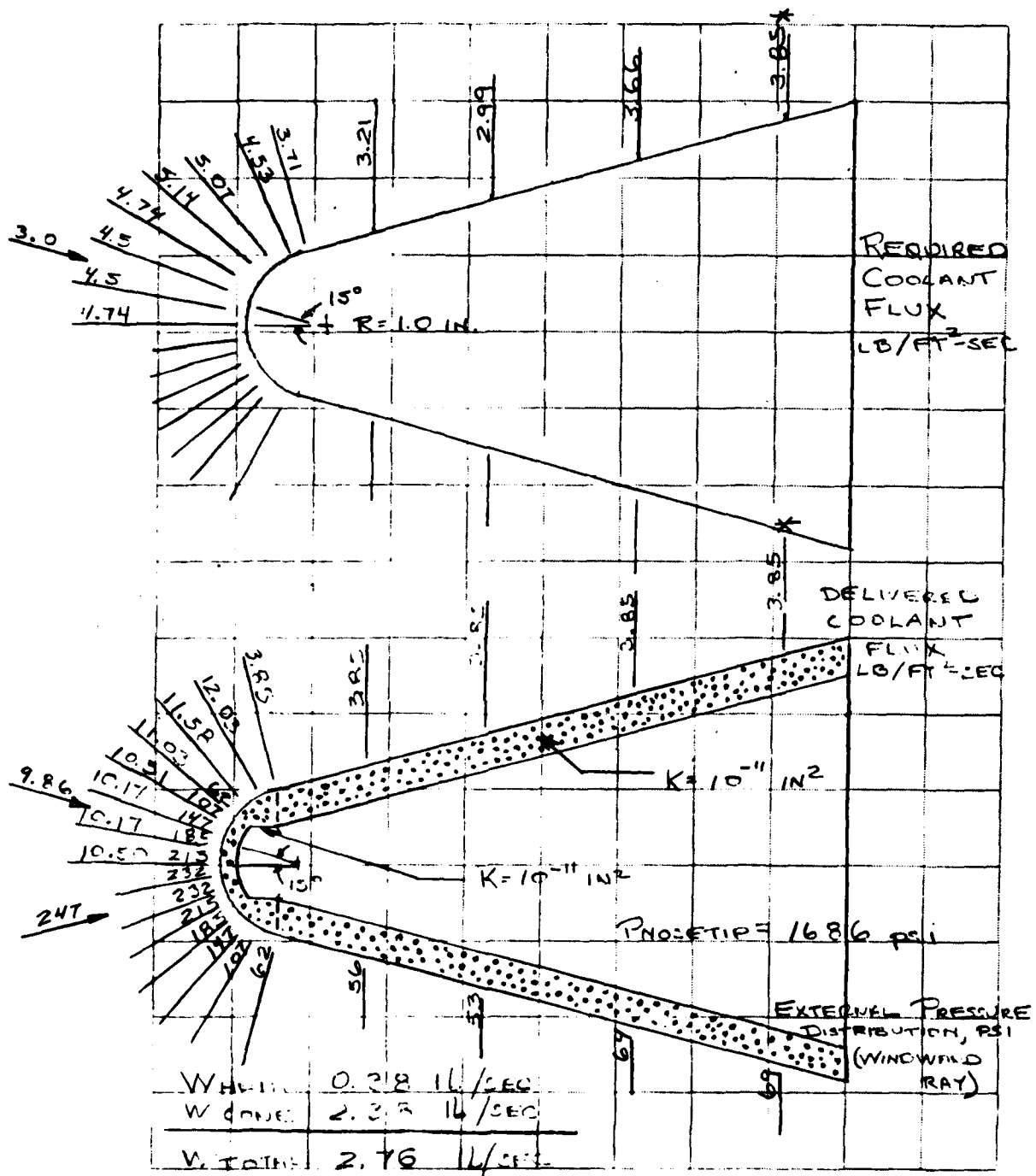Figure 2-1. Case 1, $K = 10^{-11}$ in^2, Angle of Attack = 0 Deg

MCDONNELL DOUGLAS

Figure 2-2.   Case 6, $K = 10^{-11}$ in^2, Angle of Attack = 15 Deg

MCDONNELL DOUGLAS
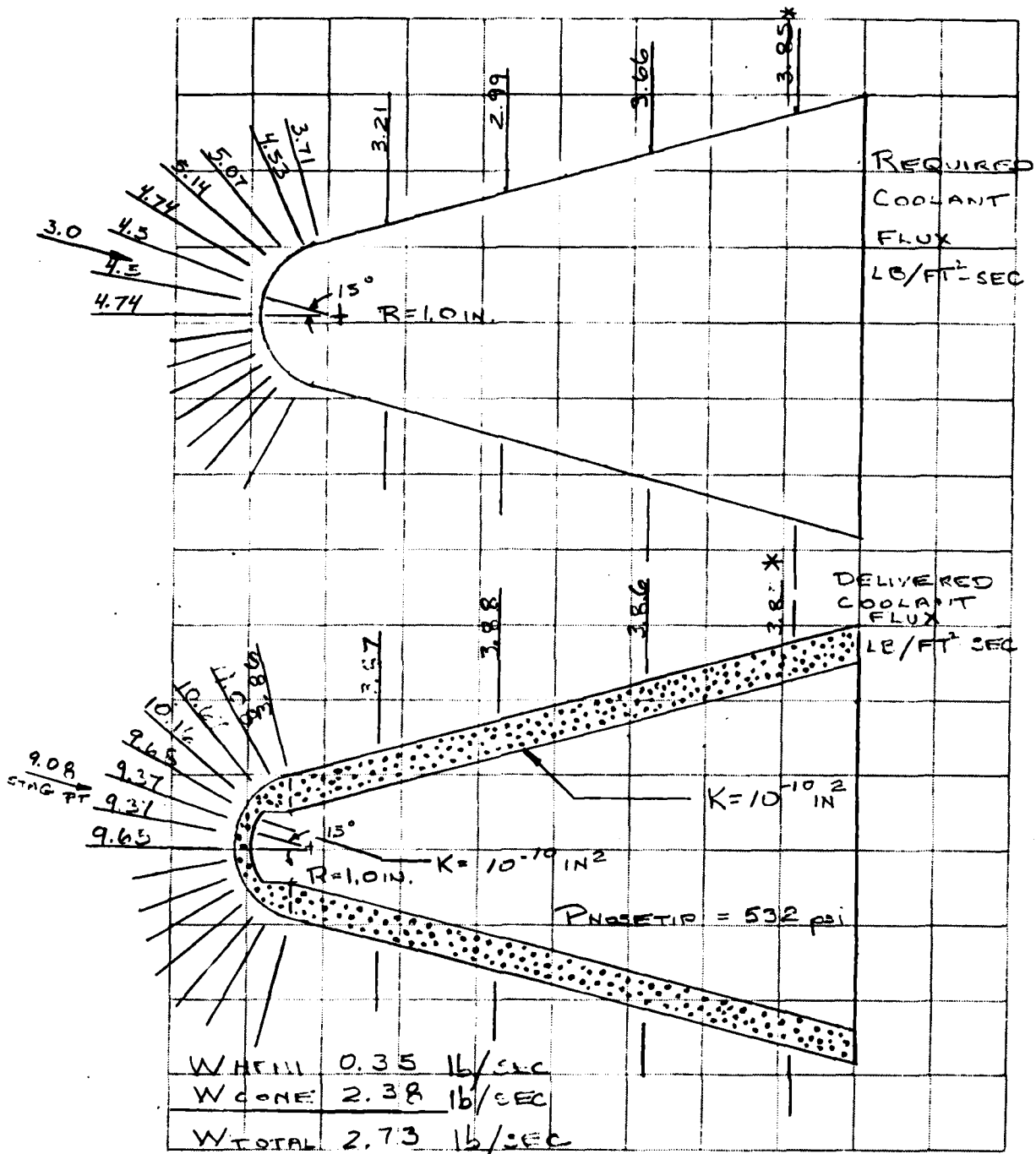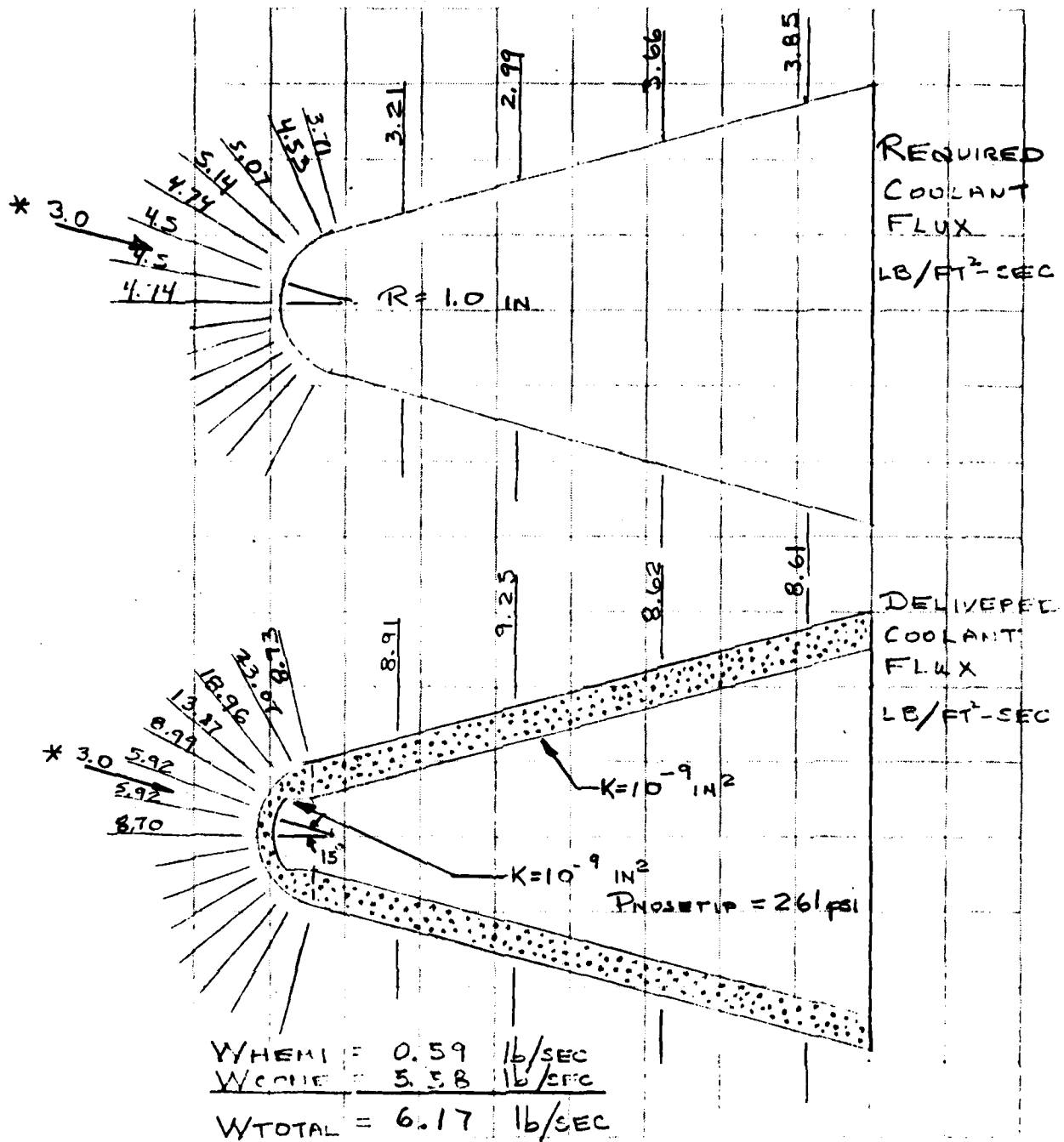
Figure 2-3. Case 13, $K = 10^{-10}$ in^2, Angle of Attack = 15 Deg

Figure 2-4.   Case 21, K = 10^{-9} in^2, Angle of Attack = 15 Deg

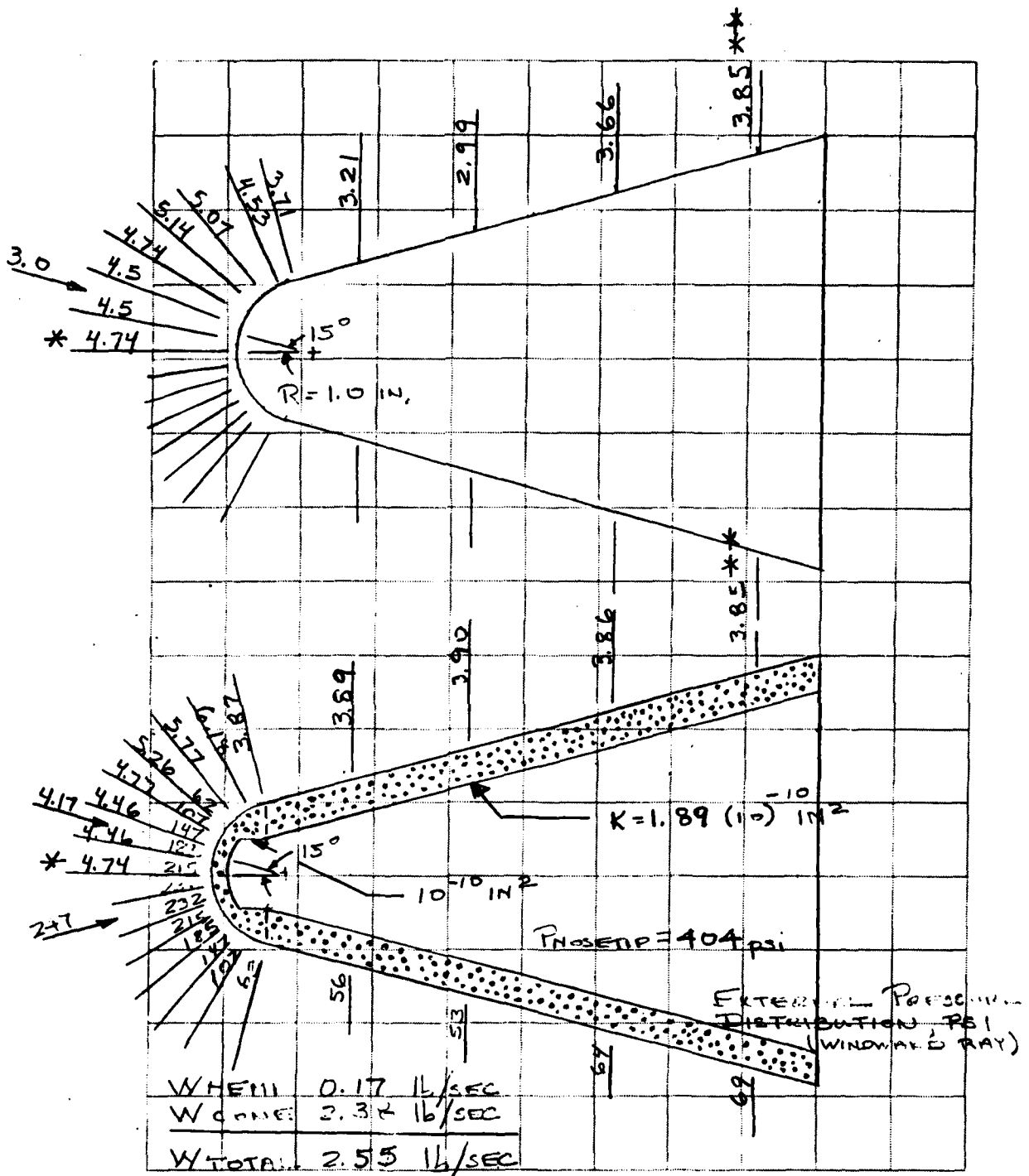Figure 2-5.   Case 12, Dual K, Angle of Attack = 15 Deg

MCDONNELL DOUGLAS

Table 2-2. Permeability Selection Tradeoffs (Cases 16-24)

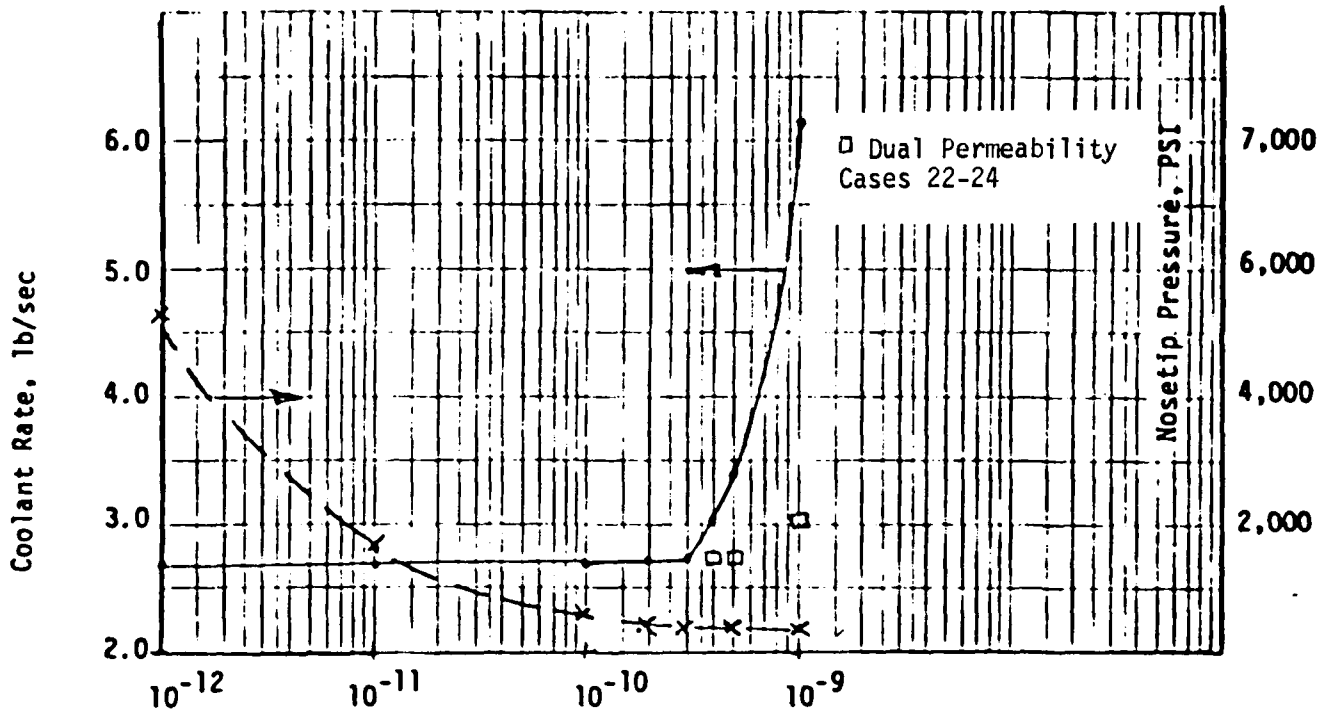| Case	Altitude (kft)	Velocity (kft/sec)	Angle of Attack (degree)	Hemisphere Permeability (in²)	Cone Permeability (in²)	Internal Pressure (psi)	Coolant Rate (lb/sec)
16	50	10	15	1×10^{-12}	1×10^{-12}	5324	2.72
17	50	10	15	2×10^{-10}	2×10^{-10}	382	2.72
18	50	10	15	3×10^{-10}	3×10^{-10}	315	2.66
19	50	10	15	4×10^{-10}	4×10^{-10}	285	2.99
20	50	10	15	5×10^{-10}	5×10^{-10}	275	3.43
21	50	10	15	1×10^{-9}	1×10^{-9}	261	6.17
22	50	10	15	4×10^{-10}	3.53×10^{-10}	285	2.68
23	50	10	15	5×10^{-10}	4×10^{-10}	275	2.72
24	50	10	15	1×10^{-9}	4.47×10^{-9}	261	3.06

Figure 2-6. Impact of Permeability on Coolant Rate and Pressure

tively smaller hemispherical area. The result is a good match between theoretical and delivered coolant flow rates. When the critical point is on the hemisphere, little coolant is wasted on the hemisphere but a great deal of coolant is wasted on the larger cone area. Thus, a poor match between theoretical and delivered coolant flow rate results. The nosetip goes from cone critical to hemisphere critical at a permeability of 3×10^{-10} in^2; thus, a rapid increase in coolant requirements occurs at permeabilities greater than 3×10^{-10} in^2.

As expected, the internal nosetip pressure increases with decreasing (tighter) permeability. Pressure requirements vary between 261 psi to 5324 psi over the 1×10^{-9} to 1×10^{-12} in^2 permeability range. Dual permeability was evaluated for those cases where coolant rates exceeded 2.7 lb/sec. At all but 1×10^{-9} in^2 permeability, a cone permeability could be selected so as to reduce the coolant rate to 2.7 lb/sec. Three conclusions can be drawn from the analytical results: (1) endohoming interceptor nosetip design is insensitive to permeability over a wide range of permeabilities, 3×10^{-10} to 1×10^{-12} in^2; (2) nosetip internal pressure requirements are acceptable over the range of 1×10^{-9} to approximately 1×10^{-11} in^2 permeability, i.e., gas bottle sizing is reasonable; (3) the use of a dual permeability nosetip is unnecessary

20

in endohoming interceptor nosetip design since a good match to the thermally required coolant flow rate can be achieved with a single permeability over a wide range of permeabilities. Previous studies on porous stainless steel nosetips have shown that permeabilities near 1 x 10^{-10} in^2 can be achieved using conventional powder metallurgy technique. Therefore, a permeability of 1 x 10^{-10} in^2 was selected for the endohoming interceptor nosetip.

The present analysis shows that a good match between the thermally ideal coolant flux distribution and the actual delivered flux distribution can be achieved at all conditions evaluated (50 Kft, 10 Kft/sec; 100 Kft, 10 Kft/sec, and 100 Kft, 20 Kft/sec). Thus the nosetip permeability is mission independent. The extent to which coolant flow history matches that required by the nosetip will be controlled by the efficiency of the flow control valve employed in the subsystem. The nosetip design drawing is shown in Figure 2-7.

2.7 STRESS ANALYSIS

A stress analysis was performed on the flat cutout region on the cone (the most stress critical portion of the porous nosetip), the 321 CRES nosetip/coolant delivery tube attachment plate, MIL-5-6721, and on the weld between the nosetip and the attachment plate.

Room temperature properties were assumed (see Section 5.2) for the porous stainless steel (yield strength 17,000 psi, ultimate strength 25,000 psi), because most of the thickness of the cone wall remains at room temperature under steady-state flow conditions and only the room temperature portion of the thickness was considered in the stress analysis. The flat surface of the nosetip cone was modeled as an equilateral triangular palte with clamped edges, as described in "Theory of Plates and Shells", by Timoshemko, an internal nosetip pressure of 532 psi was assumed corresponding to that required for a gaseous nitrogen flow rate of 2.73 lb/sec and a nosetip permeability of 1 x 10^{-10} in^2. The margin of safety is $.4 on yield and 5.45 on ultimate strength.

The base plate stress analysis using a yield strength of 30,000 psi and ultimate strength of 75,000 psi for CRES 321 resulted in a calculated margin of safety on yield strength of 1.87 and on ultimate strength of 7.19.

The weld between the porous cone and the attachment plate was analyzed as a cylinder attached to a flat closure on one end with fixed edges. The equation used was from "Formulas for Stress and Strain" by Roark, 3rd edition, Table XIII, case 24, page 274. The modulus of elasticity of the porous material was taken as 1.2×10^7 psi and that of the base plate as 2.8×10^7 psi while Poisson's ratio was taken as 0.330. For a nominal plate thickness at the weld of 0.370 inch, the margin of safety is 1.11 on yield and 1.66 on ultimate strength. The stress analysis indicates that the minimum margin occurs at the weld. The analysis performed is conservative as was shown during the ground test program, Section 9, when one nosetip was pressurized to 700 psia and another to 1400 psia without evidence of yielding. It is recommended that the nosetip be analyzed using more sophisticated computer modeling techniques.

DIM	-3	-5
A	2.350 R	2.340 R
B	1.510	1.500
C	.190 R	.200 R
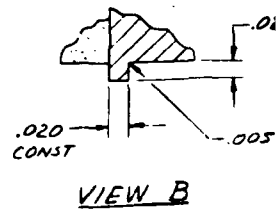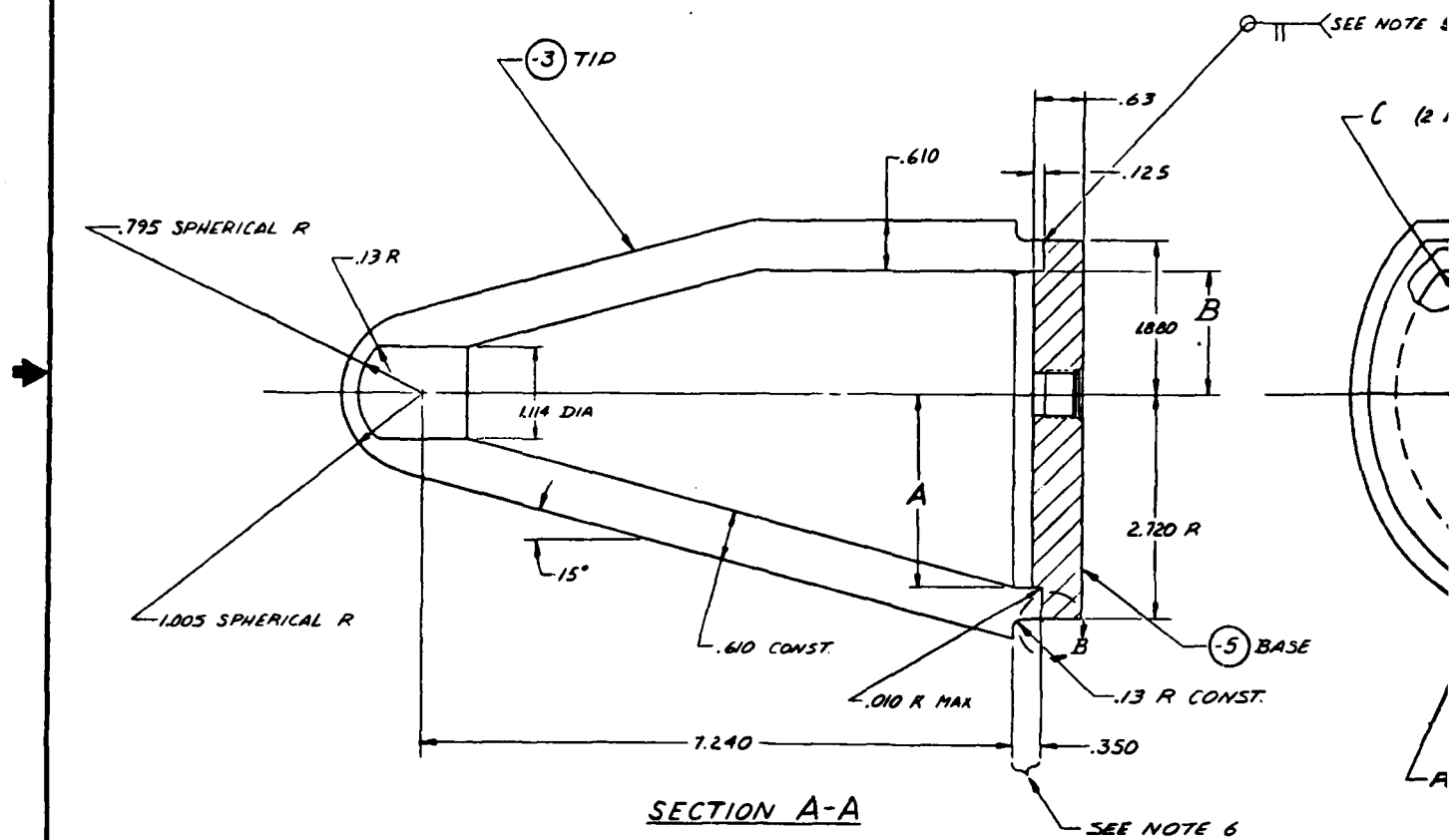
(-3) TIP

.795 SPHERICAL R

.13 R

.610

.63

.125

B

1.880

1.114 DIA

A

15°

.610 CONST.

1.005 SPHERICAL R

.010 R MAX

2.720 R

B

(-5) BASE

.13 R CONST.

7.240

.350

SECTION A-A

SEE NOTE 6

SEE NOTE

C (2

.020
CONST

.005

VIEW B

Figure -7. Enlohexing Transpiration Cooled Nosetip

GENERAL NOTES: UNLESS OTHERWISE SPECIFIED.

1. ALL MACHINED SURFACE ROUGHNESS 125√ PER USAS B46.1.
2. BREAK SHARP EDGES .010 R MAX.
3. PASSIVATE -5 PER MIL-S-5002.
4. AFTER FINAL MACHINING OF -3, ACID ETCH PER ENGR. INSTRUCTIONS.
5. ELECTRON BEAM WELD -3 TO -5.
6. SHOT PEEN THIS AREA PER ENGR INSTRUCTIONS.
7. MAT'L:
   -3 CRES POWDER PRESSED AND SINTERED PER ENGR. INSTRUCTIONS.

   -5 .625 × 5.0 × 6.0   CRES PLATE 321   MIL-S-6721

(SEE NOTE 5

C (2 PL)

A

PORT PER MS33649-6

A

.020 CONST

.005 R MAX

B

1T51392

Section 3
POWDER CHARACTERIZATION

3.1 POWDER FABRICATION METHOD

Eight hundred pounds of -200 mesh, 316L stainless steel powder were procured from Hoeganaes Corporation. A water atomization process was used to produce the powder. The starting material consisted of sponge iron, pure elements, and some steel scrap that was carefully blended to yield a 316L composition that was low in manganese. The low manganese content resulted in atomized powder that was irregularly shaped and had high compaction green strength. A molten stream of the starting material was fed into a chamber filled with nitrogen gas where it was atomized by two high pressure water jets. The atomized powder then fell into a water bath from which it was subsequently withdrawn, dried, and screened to less than 75μ in size.

3.2 POWDER SIZE CLASSIFICATION AND CHEMICAL ANALYSIS

The as-received -200 mesh 316L powder was classified into the following particle sizes: -7μ, 7 to 25μ, 25 to 44μ, 44 to 63μ, 63 to 74μ, and $+74\mu$. A Vortec model C1 particle classifier was used to divide the powder up to a size of 44μ. The larger and heavier particles above 44 that could not be sized with the air screening apparatus were classified using stainless steel screens and mechanical agitation. The particle size distribution is shown in Table 3-1.

Vendor specifications received with the powder showed that the material met the chemical requirements of Federal Specification QQ-S-763d. A chemical analysis of the powder was made in the as-received condition and again after classification to ensure chemical purity during processing. It can be seen in Table 3-2 that both the as-received and 25 to 44μ classified powder met the chemical requirements for wrought 316L stainless steel.

Table 3-1. Particle Size Distribution for -200 Mesh 316L Powder

Particle Size, μ	Weight, lbs.	% of Total
-7	5	0.6
7 to 25	119	14.9
25 to 44	315	39.4
44 to 63	157	19.6
63 to 74	152	19.0
+ 74	44	5.5

Saved as-received powder	8	1.0

Table 3-2. Chemical Analysis of 316L Powder

Element	As-Received Powder	25 to 44μ Powder	Specification Requirements
C	0.03	0.03	0.03 max
Mn	0.78	0.83	2.0 max
Si	0.48	0.47	1.0 max
P	0.013	0.011	0.041 max
S	0.015	0.016	0.03 max
Cr	17.7	17.9	16 to 18
Ni	12.4	13.6	10 to 14
Mo	2.3	2.2	2 to 3
Fe	Base	Base	Base

3.3 PHYSICAL PROPERTIES OF THE POWDER

Metallographic analysis of the powder revealed a microstructure indica-
tive of material that was rapidly cooled from a melt condition (Figure 3-1).
The shape of the powder was determined by examining it in a scanning electron
microscope (SEM). The powder consisted of a combination of smooth spherical
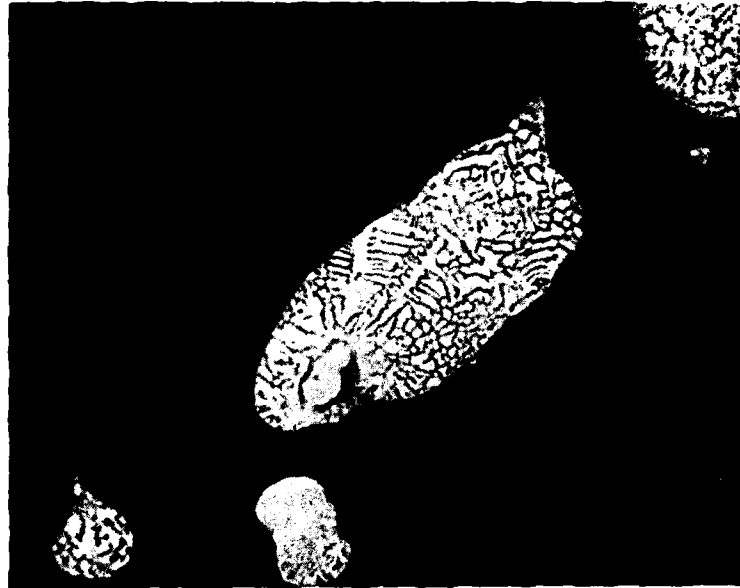and oblong shaped particles intermixed with numerous irregular particles (Fig-

26

MCDONNELL DOUGLAS

Figure 3-1. Microstructure of 316L Powder (1040X)

Figure 3-2. SEM Photograph of 316L Powder (700X)

27

ure 3-2). The degree of cold work in the as-received powder was evaluated using x-ray diffraction analysis. Peak position and line breadth measurements were made for the (111), (200), and (220) peaks for annealed and as-received powder, as shown in Table 3-3. This data indicated that the powder was received in the annealed condition. The minor changes seen between the annealed and as-received powder are probably due to solute segregation that occurred when the material was atomized.

3.4 POWDER SPECIFICATION

A powder procurement specification was prepared with the concurrence of Hoeganaes Corporation that will assure consistent powder in subsequent orders. The specification details the powder manufacturing method and the requirements for chemical purity, particle size distribution, particle shape, and heat treatment condition. A copy of this specification is given in Appendix A.

MCDONNELL DOUGLAS

Table 3-3. Line Breadth and Peak Position Measurements for As-Received and Annealed 316L Powder From Lot No. 12-35920

(hkl)	25 to 44μ Annealed		25 to 44μ As-Received		44 to 75μ Annealed		44 to 75μ As-Received	
	Breadth 2θ	Peak 2θ	Breadth 2θ	Peak 2θ	Breadth 2θ	Peak 2θ	Breadth 2θ	Peak 2θ
(111)	0.15	43.57	0.17	43.43	.15	43.54	0.18	43.48
	0.15	43.56	0.18	43.44			0.16	43.50
(200)	0.13	50.75	0.18	50.64	.12	50.73	0.20	50.66
	0.13	50.75	0.200	50.63			0.20	50.67
(220)	0.12	74.63	0.14	74.52	.11	74.61	0.14	74.54
	0.13	74.63	0.12	74.51			0.15	74.56

29

Section 4
SINTERING CHARACTERISTICS

4.1 SINTERING CONDITIONS

The permeability of sintered billets is controlled by the particle size, pressing pressure, sintering time, and sintering temperature. obtain maximum strength in the green billet, it is desirable to use the highest available pressing pressure. Since the isostatic press capable of handling the full-scale billets had a working pressure of 25 KSI, this pressing pressure was chosen for the sintering tests. Of the two variables, time and temperature, the time at temperature has the least effect on the sintering characteristics of the material. A sintering time of 4 hours was chosen for this study. Particle size and sintering temperature are the two variables that were evaluated for obtaining sintered billets with a prescribed degree of porosity.

A series of cylindrical test billets 1.3 inches in diameter and 1 inch in height were isostatically pressed at 25 ksi. The billets were pressed using powders from either a single-screened particle size range or a 50/50-weight percent blend of two size ranges. The powder blends were produced by rotating equal weights of the two selected particle size ranges in a conical blender for 1 hour. The test billets of each particle range or blend were then

Table 4-1. Tabulation of Samples Used to Determine the Sintering Characteristics of 316L Powder Compacted at 25 ksi

Temp. °F \ Powder Size	7 to 25µ	7 to 25µ 25 to 44µ	24 to 44µ	25 to 44µ 44 to 63µ	44 to 63µ
2100	1*	1	1	2	2
2200	1	1	2	2	2
2250	1	1	1	1	1
2300	1	1	1	1	1
2350	1	1	1	1	1

*Numbers shown indicate number of samples for each test condition.

MCDONNELL DOUGLAS

sintered over a range of temperatures in 10^{-6} torr vacuum to determine billet permeability as a function of both particle size and sintering temperature. The conditions selected are tabulated in Table 4-1.

4.2 PERMEABILITY MEASUREMENTS

Permeability discs measuring 1 inch in diameter by 0.11 inch thick were machined from the center of each billet. The discs were cooled with Freon during machining. Turning speeds were typically 130 surface feet per minute (SFM) with a feed of 0.05 inch per revolution. The depth of cut for rough machining was 0.03 inches. A finished surface was achieved by making a minimum of five cuts, each 0.005 inches deep.

After the permeability discs were machined, they were electroetched to remove smeared metal from the machined surfaces. The electrolyte consisted of 40% by volume of concentrated sulphuric acid (specific gravity of 1.84) and 60% concentrated phosphoric acid (specific gravity of 1.70). A stainless steel cathode was used with the sample as the anode. Typical electrical parameters for the one inch diameter disc were 10 volts and 7 to 10 amperes. These values yielded a current density of about 6 amperes per square inch. The electrolyte was stirred continuously and maintained at a temperature between 90 and 120°F. It was found that 0.005 inch of metal had to be etched from each surface to remove the smeared metal produced during machining.

Following etching, each disc was passivated, rinsed and dried. A specimen holder of the type shown in Figure 4-1 was used to flush the various solutions through each specimen. Each disc specimen was clamped in the lower part of the rinse fixture and a 5% nitric acid solution was poured in through the liquid fill opening. The liquid fill cap was then installed and the chamber was pressurized with nitrogen gas to 150 psi, thus forcing the solution through the disc. This process was then repeated with 200 milliliters of deionized water and again with 200 milliliters of methanol. After expelling the methanol, the nitrogen gas was forced through the disc to promote drying. The disc was then removed from the rinse fixture and dried in air at 150 ± 10°F for one-half hour.

The permeability of each specimen was determined by flowing nitrogen gas through it using five different flow rates. The upstream and downstream pressures were recorded for each flow rate. The pressures, flow rates, sample thickness, and gas temperature were used in a modified D'arcy equation, equa-

32

tion 2-10, to calculate the permeability constant, "K." The permeabilities of the specimens listed in Table 4-1 are plotted in Figure 4-2 as a function of sintering temperature.

Because electroetching required a relatively large current density, chem-milling was evaluated as an alternative method for removing smeared metal from the full-scale nosetips. Two permeability discs that were previously evaluated were surface ground using 60 grit metallographic paper and subsequently chem-milled to remove a minimum of 0.005 inch of material from each surface. The chemical milling was accomplished at Aerochem Incorporated in Orange, California. A modified aqua regia etchant, designated Etchant No. 30 per Aerochem Process Specification APS 1300, was used at $150^{\circ}F$. A total of 0.006 inch of material was removed from each surface in approximately 10 minutes, leaving behind surfaces that were visually smooth and uniform. The discs were then cleaned using the previously described procedure. It was found that the permeability of the discs did not change as a result of the chem-milling. Therefore chem-milling was considered to be an acceptable alternative to electroetching.

4.3 ELECTRICAL CONDUCTIVITY

A correlation was made between electrical conductivity and billet permea-bility by measuring the surface conductivity of the permeability discs listed in Table 4-1. The conductivity measurements were made using a NORTEC NDT-5A with a 5/8-inch-diameter probe. Electrical conductivity plotted as a function of disc permeability is given in Figure 4-3. Conductivity values are measured as % IACS (International Annealed Copper Standard), which is a percent of the electrical conductivity for pure annealed copper. While the data in Figure 4-3 does show some scatter, the curves are sufficiently accurate to predict the degree of sintering in full-scale billets.

4.4 SHRINKAGE CHARACTERISTICS

Billet density and total shrinkage were determined as a function of per-meability, Figures 4-4 and 4-5. Using the density measurements in Figure 4-4, the weight of a full-scale, conical shaped billet with a permeability constant of 1×10^{-10} in.^{2} was calculated to be 30 pounds. The shrinkage data given in Figure 4-5 was used to size the polyurethane mold for isostatically pressing the full-scale billets. The line in Figure 4-5 defines the minimum shrinkage that had to be accounted for in the mold size. The design of the mold will be discussed in detail in Section 6.
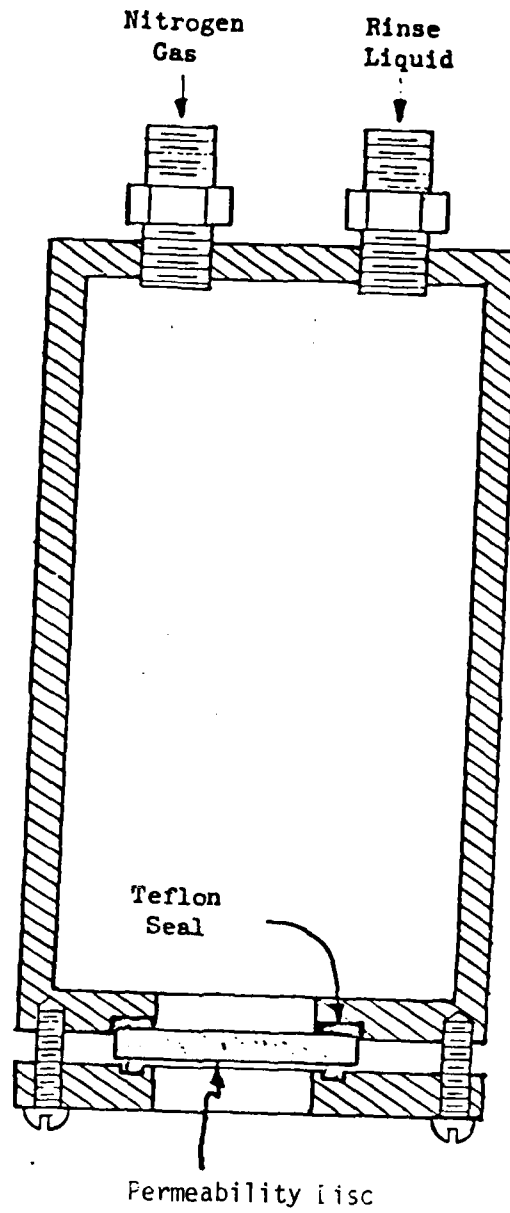
33

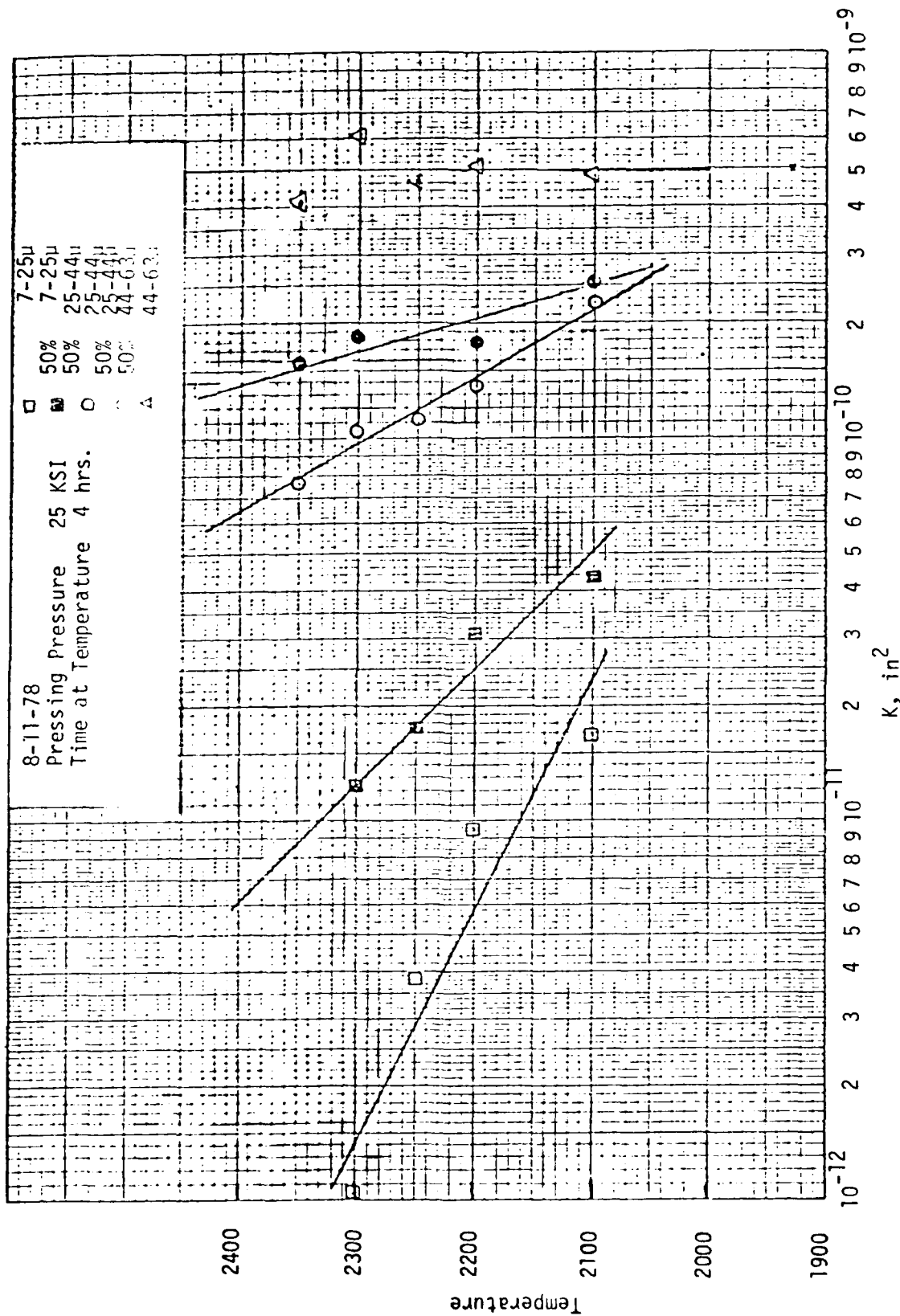Figure 4-1. Permeability Disc Rinse Fixture

MCDONNELL DOUGLAS

Figure 4-2. Effect of Particle Size and Temperature on Billet Permeability. All Samples Were Isostatically Pressed at 25 ksi and Sintered at Temperature for 4 Hours in Vacuum. One-Inch-Diameter Billets Were Used.
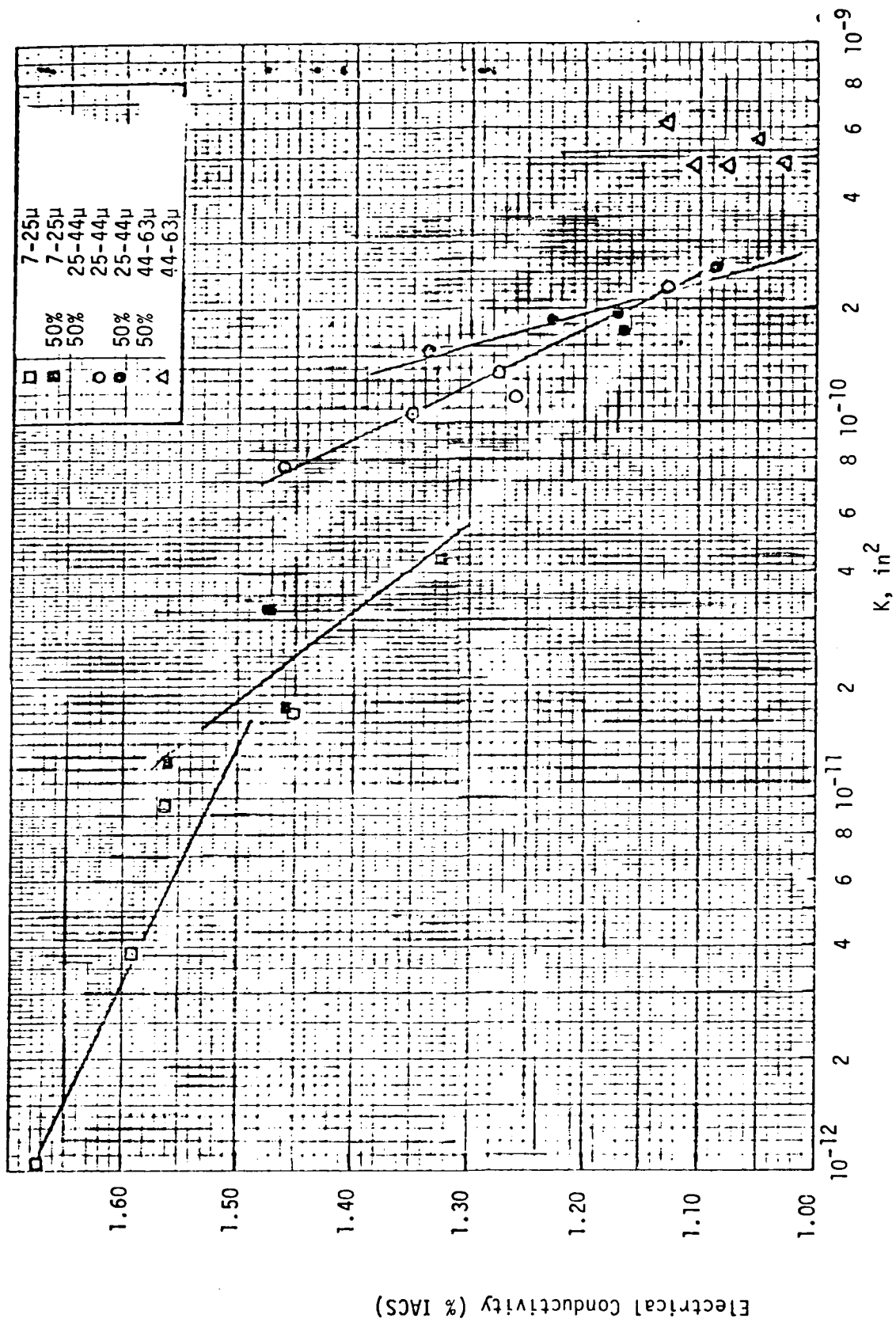
35

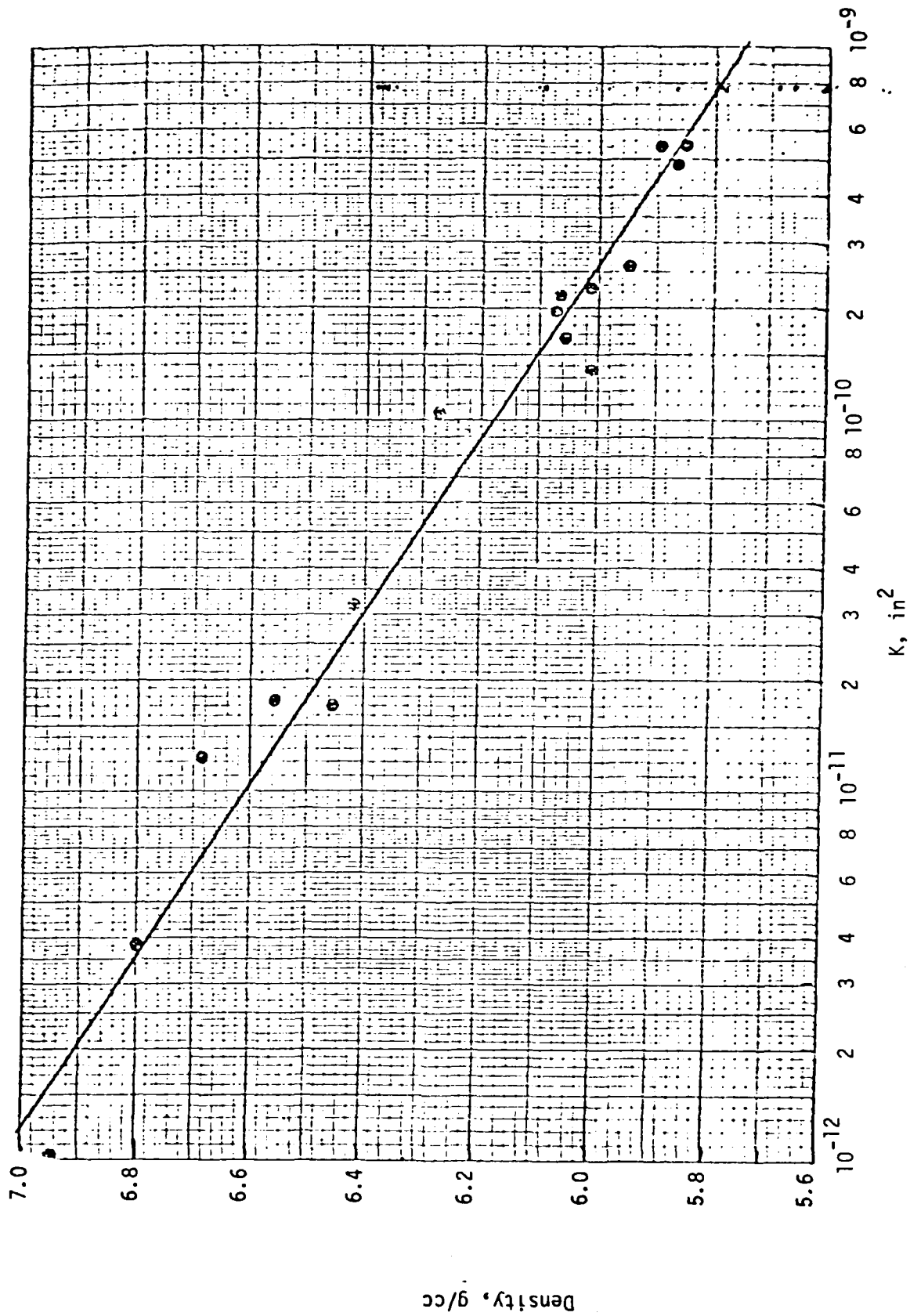Figure 4-3. Electrical Conductivity Shown as a Function of Billet Permeability

36

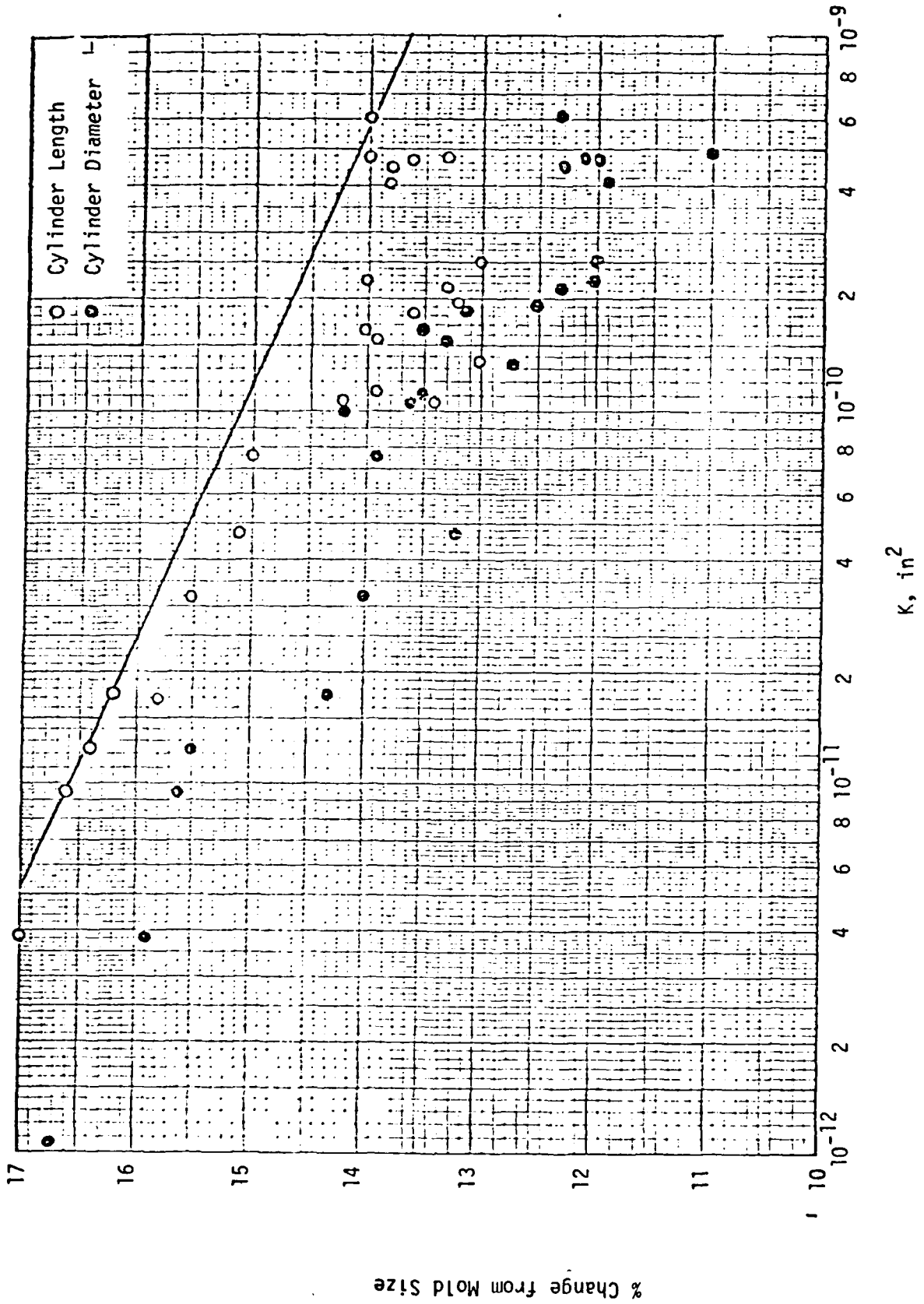Figure 4-4. Billet Density Given as a Function of Permeability

37

Figure 4-5. Percent Change in Billet Length and Diameter From Mold Size to Sintered Billet Size Shown as a Function of Permeability

Section 5
SUBSCALE BILLET EVALUATION

5.1 BILLET FABRICATION

A large billet measuring 4.3 inches in diameter by 5.0 inches long was fabricated to verify the sintering parameters established by the small experimental billets. Because a permeability of 1×10^{-10} in^2 was selected in Section 2 for the full-scale nosetips, the following powder size and sintering parameters, as determined from Figure 4-2, were used to fabricate this billet.

A polyurethane mold was filled with 24 to 44 size powder while the mold was continuously vibrated on a shake table. The mold was then sealed and isostatically pressed at 25 ksi. The billet was sintered at 2300°F $\pm$ 20°F for four hours in a 10^{-6} torr vacuum. In an attempt to minimize thermal stresses in the billet and thus prevent the internal cracking found in previous studies, the heat-up rate of the billet was limited to 700°F per hour. The sintered billet is shown in Figure 5-1 next to one of the small experimental billets that was used to develop the temperature versus permeability curves in Figure 4-3.

5.2 PROPERTIES OF BILLET

The billet was cut into six segments from which permeability discs and tensile specimens were machined, Figure 5-2. Also shown in Figure 5-2 is a tabulation of the mechanical and physical properties of the billet.

Each segment of the billet was radiographed and carefully examined for cracks. There were no indications of cracks in any of the segments.

Using the previously described procedures, the electrical conductivity of the sintered billet was measured as 1.40% IACS. From the electrical conductivity curve in Figure 4-3 for the 25 to 44 size powder, the permeability of the large billet was estimated to be between 0.8 and 1.1×10^{-10} in^2. Five permeability discs were removed from three different segments of the billet to
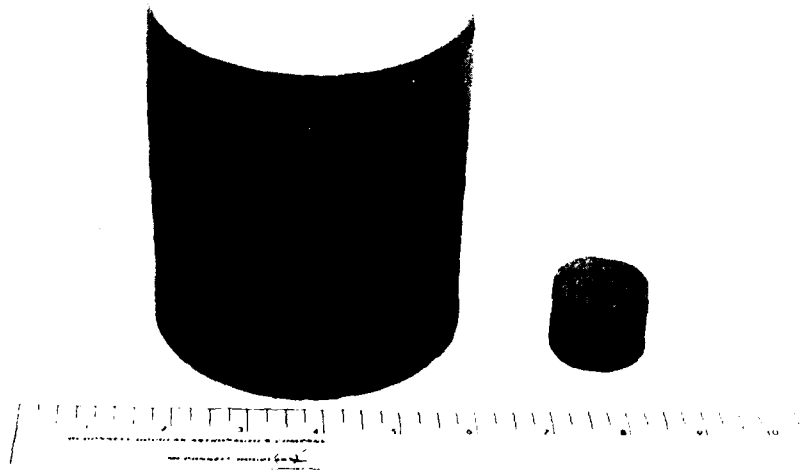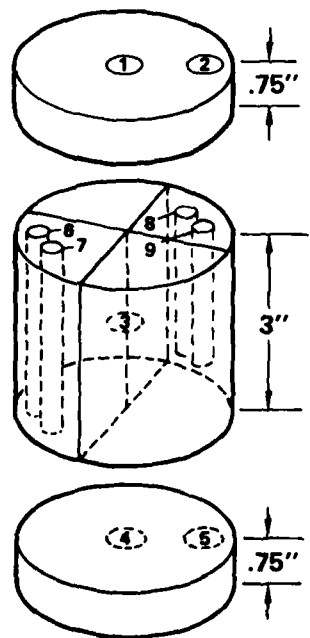
Figure 5-1. Comparison of Large Diameter Billet and Experimental Permeability Billet

PERMEABILITY

SAMPLE NO.	K IN^2
1	1.02×10^{-10}
2	0.95×10^{-10}
3	0.90×10^{-10}
4	1.06×10^{-10}
5	0.91×10^{-10}

TENSILE PROPERTIES

ROOM TEMPERATURE

SAMPLE NO.	F_{TY} (PSI)	F_{TU} (PSI)	ELONG. (%)
6	21,690	31,265	6
7	18,890	28,285	6

1000°F

SAMPLE NO.	F_{TY} (PSI)	F_{TU} (PSI)	ELONG. (%)
8	11,815	18,735	4
9	14,545	20,810	4

Figure 5-2. Mechanical and Physical Properties of Subscale Billet

establish the actual permeability constant. It can be seen in Figure 5-2 that all of the permeability values were consistent with the target value of 1 x 10^{-10} in^2.

The average density of the billet was calculated to be 6.22 gm/cc as determined by measurements made on the permeability discs. The curve in Figure 4-4 predicts a density of approximately 6.19 gm/cc for a permeability of 1 x 10^{-10} in^2.

Smooth round tensile specimens were used to determine the mechanical properties of the material. The room temperature tests showed an average yield strength of 20,290 psi and an average ultimate strength of 29,775 psi, while at 1000°F the yield strength decreased to 13,280 psi and the ultimate to 19,773 psi, Figure 5-2.

Metallographic analysis of the billet showed a relatively uniform pore structure, Figure 5-3, with an average pore size of 17μ. The recrystallized grain structure showed minimum grain growth and an average grain size of 20μ.
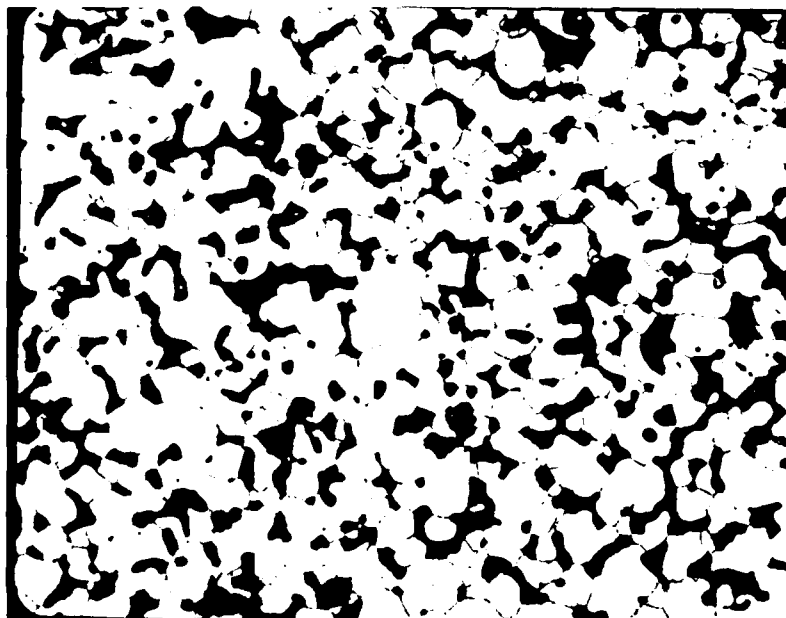

Figure 5-3.   Microstructure of Porous 316L with a Permeability
Constant of 1 x 10^{10} in^2 (255X)

Section 6
FULL-SCALE BILLET FABRICATION

6.1 MOLD DESIGN

A polyurethane mold was designed for producing near-net-shape full-scale billets. The mold shape, sintered billet shape, and position of the machined nosetip and permeability discs within the billet are schematically shown in Figure 6-1. The mold was sized with respect to the sintered billet to allow for 15% shrinkage in compacting and sintering the powder. The 15% shrinkage factor was established by using the curve in Figure 4-5 with a desired billet permeability of 1×10^{-10} in^2. The sintered billet was sized to be 10% larger than the machined nosetip. The oversized billet provided sufficient material for removing surface irregularities introduced during the powder compaction process.

6.2 BILLET FABRICATION

The polyurethane mold for making the full-scale billets is shown in Figure 6-2A. In an attempt to develop a method for compacting the powder to yield consistent green billets, three different procedures for filling the mold with 25 to 44 size powder were examined. In each case the mold was placed in a fiberglass holder on a shake table as shown in Figure 6-2B. With the shake table operating, the mold was slowly filled with powder. The three different filling procedures that were examined are: (1) continuous pouring, (2) pouring in 250 ml steps with a two minute hold time between pours, and (3) continuously tamping while pouring. After filling each mold, it was sealed with rubber tape and isostatically pressed at a pressure of 25 KSI with a hold time of one minute at pressure.

The condition of the green billets using the various mold filling procedures is tabulated in Table 6-1. Since the tamped billet showed excessive chipping and the intermittent pour billet contained a layered structure, these two processes were considered unacceptable. The most uniform billets in both shape and size were fabricated by continuously pouring the powder into the
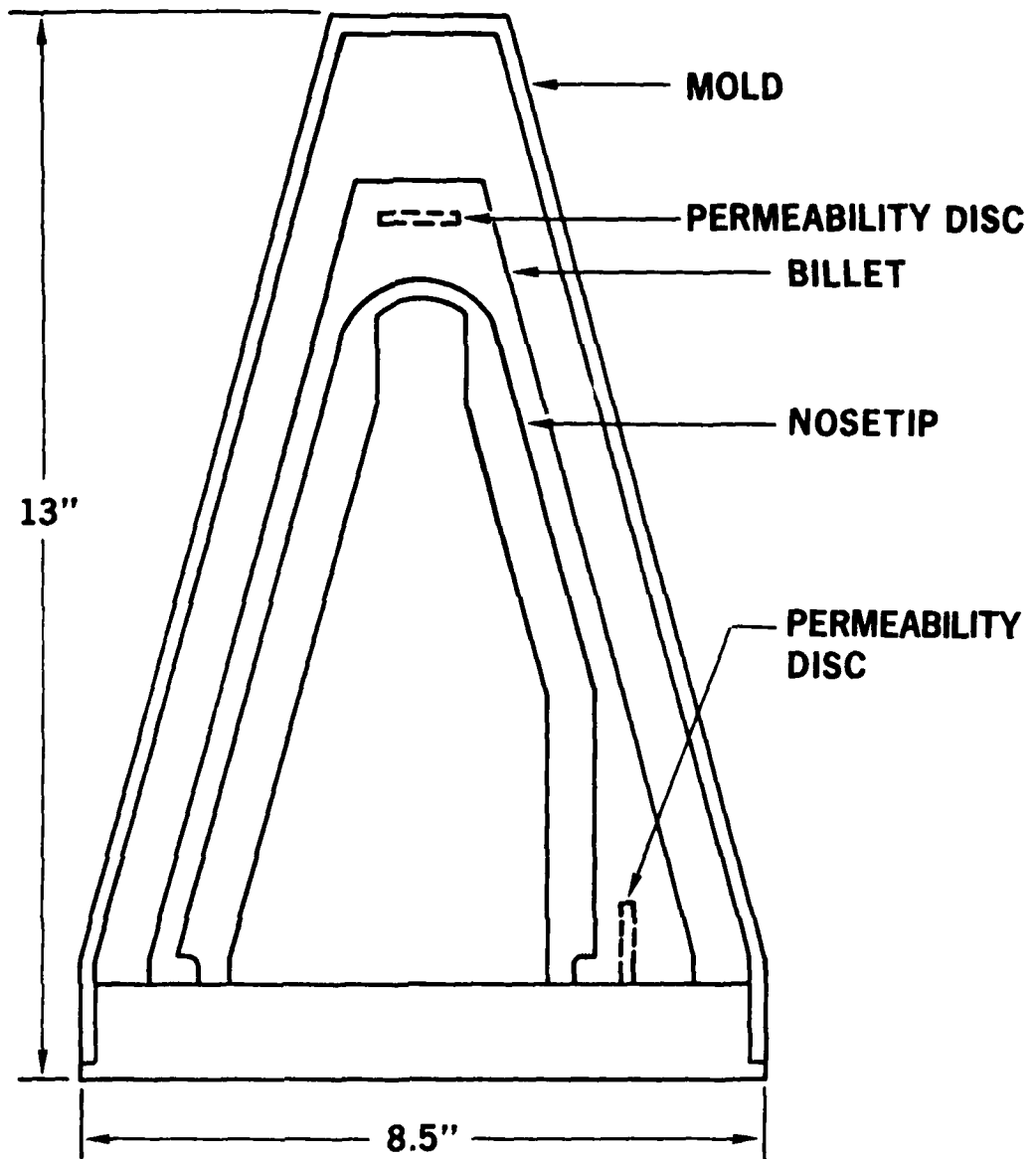
43

Figure 6-1. Schematic Presentation of Mold Shape, Sintered Billet Shape, and Position of Machined Nosetip and Permeability Discs Within the Billet
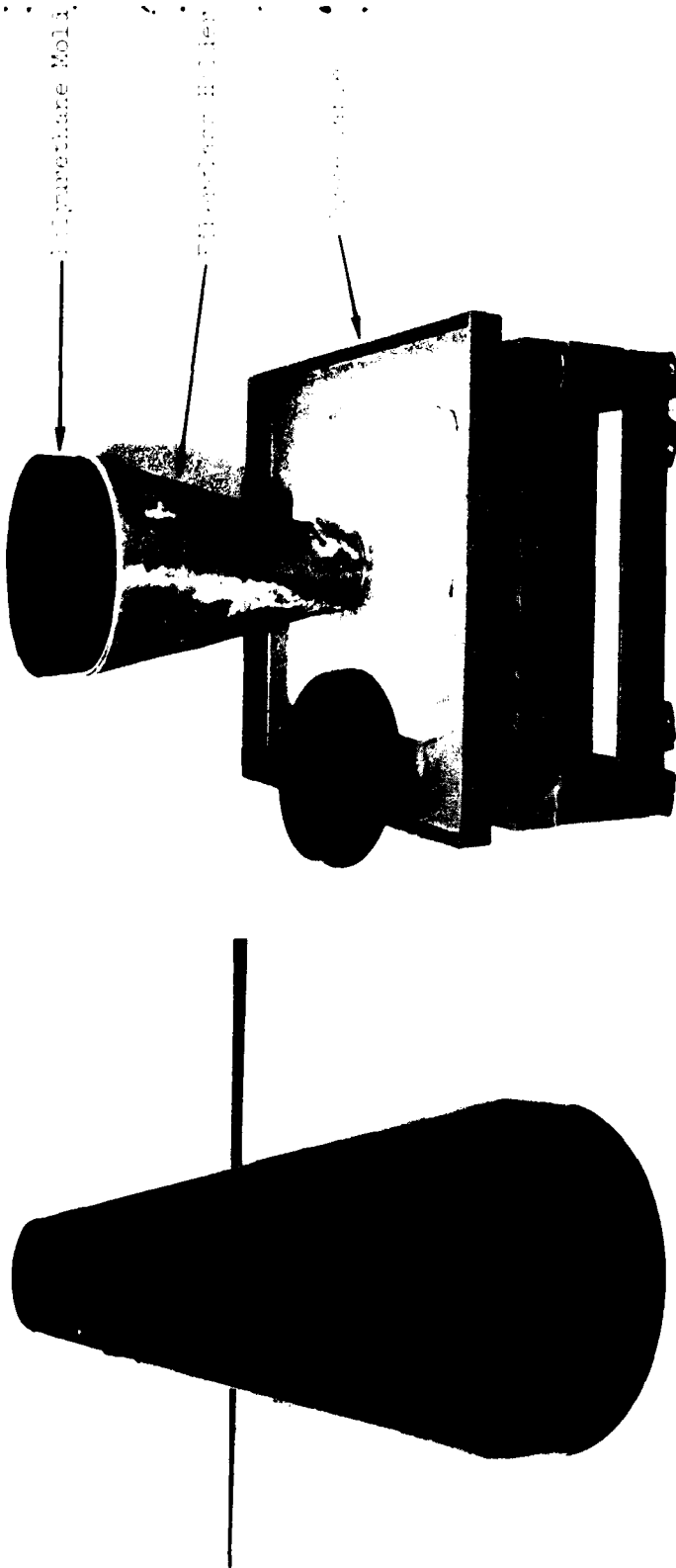
Figure 6-2b. Shake Table with Polyurethane Mold
and Fiberglass Holder

Figure 6-2a. Polyurethane Mold for Making
Tape-Wrap Fiberglass Holder

MCDONNELL DOUGLAS

Table 6-1. Tabulation of Mold Filling Methods and Corresponding Condition of Billets After Isostatically Pressing at 29 ksi

Billet No.	Mold Fill Method	Condition of Billet After Isostatically Pressing
1N	Continuously poured while vibrating mold.	Faint swirl marks on surface, slight chipping at base.
2N	Powder poured in 250 ml steps with a two minute hold time between pouring; mold vibrated continuously.	Surface appearance indicated that the powder had formed a layered structure.
3N	Continuously poured while vibrating mold.	Faint swirl marks on surface, slight chipping at base.
4N	Tamped and continuously poured powder while vibrating mold.	Very severe chipping around base.
5N	Continuously poured while vibrating mold.	Faint swirl in areas on surface, slight chipping.
6N	Continuously poured while vibrating mold.	Faint swirl marks on surface, slight chipping.
7N	Continuously poured while vibrating mold.	Faint swirl marks on surface, slight chipping.

46

vibrating mold. A total of five billets were processed using this procedure. Some chipping did occur at the base of these billets; however, this chipping was considered to be within acceptable limits, Figure 6-3.
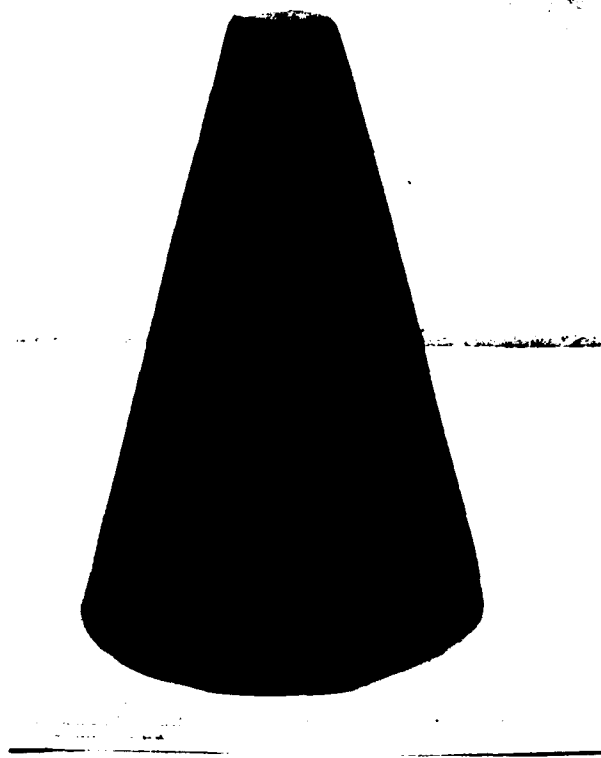

Figure 6-3. Pressed Billet Fabricated by Cold-Isopressing and Vibrating

6.3 BILLET SINTERING

All of the billets were sintered at Vac Hyd Corporation in Torrance, California using a vacuum of 10^{-6} Torr, a maximum heat-up rate of 600°F/hr, and a hold time of four hours at temperature. Billets 1N through 4N were sintered at 2300°F $\pm$ 10°F, and billets 5N through 7N at $2,275^{\circ}$F $\pm$ 10°F. A dimensional check of each billet showed that all of the billets except No. 4N met the nosetip drawing requirements. Billet No. 4N did not meet dimensional requirements because of the severe chipping that occured at the base of the billet during cold pressing.

41

6.4 BILLET PROPERTIES

Electrical conductivity measurements were made on each sintered billet and two permeability discs were removed from each billet at the locations shown in Figure 6-1. The discs were electroetched to open the surface pores, and permeability measurements were made using the procedures described in Section 4. The electrical conductivity and permeability values obtained for these billets are given in Table 6-2.

It can be seen in Table 6-2 that the electrical conductivity of the billets did give a reasonable estimate of the actual billet permeability. The actual permeabilities of the full-scale billets were within an acceptable range even though they were somewhat lower than the desired 1×10^{-10} in^2.

Table 6-2. Electrical Conductivity and Permeability of Nosetip Billets

Billet Number	Electrical Conductivity % IACS	Predicted * K (10^{-10} in^2)	Actual Permeability K (10^{-10} in^2)	
			Top	Base
1N	1.38	1.0	0.9	0.9
2N	1.41	0.9	0.8	0.9
3N	1.35	1.0	0.9	0.9
4N	1.36	1.0	0.9	0.9
5N	1.43	0.8	0.8	0.9
6N	1.41	0.9	0.8	0.8
7N	1.36	1.0	0.8	0.8

*Predicted K value obtained from Figure 13.

Section 7
NOSETIP MACHINING

Four billets, numbers 1N, 2N, 6N, and 7N, were selected for processing into full-scale nosetips. The machining of these billets was accomplished using a combination of conventional machining methods, electrical discharge machining, and chemical milling. Following is a detailed discussion of the machining procedure.

7.1 CONVENTIONAL MACHINING

Each billet was rough machined to the approximate nosetip shape leaving 0.035 inches of excess material on each surface. The rough machining operation was performed using conventional shop equipment with freon as a coolant to eliminate the problem of pore blockage which can occur with oil coolants. Carbide cutting tools were used with turning speeds between 125 to 150 surface feet per minute. A cutting tool surface feed rate of 0.05 inches per revolution was used with the cutting depth set at 0.030 inches.

The outside surfaces and inside forward section of each nosetip were then final machined to within 0.005 inches of final dimensions using a cutting depth of 0.005 inches per pass. This procedure eliminated the surface deformation introduced during rough machining and limited the depth of additional disturbed metal to that which could be easily removed by chemical milling.

7.2 ELECTRICAL DISCHARGE MACHINING

The inside aft surfaces of each nosetip were machined to within 0.005 inches of drawing requirements by Electrical Discharge Machining (EDM) at EDM Laboratories in Garden Grove, California. This machining procedure was selected because dimensional tolerances could not easily be achieved in the aft nonsymmetrical area using conventional machining methods. A carbon electrode was used in the EDM process with deionized water as the dielectric fluid. Previous studies showed that the use of conventional dielectric fluids such as oil or kerosene resulted in pore contamination that could not be subsequently removed. A dark gray residue found on the surface of each nosetip

after the EDM operation was ultrasonically removed in deionized water. Each nosetip was then cleaned in methanol and dried prior to chemical milling.

7.3 VISUAL AND RADIOGRAPHIC INSPECTION

After machining and prior to chemical milling, the nosetips were visually examined and radiographed. Three cracks, each approximately one inch long, were found on the inside surface of nosetip 1N. No indications of cracks were found in the remaining three nosetips. Therefore, the fabrication of only nosetips 2N, 6N, and 7N was continued.

7.4 CHEMICAL MILLING

Both conventional and electrical discharge machining produced a surface condition that reduced the gas flow through the nosetips. This surface condition, normally less than 0.005 inches deep, was removed by chemical milling. The chemical milling was accomplished at Aerochem, Inc. in Orange, California. A modified aqua region etchant, designated Etchant No. 30 per Aerochem Process Specification APS 1300, was used at $150^\circ F$. A total of 0.006 inches of material was removed from each surface in approximately 10 minutes leaving behind surfaces that were visually smooth and uniform. Some shallow, isolated pits were found on the outside surfaces of each nosetip.

After chemical milling, absorbed acid was removed by attaching a base plate to each nosetip and forcing cleaning solutions through the nosetips under an argon pressure of 100 psi. Figure 7-1 shows a nosetip in the process of being cleaned (A) and one that was cleaned and dried (B). The cleaning procedure is shown in Table 7-1.

Table 7-1. Nosetip Cleaning Procedure Following Chemical Milling

Cleaning Solution	Purpose
1. Deionized water	Remove milling acid
2. Deionized water + 5% HNO_3	Passivate stainless steel
3. Deionized water	Remove passivation acid
4. Methanol	Promote drying

(B)

(A)

53
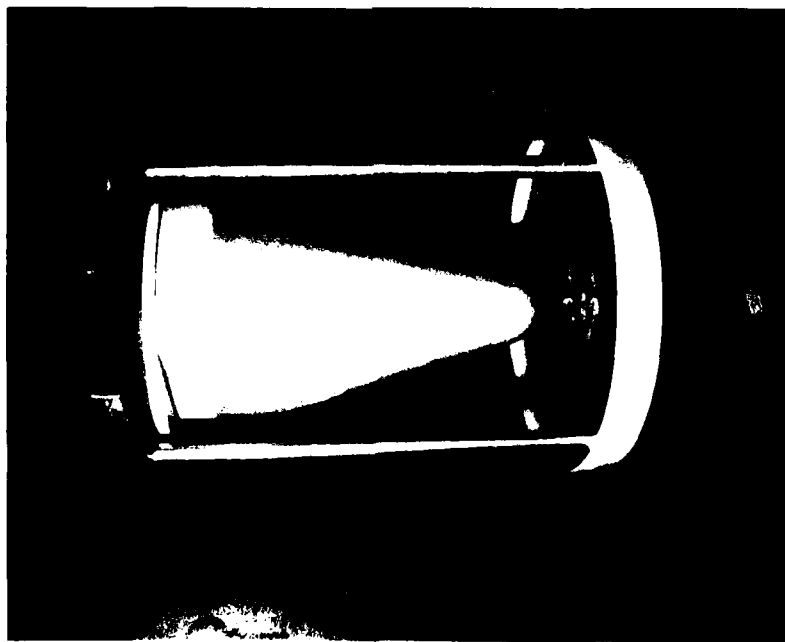
7.5 NOSETIP WELD JOINT AND BASEPLATE MACHINING

The aft end of each nosetip was machined in accordance with Figure 2-7 in preparation for welding. The machining conditions were the same as those that were used to contour the nosetip. Also shown in Figure 2-7 is the configuration of the 321 stainless steel base plate. Each base plate was fabricated to be a slip fit in the intended nosetip. A machined nosetip and base plate are shown in Figure 7-2 prior to welding.
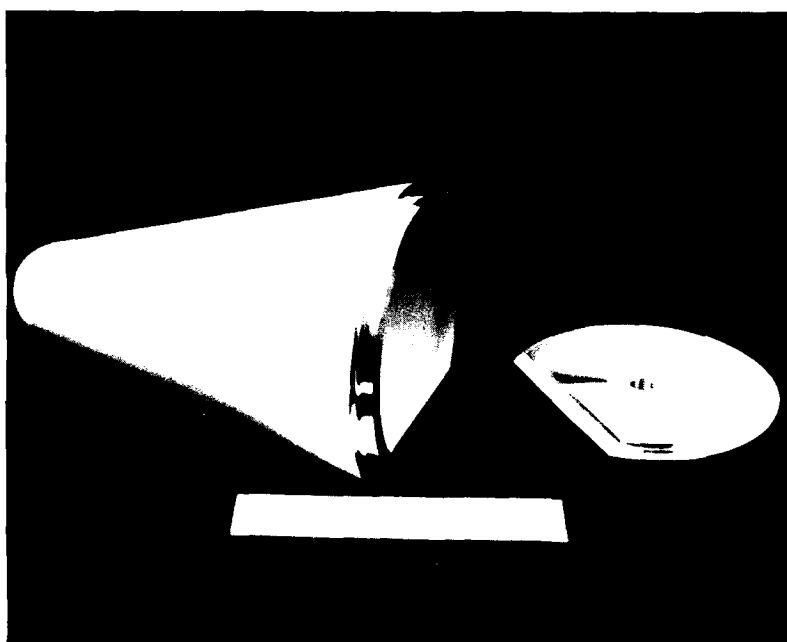

Figure 7-2. Machined Nosetip and Baseplate Prior to Welding

54

Section 8

NOSETIP WELDING

Electron beam welding was selected as the method for attaching the baseplate to the nosetip. In previous studies, it was found that electron beam welding minimized contamination and damage to the porous material and provided a sound full-penetration weld.

8.1 WELD PARAMETERS

Test specimens simulating the weld joint were electron beam welded to establish the weld parameters, Figure 8-1. Each test specimen consisted of a 316L stainless steel porous segment the same thickness as the nosetip, and a 321 stainless steel segment machined to the baseplate configuration. The dimensions were chosen to provide a volume sufficient to simulate the heat-affected zone of the full-scale parts. The weld conditions were selected to yield a full penetration weld as shown by the microstructure in Figure 8-2.
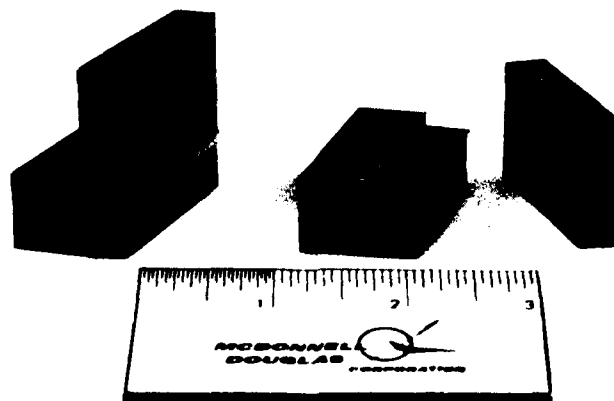
Figure 8-1. Test Specimens for Electron Beam Welding

MCDONNELL DOUGLAS
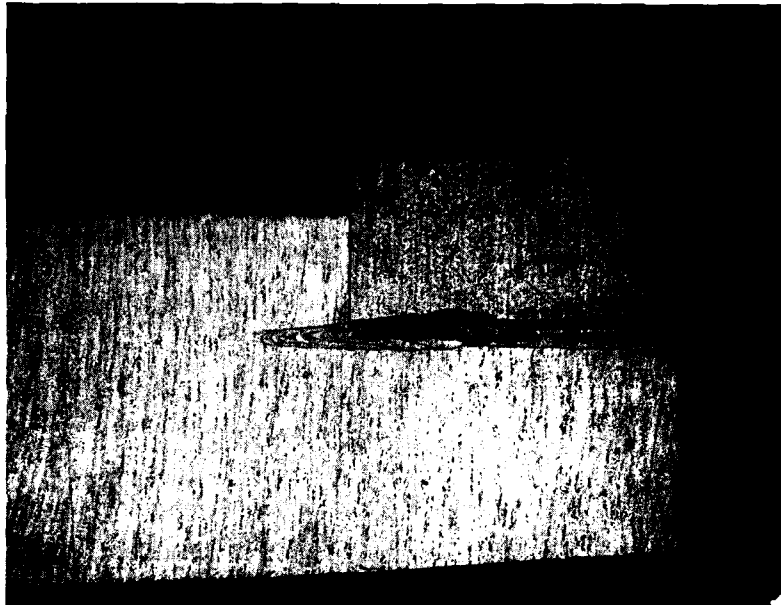
Figure 8-2. Electron Beam Weld Showing Full Penetration

Prior to welding, the porous 316L stainless steel was outgassed in a hydrogen atmosphere at $1800^\circ F \pm 25^\circ F$ for 1 hour. This heat treatment was essential to prevent outgassing of the porous material in the vacuum weld chamber.

The fillerless welding of porous materials frequently results in severe undercut because the resolidified weld metal occupies a smaller volume than the original porous material. Therefore, to provide additional molten material to the weld, a small lip measuring 0.020 by 0.020 inch was machined on the mating edge of the simulated baseplate, Figure 8-1. This resulted in minimum weld undercut, as shown in Figure 8-2.

8.2 WELDING OF NOSETIPS

The electron beam welding of the three nosetips to the baseplates was accomplished at Radcliffe Engineering in Pasadena, California. Prior to welding, all of the nosetips were outgassed at $1800^\circ F \pm 25^\circ F$ for 1 hour in hydrogen gas. Each nosetip was then placed in the teflon lined fixture, shown in Figure 8-3, in preparation for welding. This fixture maintained the alignment between the nosetip and baseplate and also provided a means of rotating
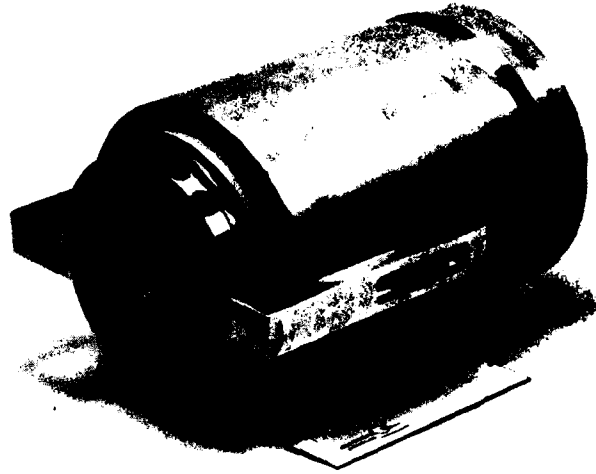
56

Figure 8-3. Nosetip in Welding Fixture

the part during welding. After assembly, several tack welds were made followed
by the welding of the flat segment. The assembly was then removed from the
welding chamber to reposition the tooling, thus providing clearance for making
the circumferential weld. An as-welded nosetip is shown in Figure 8-4. Follow-
ing welding, the weld areas were machined to remove the weld bead and undercut
that was present. The machined porous material in the weld area was shot
peened to close the surface pores and thus prevent loss of coolant during
ground testing. Shot peening was done with size 12 glass beads at 25 psi.

8.3 NITROGEN GAS FLOW DISTRIBUTION

Each nosetip was flow checked after chemical milling to verify that all
of the disturbed metal was removed from the surface and that the distribution
of flow on the nosetip was acceptable. The method used to check the gas flow
distribution is shown in Figure 8-5. A locating band was placed on the nosetip
and point flow measurements were made at the indicated positions on the band.
The band was then relocated at eight equally spaced positions around the cir-
cumference of the nosetip. All measurements were made using nitrogen gas at a
pressure of 30 psia. The flow distributions for nosetips 6N and 7N are given
in Tables 8-1 and 8-2. Also shown are the circumferential flow averages at
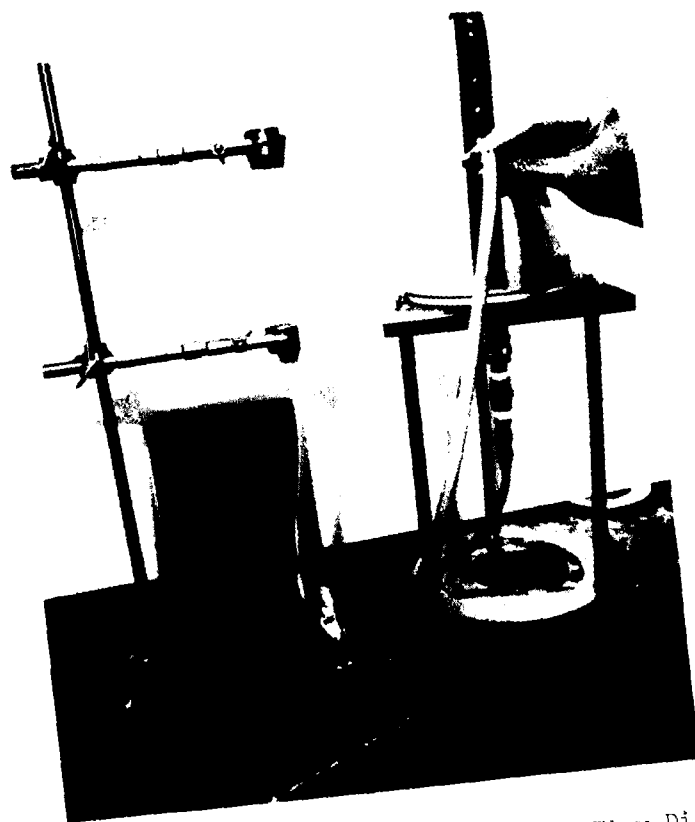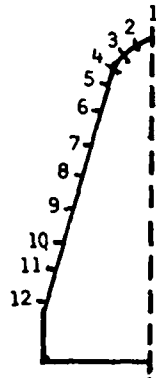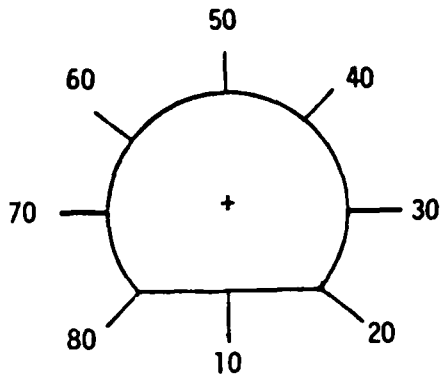
57

Figure 8-4. As-Welded Nosetip

Figure 8-5. Method Used to Measure Nitrogen Gas Flow Distribution Over Surface of Nosetip

58

Table 8-1. Laboratory Flow Check – Nosetip 6N

$\Delta P = 30 \pm 1$ psig

disc permeability

TOP 0.80 $(10)^{-10}$ in^2

BOTTOM 0.73 $(10)^{-10}$ in^2

LOCATION	STANDARD CUBIC CENTIMETERS PER MINUTE (SCCM)								AVG
	10	20	30	40	50	60	70	80	
1	40	40	42	41	41	42	42	42	41.2
2	47	49	49	47	45	49	49	46	47.6
3	33	32	36	36	30	36	32	37	34.0
4	21	24	22	25	22	22	24	25	23.1
5	18	18	20	19	18	17	18	18	18.3
6	21	21	18	18	17	17	17	17	18.3
7	22	19	18	20	18	20	24	22	20.4
8	(24)	(22)	20	17	19	21	21	(22)	19.6
9	(21)	(19)	24	18	20	20	21	(20)	20.6
10	(22)	(24)	20	17	19	21	19	(18)	19.2
11	(24)	(19)	19	18	20	21	21	(19)	19.8
12	(20)	(22)	19	22	21	26	27	(16)	23.0

( ) ON FLAT

MCDONNELL DOUGLAS

Table 8-2. Laboratory Flow Check – Nosetip 7N
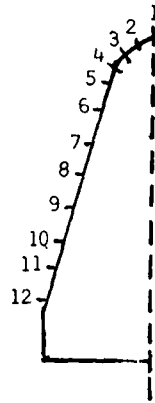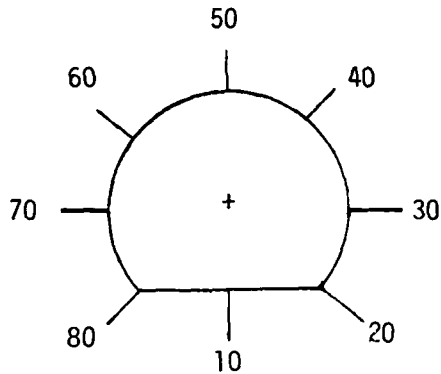
$\Delta P = 30 \pm$ psig

DISC PERMEABILITY 0.83 $(10)^{-10}$ in^2

CALCULATED
PERMEABILITY 0.57 $(10)^{-10}$ in^2

LOCATION	STANDARD CUBIC CENTIMETERS PER MINUTE (SCCM)								AVG
	10	20	30	40	50	60	70	80	AVG
1	45	45	47	46	47	49	46	45	45.9
2	55	57	54	55	55	54	50	57	54.6
3	37	38	33	37	35	36	32	31	34.8
4	24	22	22	22	21	26	18	22	22.1
5	19	20	17	17	16	16	17	18	17.5
6	17	18	16	18	19	15	14	15	16.5
7	24	24	25	21	21	21	21	25	22.8
8	(22)	(18)	18	21	17	17	19	(19)	18.4
9	(22)	(19)	17	19	21	16	19	(16)	18.4
10	(26)	(21)	21	18	19	17	20	(17)	19.0
11	(22)	(21)	20	18	20	20	17	(17)	19.4

( ) ON FLAT

MCDONNELL DOUGLAS

each axial location on the nosetip. Flow data taken on the flat portion of the nosetip are shown in parentheses. These data are not included in the circumferential averages.

Figure 8-6 and 8-7 show the measured flow distribution compared to theory for nosetips 6N and 7N, respectively. The theoretical flow distribution was calculated using the permeability coefficients of discs taken from each end of the nosetip billet (see Table 6-2) and measured wall thickness. Figure 8-6 shows good agreement between measured and theoretical flow rates except at the first two measurement locations (the stagnation point and about 30° from the stagnation point). Figure 8-7 shows the results for nosetip 7N. The permeability deduced from the discs was 0.83×10^{-10} in^2. Using this value to predict the nosetip flow distribution results in a significant difference between predicted and measured flow distribution, but does show the shape of the distribution along the cone to agree with theory. The use of a permeability of 0.57×10^{-10} in^2 results in good agreement with the test data along the cone, but over-predicts the flow at the first two locations on the hemisphere; the same phenomena noticed on nosetip 6N. These points are located at the bottom of the cylindrical inner nosetip contour. It is possible that the etchant solution became stagnated in this region producing a depleted etchant layer adjacent to the nosetip surfaces. This stagnation would produce a reduction in etching rate and an incomplete removal of smeared metal in this region.
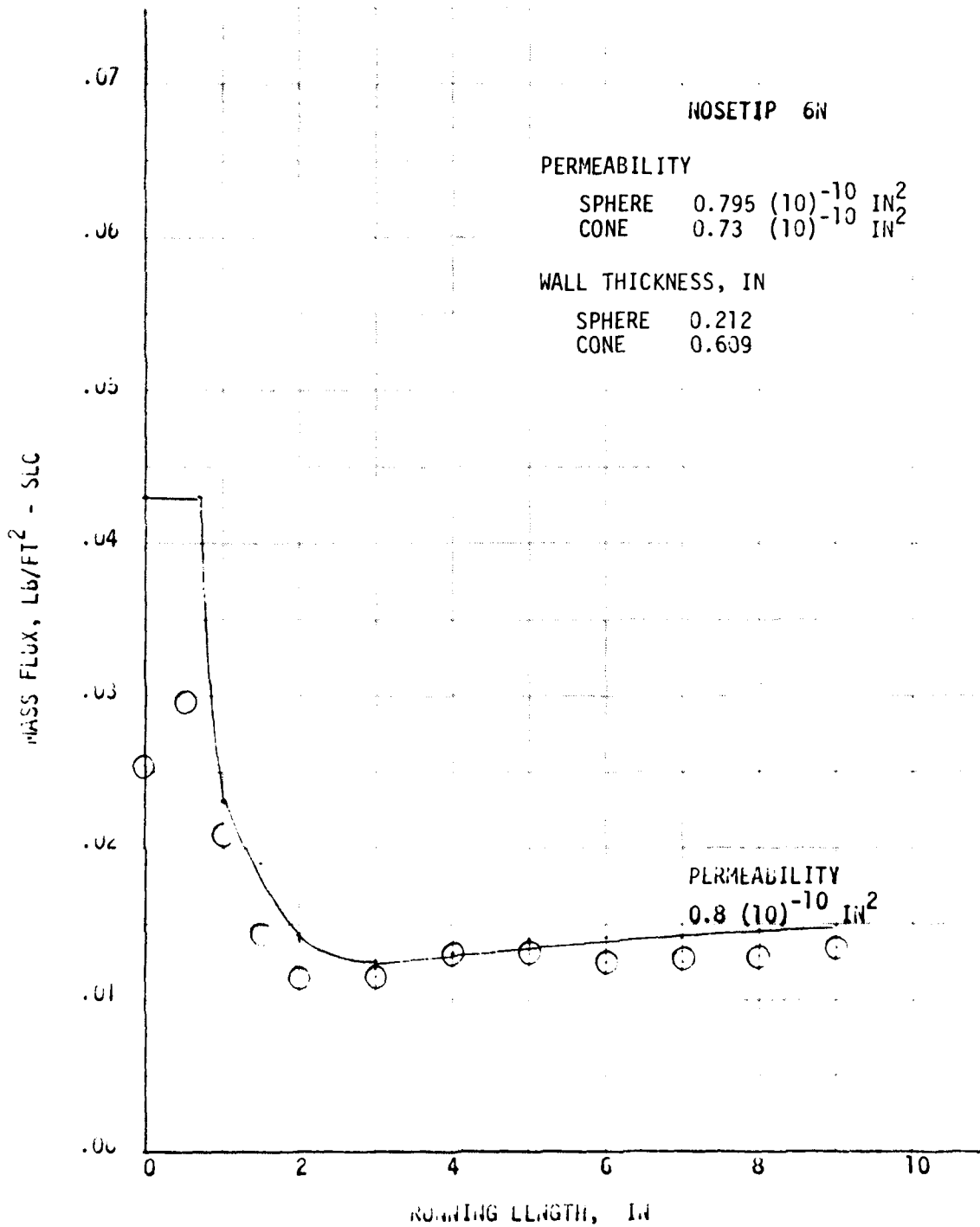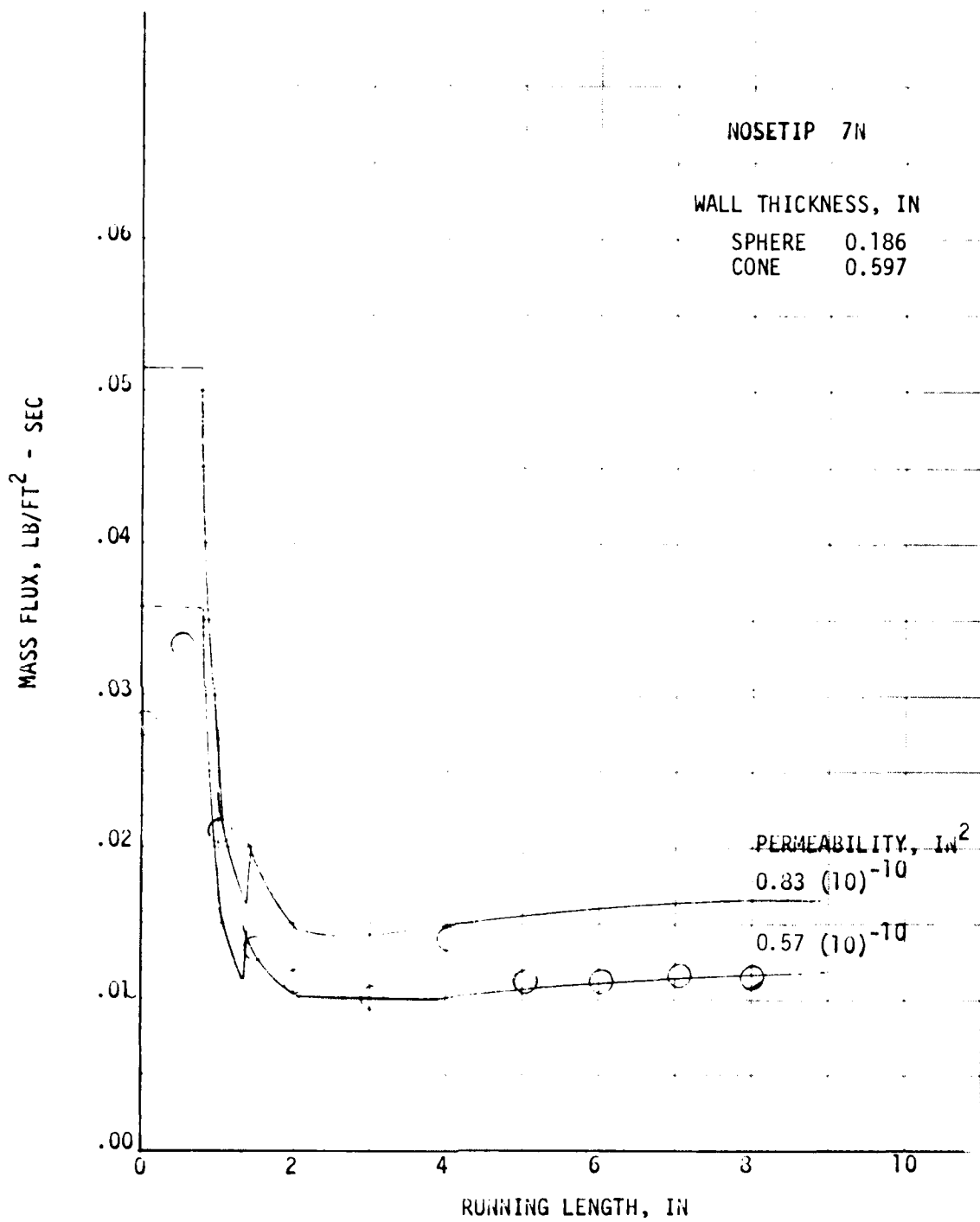
MCDONNELL DOUGLAS

Figure 8-6. Laboratory Flow Check, Nosetip 6N

Figure 5-7. Laboratory Flow Check, Nosetip 7N

63

MCDONNELL DOUGLAS

Section 9
GROUND TEST

Nosetips 6N and 7N were designated for ground tests simulating the thermodynamic environment expected in flight. The "13 atm nozzle" at the Edwards Air Force Base Rocket Propulsion Laboratory was selected for the test because its environment was a good match to flight and the cross-section of the rocket exhaust plume was sufficient to completely immerse the nosetip in a shock free environment. Table 9-1 compares the test environment to flight, while Figure 9-1 compares the heating distributions about the nosetip. The thermal environment of the test was more severe than flight in both severity and integrated heating.

Table 9-1. RPL Test Environment Versus Flight

	RPL	Flight*
Mach Number	3.89	
Propellant	LOX/Benzonitrile	Air
Chamber Pressure (atm)	200	--
Stream Total Temperature (°R)	7165	6300
Total Enthalpy (Btu/lb)	4000	2091
Exit Diameter (inches)	17	--
Stagnation Pressure (atm)	17	16
Test Time (sec)	8-10	6
Cold Wall Heat Flux - Cone (Btu/ft^2-sec)	2200	500-1500
Stagnation Heat Flux (Btu/ft^2-sec)	4500	2000

*Altitude 50 kft
 Velocity 10 kft/sec

65

MCDONNELL DOUGLAS
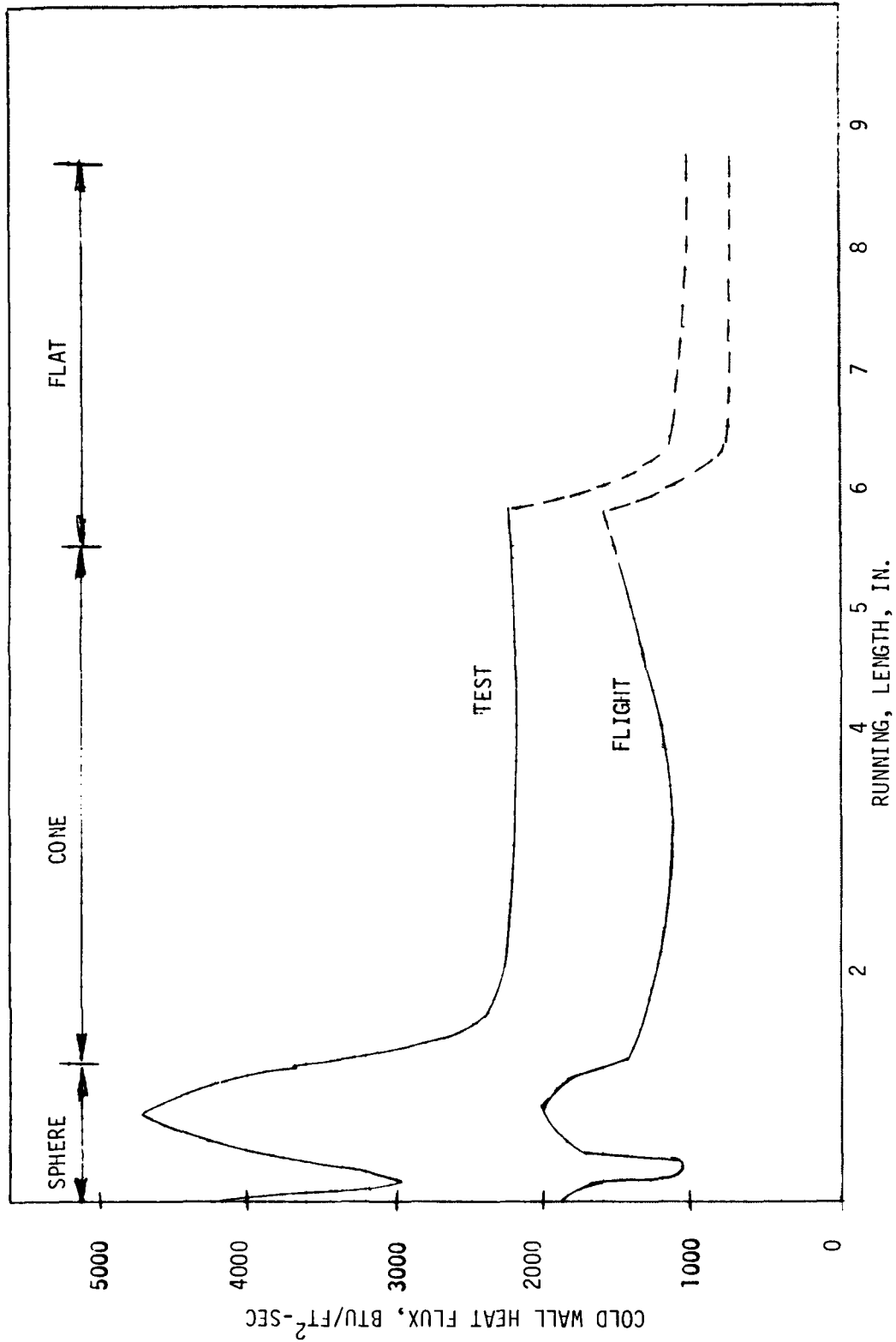
Figure 9-1. Heat Transfer Distribution – Test Versus Flight

MCDONNELL DOUGLAS

Three tests were conducted: a calibration model at ten degrees angle of attack, and two transpiration nosetips – one at zero degrees angle of attack and one at 10° angle of attack. Table 9-2 shows the test matrix.

Table 9-2. Test Matrix

Test	Test Name	Angle of Attack	Flow Rate lb/sec	Pressure psia
1	Calibration	10°	--	--
2	TCNT	0°	1.64 1.41	7.2 627
3	TCNT	10°	3.24 2.83 2.25	1165 1010 810

9.1 CALIBRATION TEST

Acurex Corporation designed and fabricated the calibration model. The copper model in the identical external configuration of the nosetip contained 15 null-point calorimeters and 15 pressure taps (Figure 9-2). Five calorimeters and five pressure transducers were located on the flat portion of the nosetip. The other sensors were placed along the windward, leeward and yaw rays of the nosetip.

The calibration test sequence was to start the engine, inject the model into the rocket exhaust centerline, hold for 0.4 seconds, withdraw the model and finally shut down the engine. Figure 9-3 shows the model location history along with the facility chamber pressure and three pressure histories on the model. P1 was located on the hemisphere 45° from the model centerline; P2 was located at the hemisphere-cone tangency point and P3 was located on the cone windward ray at an axial distance of 2.625 inches from the front of the model.

Figures 9-4 and 9-5 show heat flux versus time for a hemisphere location and a location along the cone. Selecting the appropriate heat flux from this data without also considering the movement of the model across the rocket exhaust is difficult. Figures 9-6 and 9-7 show the heat flux plotted against lateral position of model. Generally, the model enters and exits the exhaust across an annulus of high heat flux. This region is hotter than the central

67

Figure 9-2. Calibration Model

MCDONNELL DOUGLAS
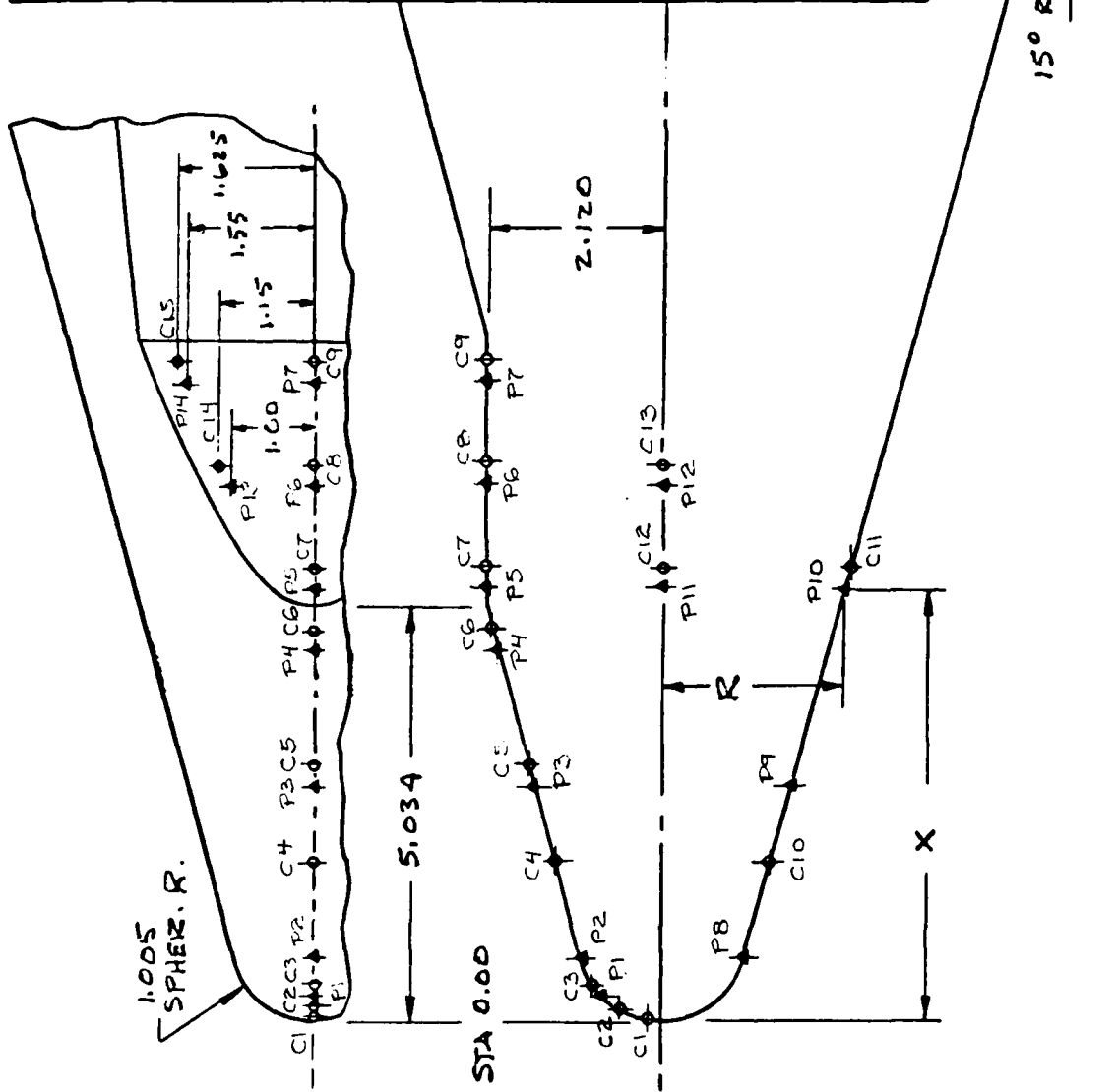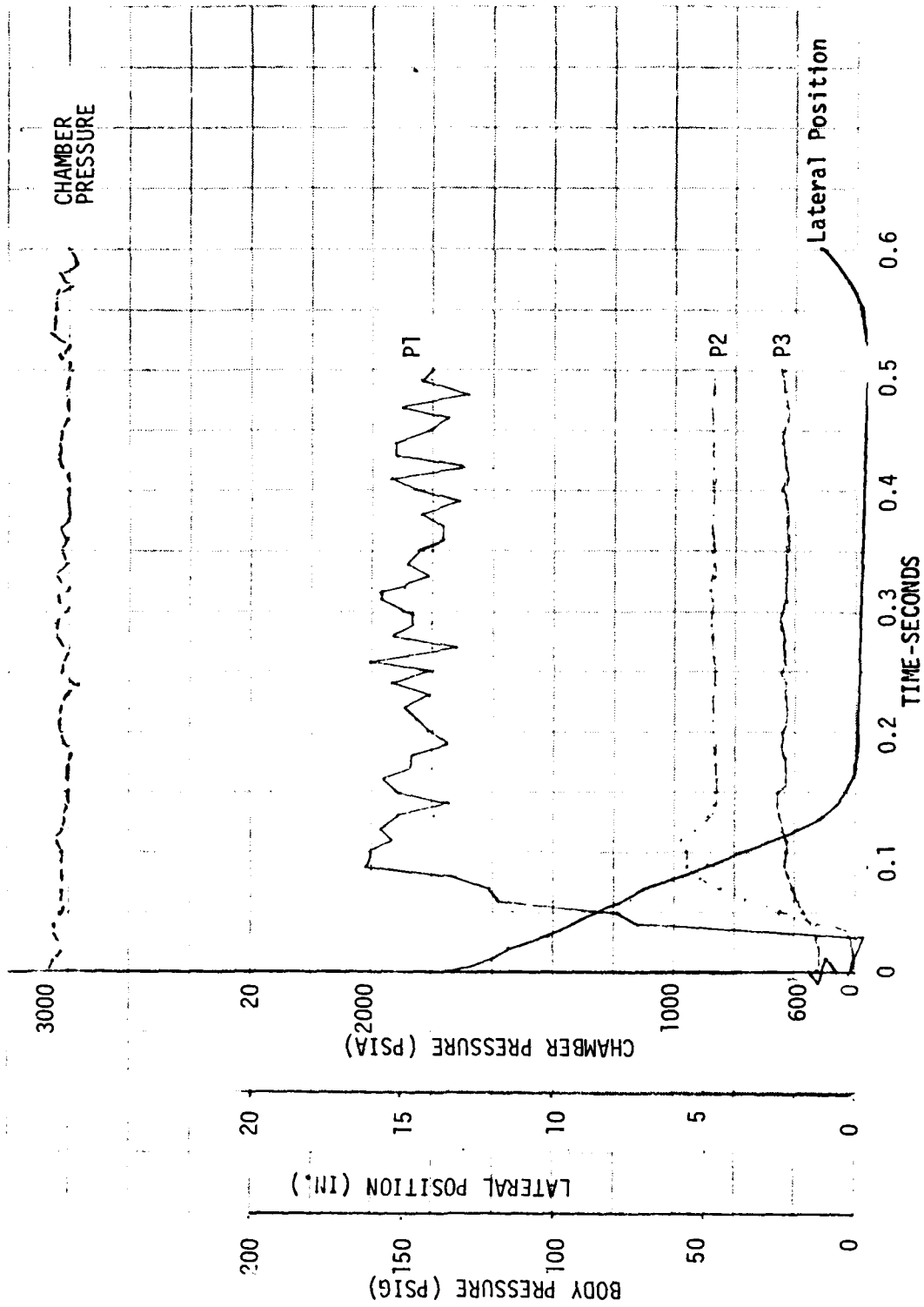
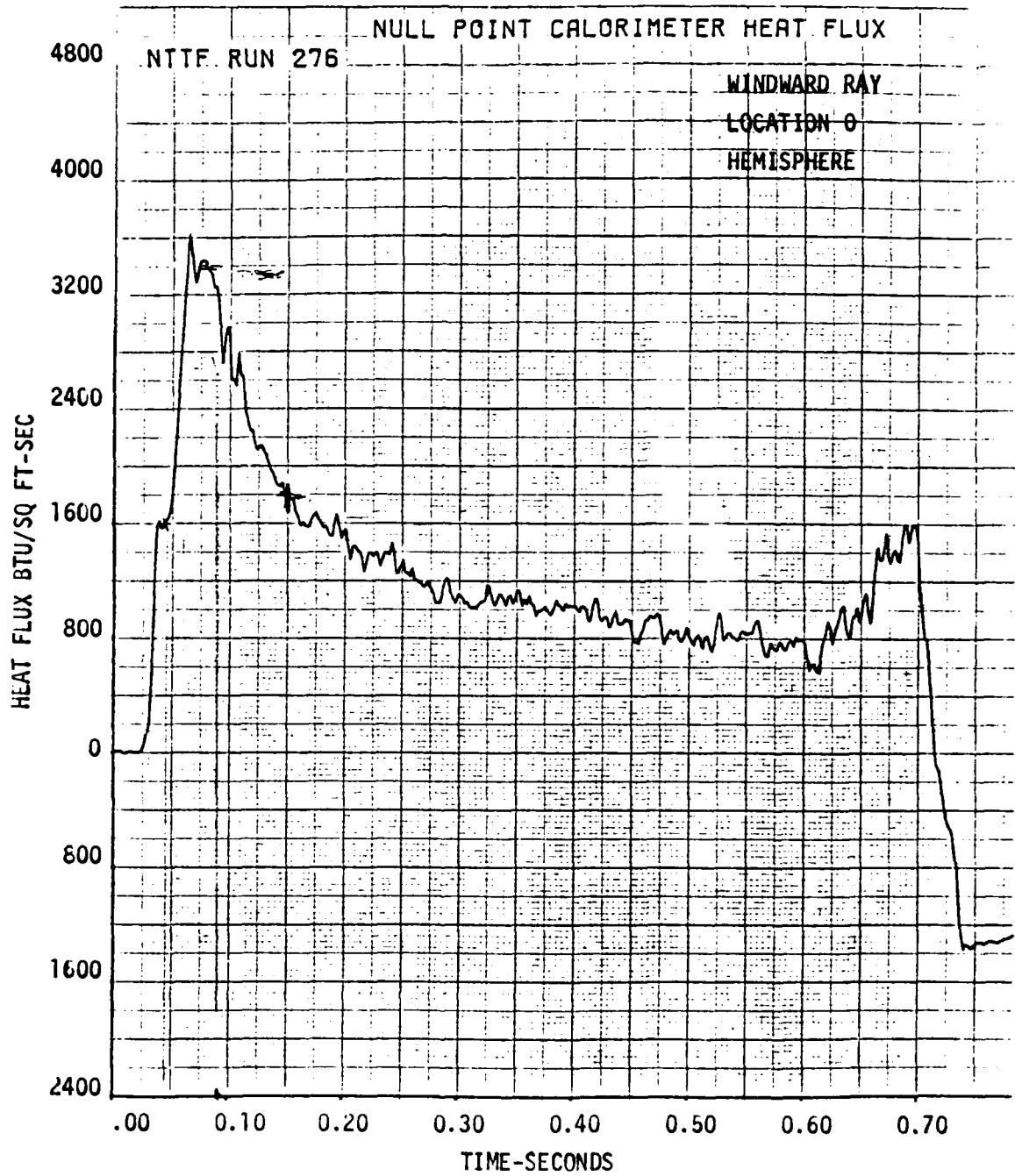Figure 9-3. Model Position Versus Facility Characteristics
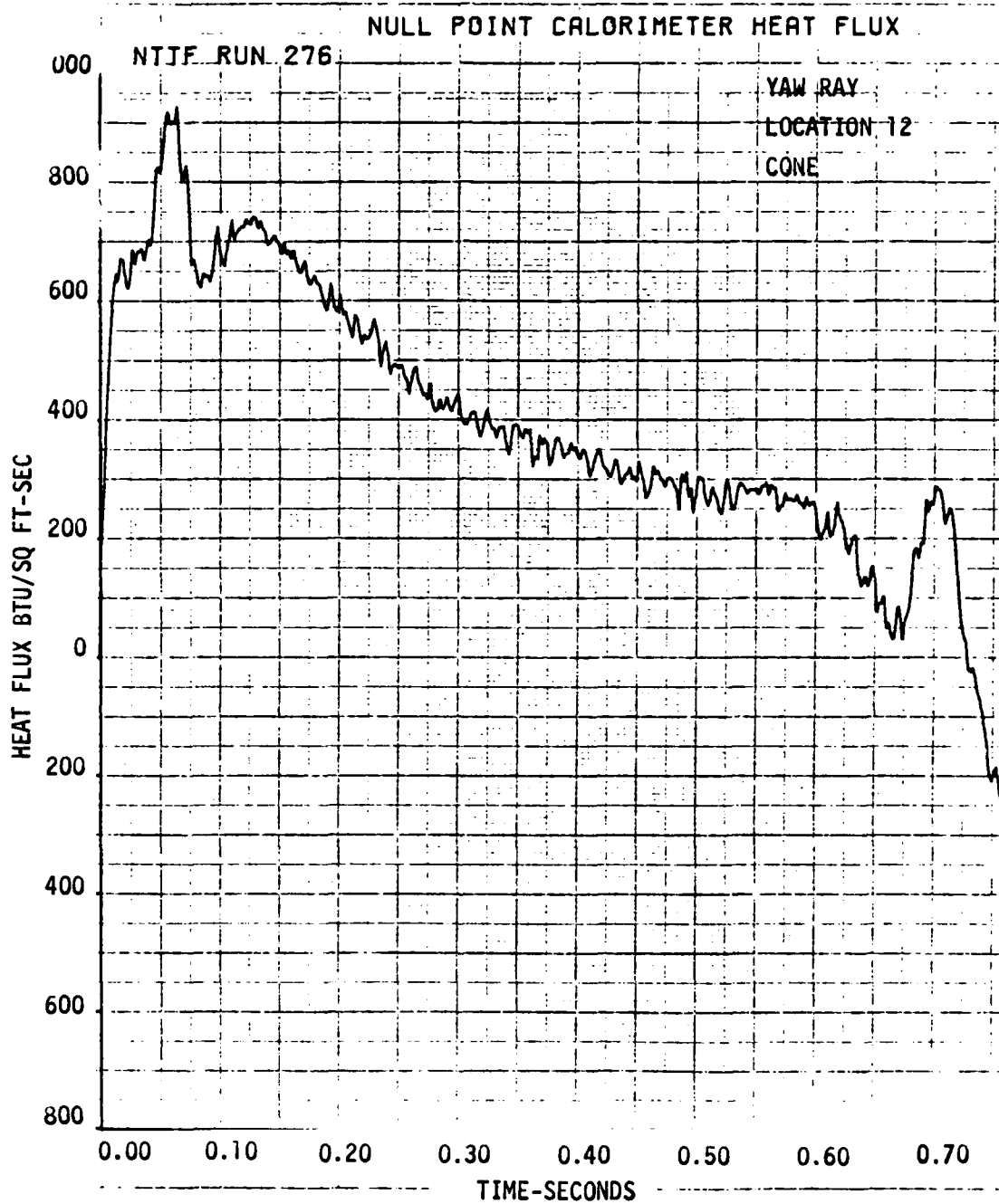
69

Figure 9-4. Typical Calibration Data — Hemisphere Heat Flux

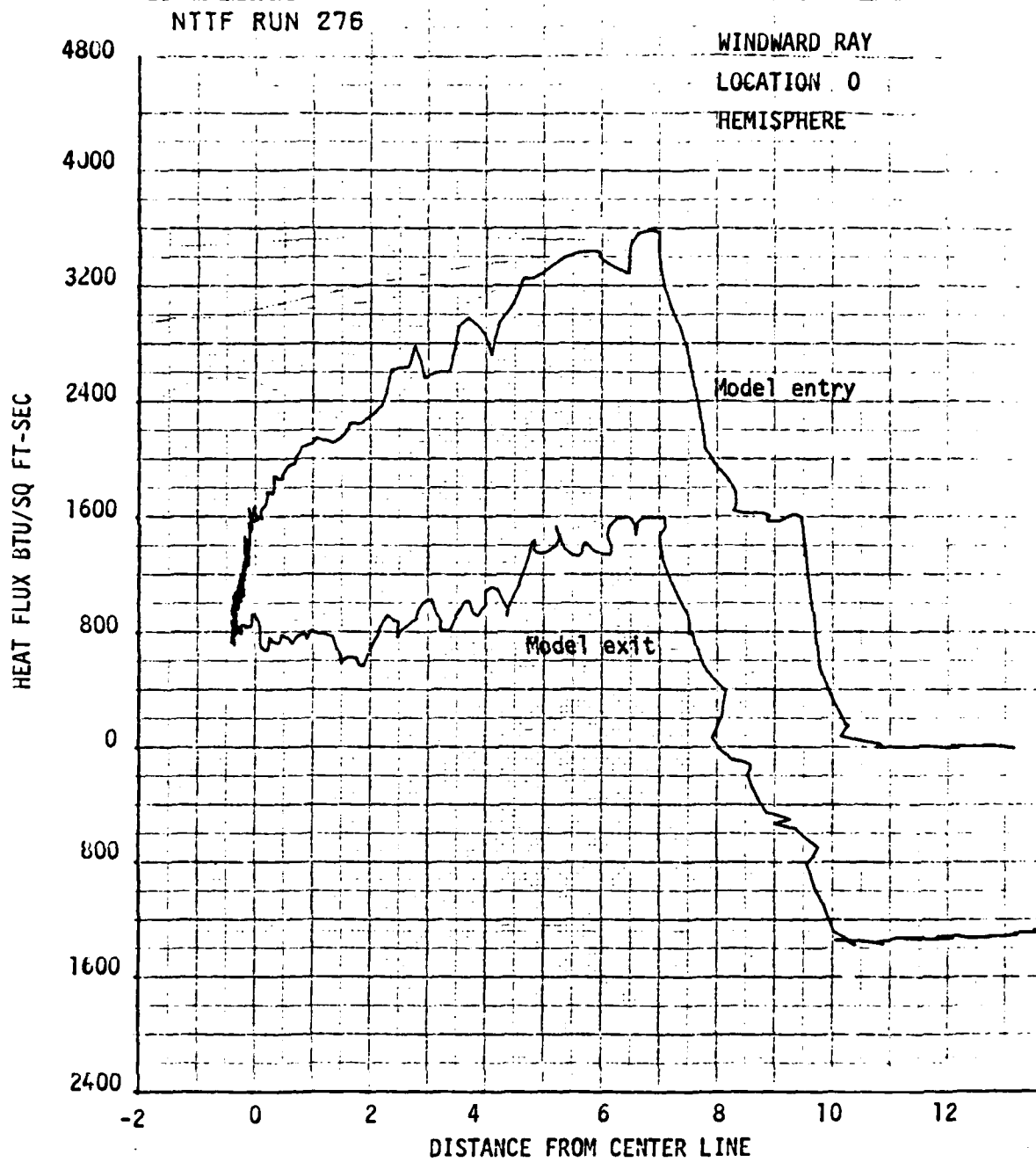Figure 9-5. Typical Calibration Data – Cone Heat Flux

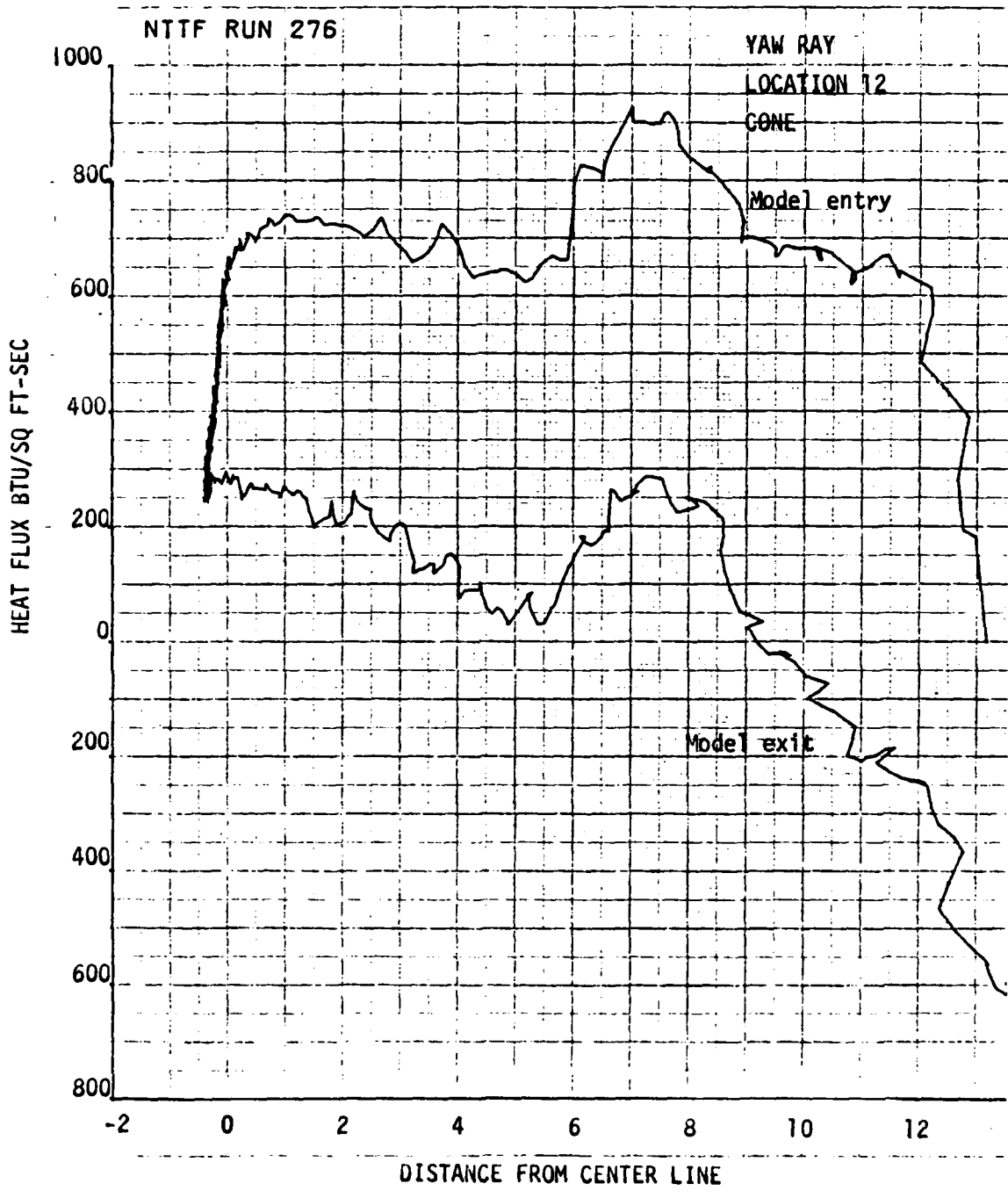Figure 9-6. Typical Calibration Data – Hemisphere Heat Flux Versus Position

MCDONNELL DOUGLAS

Figure 9-7. Typical Calibration Data — Cone Heat Flux Versus Position

73

MCDONNELL DOUGLAS

portion of the exhaust due to different chemical compositions of the exhaust products. Once the gauges have heated up, conduction to the surrounding model becomes important and the theory on which the heat flux is calculated becomes invalid. This shows in the data as reduced heat fluxes late in the test. Reviewing the transient heat flux data together with the heat flux versus model location data makes selection of appropriate values of steady state heat flux considerably easier, although an uncertainty band must be associated with each heat flux value. Figure 9-8 shows the windward ray heat flux distribution as deduced from the test data. Also shown are the predicted laminar and turbulent heating distributions for the facility operating conditions. (Rocket exhaust chemistry was included in prediction of facility heat flux distribution.) The data falls midway between laminar and turbulent heat transfer predictions, indicating that the environment is in transition between laminar and turbulent flow conditions.

Heat flux values in the presence of the transpiration nosetip should more closely approximate turbulent heating values because (1) the rougher wall of the transpiration nosetip tends to augment the boundary layer heating and (2) transpiration cooling tends to destabilize the boundary layer. For these reasons the turbulent heat transfer values were used in all calculations of nitrogen coolant requirements. Figure 9-9 shows the heat flux distribution predicted for 0° angle of attack. Pressure distributions for the windward, leeward and yaw positions about the nosetip are shown in Figure 9-10. The data fall somewhat lower than predicted along the cone. This is of no consequence in calculation of coolant flux delivered across the porous nosetip material because the internal nosetip pressure dominates the results. Figure 9-11 show the predicted pressure distribution for 0° angle-of-attack.

9.2 PROOF-TESTS

Coolant expulsion system checkouts were made using a third nosetip which was not tested in the rocket exhaust. Data showed that the coolant pressure levels required internal to the nosetip were nearly double those predicted for a given coolant flow rate. This data led to a review of the equations used to predict the coolant flow rate/nosetip pressure requirements for the test.

The flow resistance of the porous nosetip is made up of a viscous and inertial term. Experience with liquid coolants has shown that the viscous term
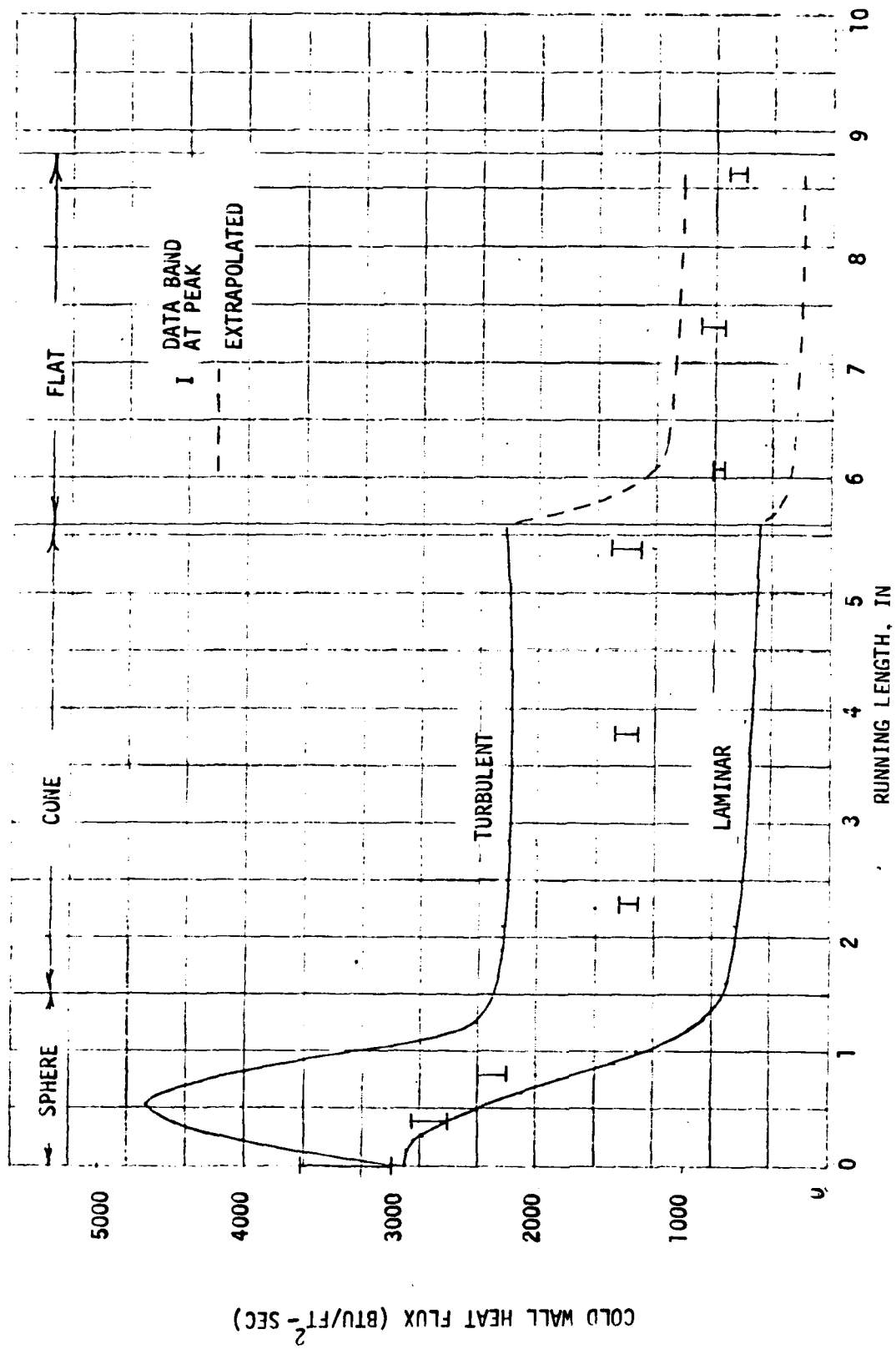
MCDONNELL DOUGLAS

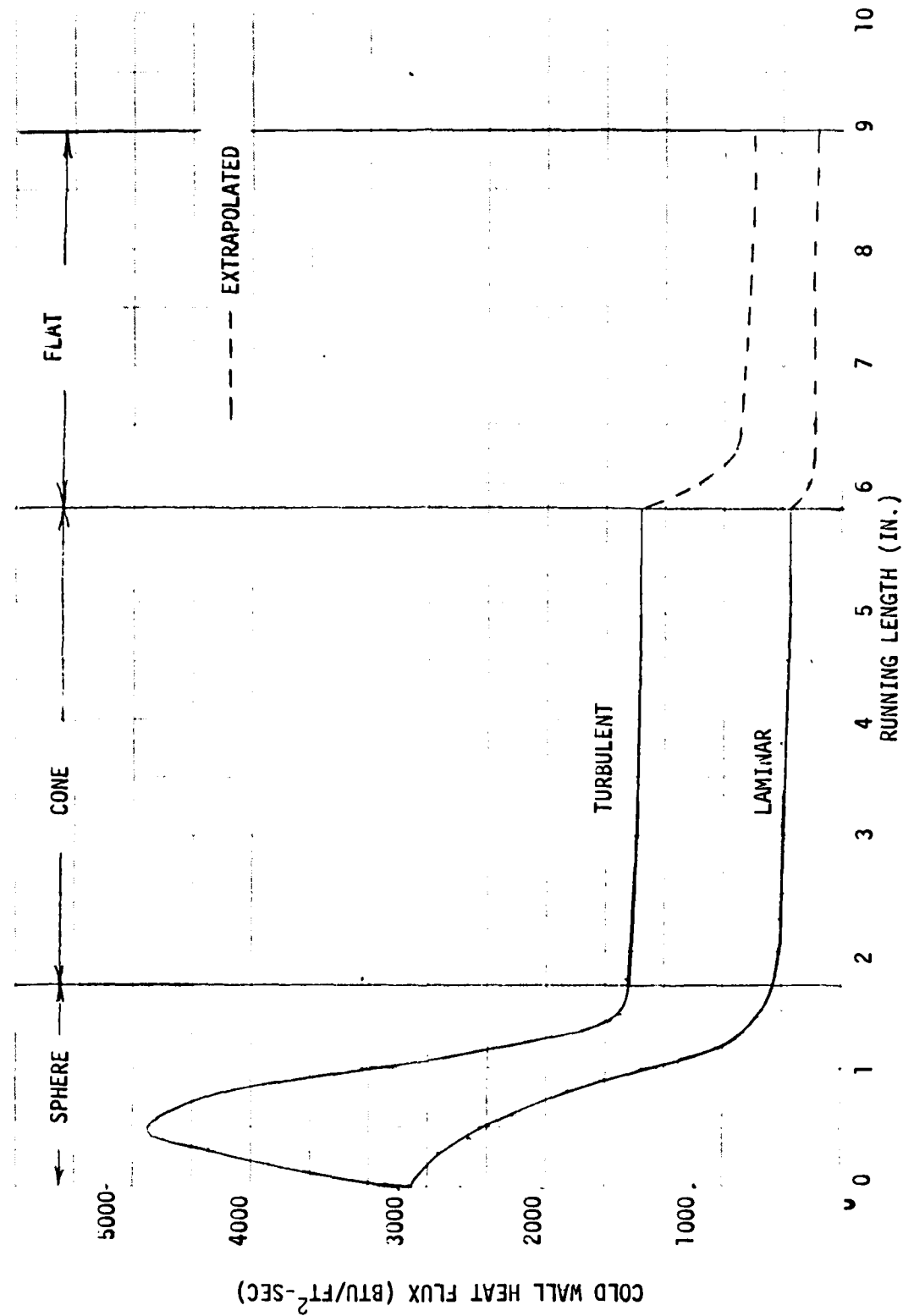Figure 9-8. Heat Transfer at 10-Deg Angle of Attack (Windward)

75

Figure 9-9. Heat Transfer at 0-Deg Angle of Attack (0-Deg Plane)

76

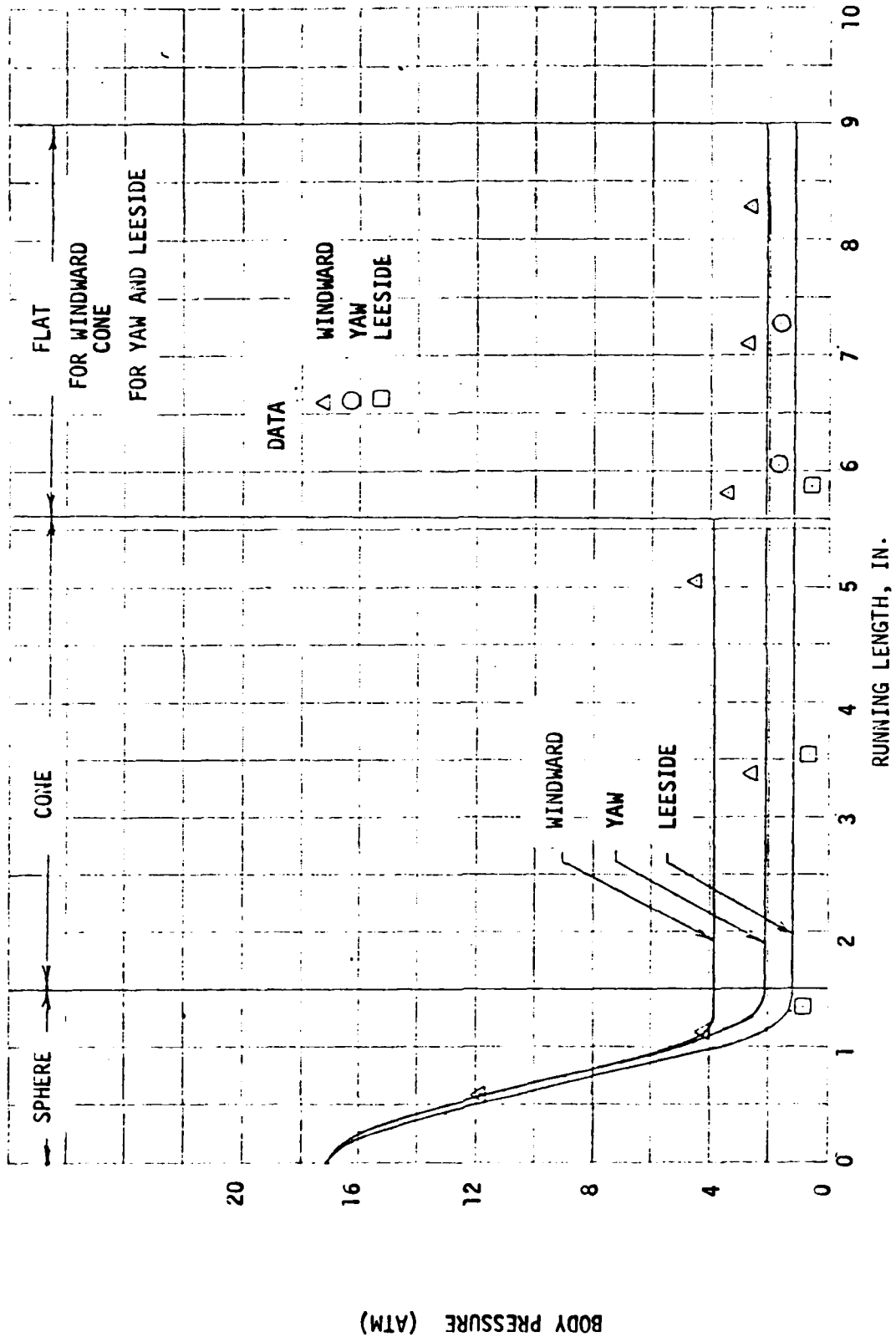MCDONNELL DOUGLAS

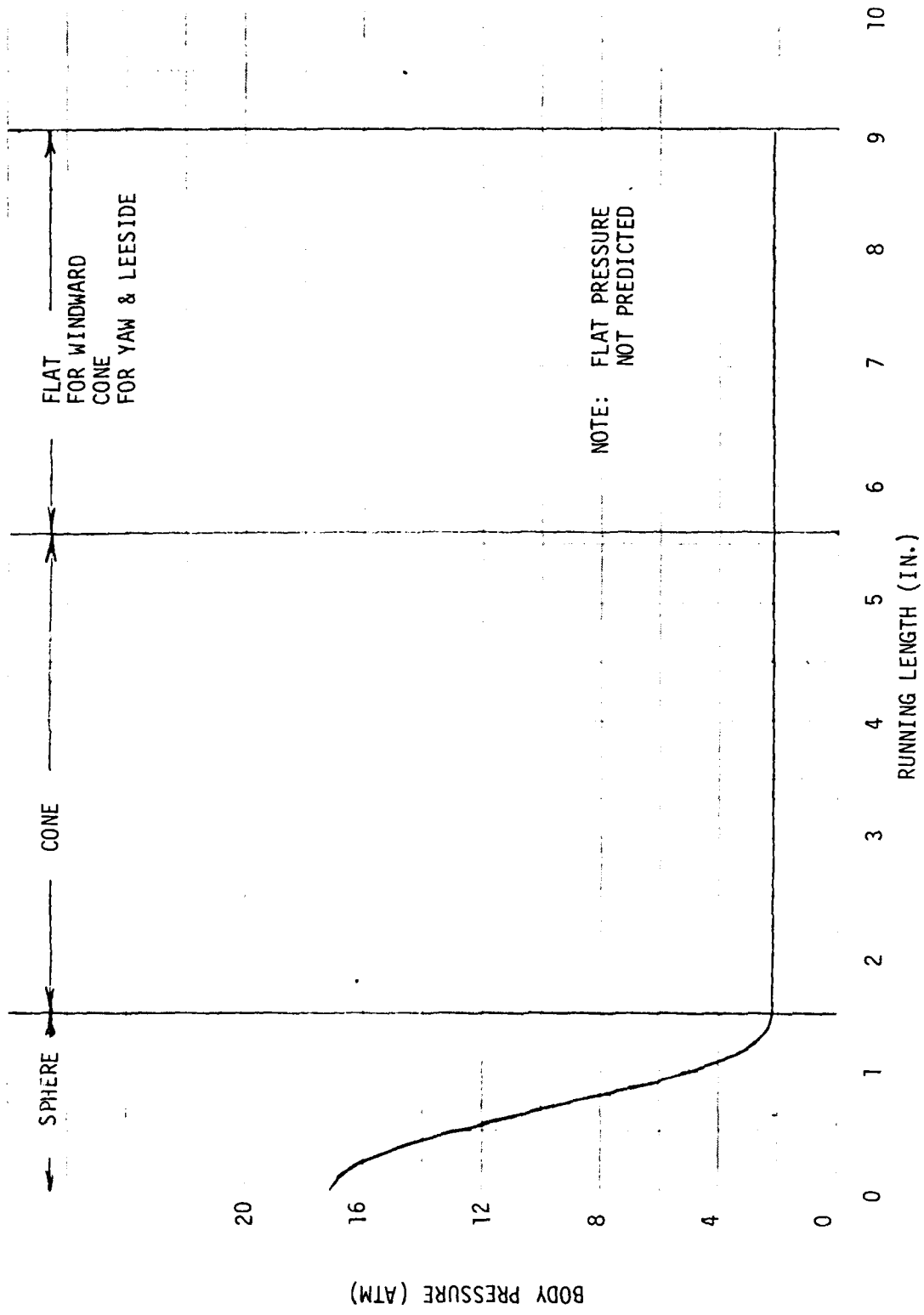Figure 9-10. Pressure Distribution at 10-Deg Angle of Attack

77

Figure 9-11. Pressure Distribution at 0-Deg Angle of Attack

78

MCDONNELL DOUGLAS

represents about 80% of the pressure drop across the nosetip; thus, preliminary design work is done using only the viscous flow resistance term. The calculations of Section 2 and the flow calculations for the ground test were done on this basis.
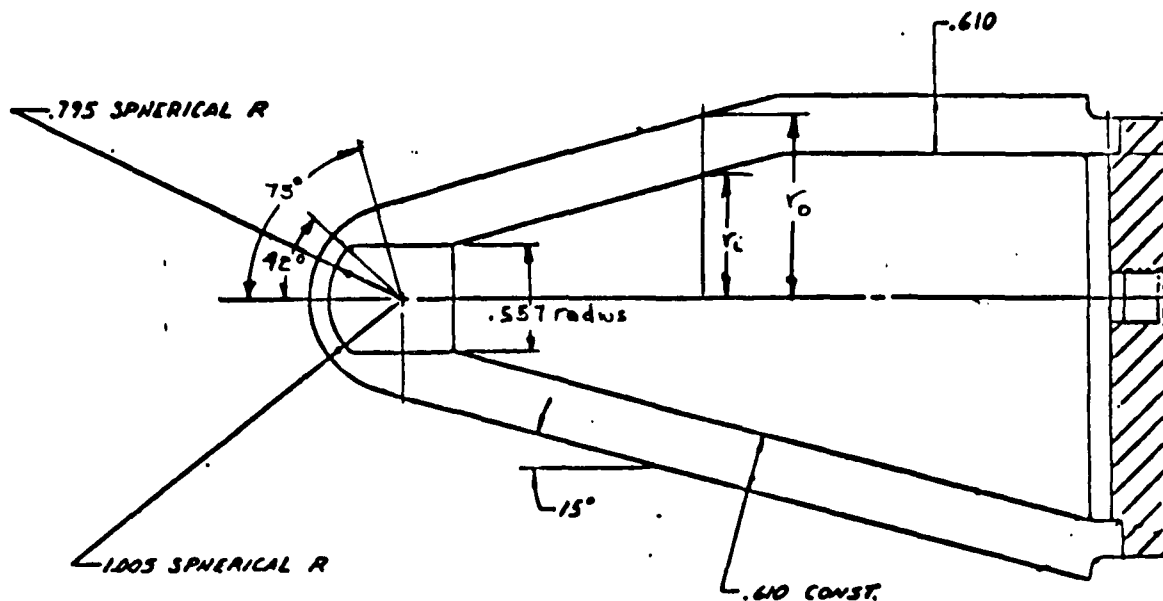
After the check-out data on the "third" nosetip indicated high pressure drops, calculations were re-done including both the viscous and inertial terms. The inertial term represents about 50% of the pressure drop across the nosetip. This is not surprising since the velocity of the gaseous nitrogen passing through the nosetip is about 30 times greater than that of an equal mass of liquid water. A review was then conducted to determine if the nosetip could handle higher internal nosetip pressures than 500 psia.

In Section 2, it was noted that the weld area was the weakest portion of the nosetip. The margin on yield strength at 500 psia is 1.19 and on ultimate strength is 1.78 while at 750 psia the predicted margin of safety drops to 0.79 on yield and 1.19 on ultimate strength. At about 900 psia, the ultimate strength margin goes to 1.0.

It is recognized that the simplified analysis done according to the equations of Roark (see Section 2.7) is very conservative and therefore it is likely that considerably higher internal nosetip pressures could be used without yielding the nosetip. In order to prove that high nosetip pressures could be achieved without damage, the third nosetip was proof tested to 700 psia prior to the zero degree angle of attack transpiration test and the same nosetip was proofed to 1400 psia before the 10° angle of attack test. Neither proof test revealed evidence of yielding; therefore, the first transpiration nosetip was tested at 702 psia and the second nosetip at 1165 psia. It is recommended that a more sophisticated computer simulation of the nosetip be conducted to get a better understanding of nosetip margins of safety.

9.3 PERFORMANCE PREDICTIONS

A one-dimensional flat plate analysis was used in Section 2 to calculate the coolant distribution about the nosetip as a result of flow through the porous nosetip, because at that time the exact geometry of the nosetip was not defined. Analysis of the RPL ground test considered the effects of the internal and external nosetip contours on flow distribution. Figure 9-12 shows the equations used for each section of nosetip. The zero to 42 degree portion of

79

SPHERE

$$\frac{\Delta P^2}{2RT} = \frac{\alpha\mu W}{4\pi}\left(\frac{r_0 - r_i}{r_0 \, r_i}\right) + \frac{\beta}{3}\frac{W^2}{9_c \, 16\pi^2} \cdot \left(\frac{1}{r_i^3} - \frac{1}{r_0^3}\right)$$

$0° \le \theta \le 42°$ $\quad r_i = .795$in., $\quad r_0 = 1.000$ in.

$42° \le \theta \le 75°$ $\quad r_i = .557$in./sin θ, $\quad r_0 = 1.000$ in.

CONE

$$\frac{\Delta P^2}{2RT} = \frac{\alpha\mu W}{2\pi}\ln\left(\frac{r_0}{r_i}\right) + \frac{\beta W^2}{9_c \, 4\pi^2}\left(\frac{1}{r_i} - \frac{.1}{r_0}\right)$$

ΔP^2 LOCAL PRESSURE DROP
α VISCOUS FLOW COEFFICIENT
β INERTIAL FLOW COEFFICIENT
r_0 OUTER RADIUS
r_i INNER RADIUS
W COOLANT FLOW RATE
μ VISCOSITY

Figure 9-12. Porous Matrix Flow Equations

the nosetip is made up of concentric hemispheres and was treated as such. The
hemisphere region between 42 and 75 degree has a spherical outer contour and a
cylindrical inner contour. Points along this body were calculated using the
spherical flow equation and a variable inner radius. Finally, points along the
cone were calculated using the cylindrical version of the flow equation and
the local values of the inner and outer radii.

80

9.4 ZERO DEGREE ANGLE OF ATTACK TEST

The first transpiration test was conducted at zero degrees angle of attack. Figure 9-13 shows an overview of the test facility. The model is in the pre-insertion position.
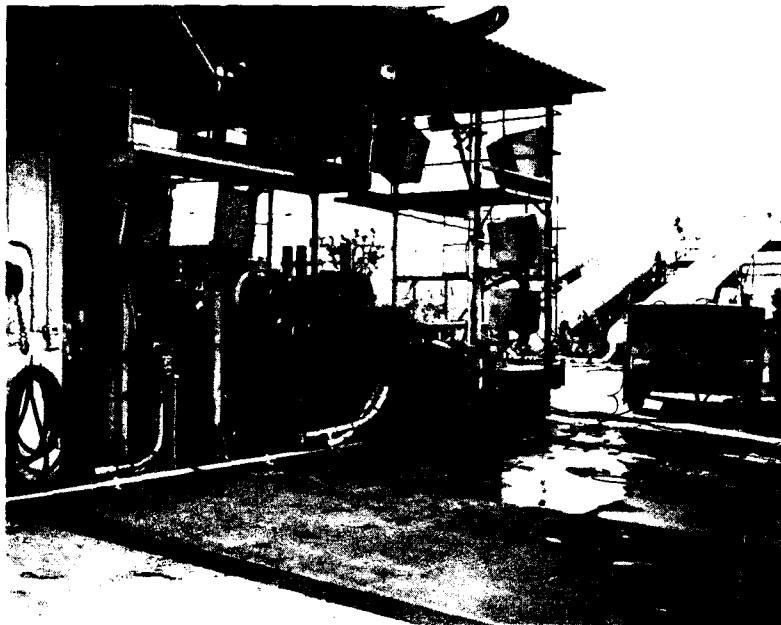

Figure 9-13. Rocket Propulsion Laboratory Test Facility

Coolant was initiated to the model prior to model insertion into the rocket exhaust. The model was covered with a teflon boot to protect the nosetip against transient facility start-up conditions. The initial coolant flow rate, 1.64 lb/sec at 705 psia internal nosetip pressure, was programmed for 5 seconds and a second flow rate of 1.41 lb/sec was programmed for 3 seconds. The teflon boot was designed to break free of the nosetip in two seconds; thus, providing three seconds of thermal environment to the nosetip at 1.64 lb/sec. Actual boot removal occurred in about 0.25 second.

Engine shutdown occurred with the model still in its test position. Post-test analysis showed that sooting and substantial chemical reaction occurred between unburned fuel products and the stainless steel nosetip during shutdown. Figure 9-14 is a post-test photograph of the 0° angle-of-attack model. In addition, motion picture films show a black oxide deposit forming early in the test on the hemispherical portion of the nosetip. The oxide started at

81

MCDONNELL DOUGLAS

Figure 9-14.   Nosetip at $\alpha = 0°$ - Post-Test

several locations and spread until the entire hemisphere was black. Melt
occurred on the hemisphere one half second into the second (lower) flow rate.
No oxidation or melt occurred on the cone.

Figures 9-15 and 9-16 shows the predictions of nosetip surface tempera-
ture distribution for the two nitrogen coolant rates employed. The tempera-
tures were predicted using one-dimensional transpiration theory for boundary
layer heat transfer effects, coupled with one-dimensional equations for flow
in porous media. In the transpiration analysis, the wall temperature is a
function of the nitrogen flux delivered to the surface, the local heat trans-
fer coefficient, the local recovery enthalpy and the reservoir temperature of
the nitrogen. The mass flux, in turn, is a function of local geometry, local
boundary lay´ pressure, internal nosetip pressure, nosetip permeability (flow
resistance) ˌd temperature. Streamline curvature in the hemispherical region
due to the pressure gradient about the nosetip and temperature conduction from
the hot surface into the nosetip was not considered. Viscous and inertial per-
meability coefficients were based on disc values with the reduced flow of the
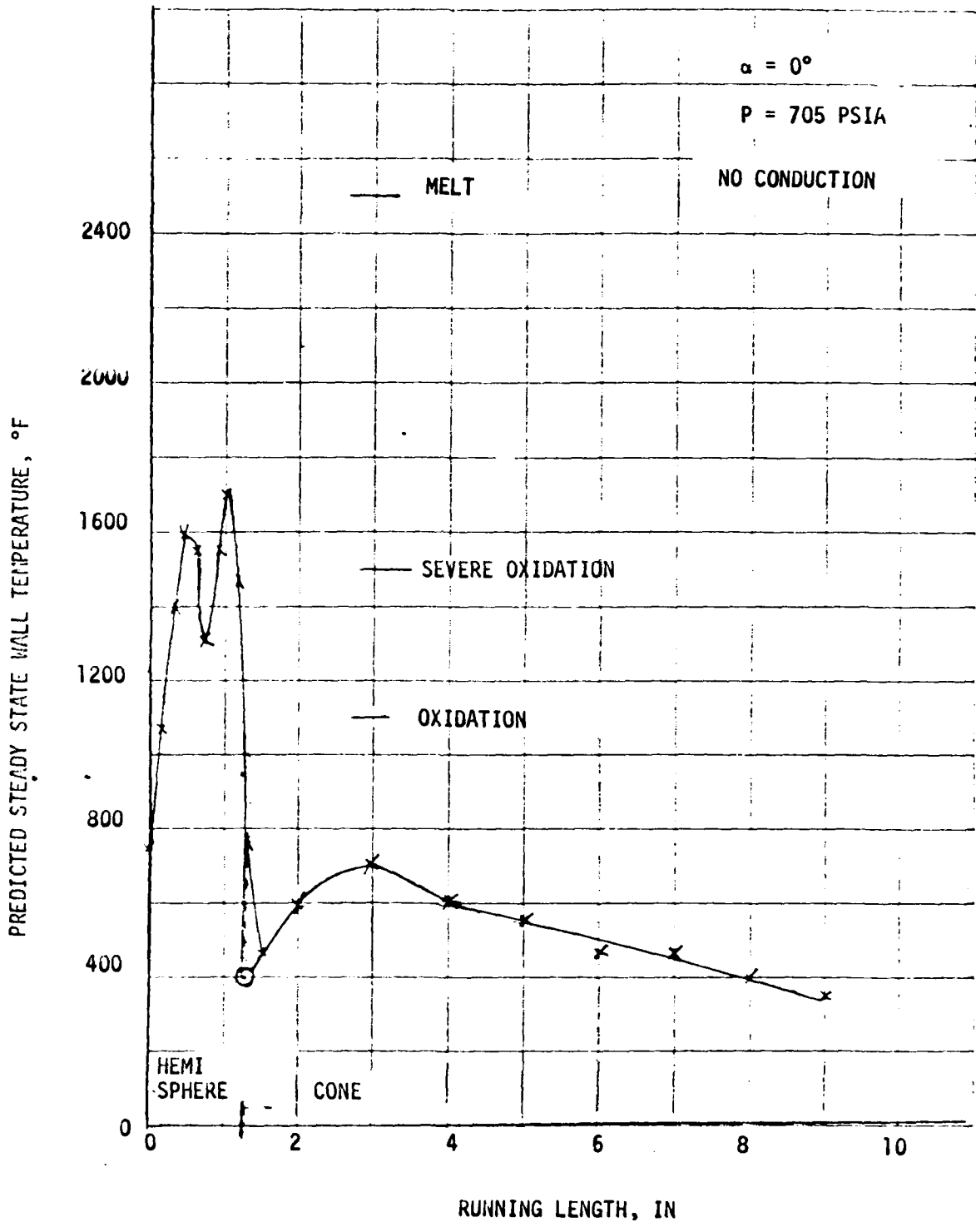hemisphere region (see Section 8-3) accounted for by increasing the viscous
coefficient.

82

Figure 9-15.   AMIRC TCNT Test 1 — W = 1.64 lb/sec
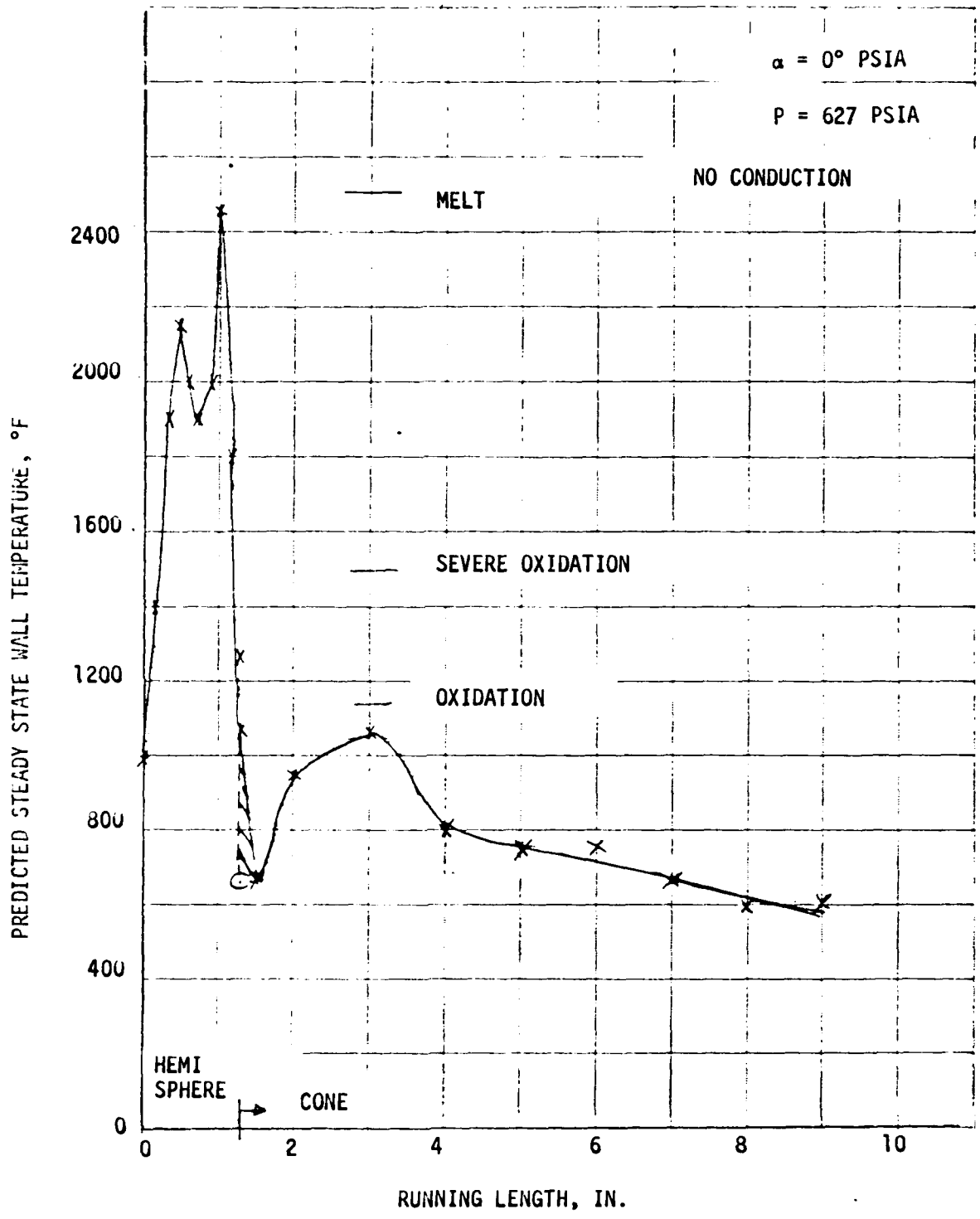
Figure 9-16. AMMRC TCNT Test 1 – W = .41 lb/sec

Figure 9-15 shows that for the first flow rate oxidation occurs on the hemisphere with the hottest location predicted to be between 0.5 - 1.0 inches (30° - 60°). This region oxidized first in the test. The cone is predicted to be well below the oxidation temperature, and indeed, did not oxidize in test. Predictions for the second flow rate, Figure 9-16, indicate temperatures close to melt in the 30° - 60° hemisphere region - the area where melt was initiated, and no melt or oxidation on the cone; a fact verified in the test. The effects of streamline flow and heat conduction on the hemisphere most certainly would increase the predicted temperatures into the melt regime.

9.5 TEN DEGREE ANGLE OF ATTACK TEST

The second transpiration test was conducted at 10° angle of attack using three coolant flow rates: 3.24 lb/sec at 1165 psia; 2.83 lb/sec at 1010 psia, and 2.25 lb/sec at 810 psia. The first flow rate was programmed for 5 seconds (2 seconds were allowed for boot removal), the second flow rate for 3 seconds and the third flow rate for 2 seconds. Actual boot removal for this test was 2.4 seconds.

Because of the problem encountered during the first transpiration test with sooting and chemical reactions between the exhaust products and the model during shutdown, the model was programmed to be removed from the exhaust prior to engine shutdown. Minimal sooting and no chemical reactions are visible in post-test examination of the nosetip (Figure 9-17). Post test examination of the nosetip revealed a very light brown discoloration (oxidation) 40 - 60° from the geometrical centerline of the nosetip and along the line forming the intersection of the "flat" and the cone. This discoloration could not be seen on the motion picture films. Figure 9-18 shows the pre-test temperature prediction for 1050 psia; a pressure slightly exceeding the pressure level utilized with the second flow rate condition. No oxidation was predicted. Figure 9-19 shows the predicted temperature distribution associated with the lowest flow condition, 2.25 lb/sec at 810 psia. The analysis does predict oxidation at the 60° location (1.05 inches from the model centerline); however, the analysis predicts the oxidation to be more severe than was observed on the model. The discontinuity at the cone-flat junction was not considered in the analysis.

Figure 9-17.   Nosetip at $\alpha = 10^\circ$ – Post-Test

9.6 UPDATED FLIGHT COOLANT REQUIREMENTS

Flight coolant requirements were redefined based on the results of the present program. The case evaluated was 10-kft/sec intercept at 50-kft altitude with a 15-deg angle of attack. The results affecting the flight coolant requirements were:

(1) The use of an $1150^\circ F$ design wall temperature rather than the $350^\circ F$ wall temperature used in the earlier analysis. (Nosetips in test were operated well into the oxidation regime without degradation in nosetip performance; thus, the use of an $1150^\circ F$ wall temperature is conservative.)

(2) The inclusion of the inertial-resistance flow coefficient in prediction of pressure drop across the nosetip. (This term was seen to be important at high flow rates during the ground test at RPL.)

(3) The hemisphere flow resistance was increased by decreasing the hemisphere permeability to account for the reduced hemisphere flow rates seen in laboratory tests (Section 8.3).

In addition, the analysis included the impact of spherical and cone geometry on flow across the nosetip and the variable wall thickness of the hemispherical portion of the nosetip. (The original analysis was one-dimensional.)

The calculations of Section 2 were repeated for the 50,000 foot altitude intercept at 15° angle of attack and 10,000 feet/sec case with the revised nosetip characteristics. Figure 9-20 shows the mass flux distributions about the nosetip as originally calculated and with the revised nosetip characteristics. The coolant flow rate to the nosetip has been reduced from 2.73 lb/sec to 1.42 lb/sec based primarily on the higher allowable surface temperature. The internal nosetip pressure is higher than originally planned (674 psia versus 532 psia) due to the inclusion of the inertial flow contributions to the nosetip permeability. The pressure, although higher than originally planned, is still acceptable. Figure 9-21 shows the temperature distribution about the nosetip predicted for the flight conditions.
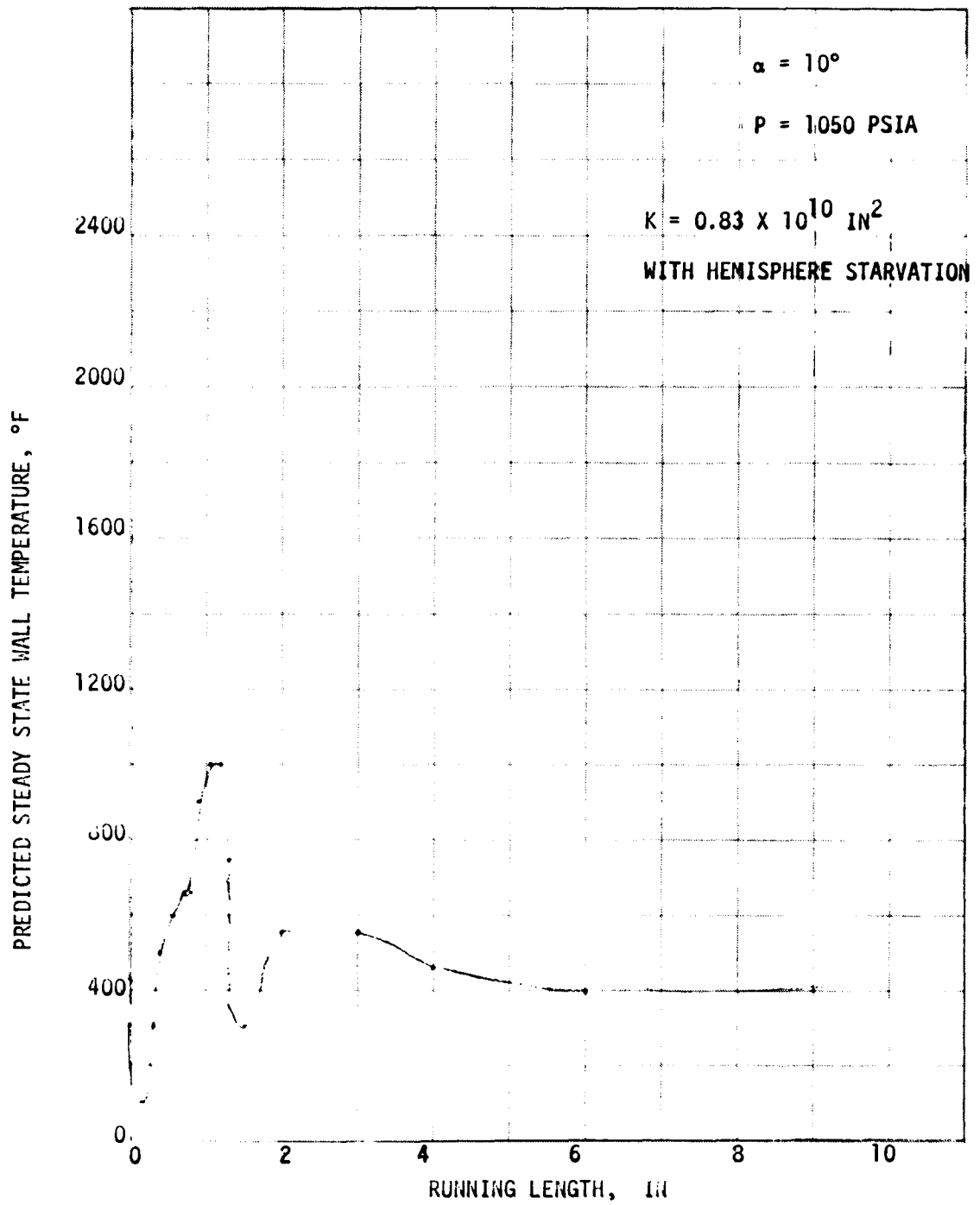
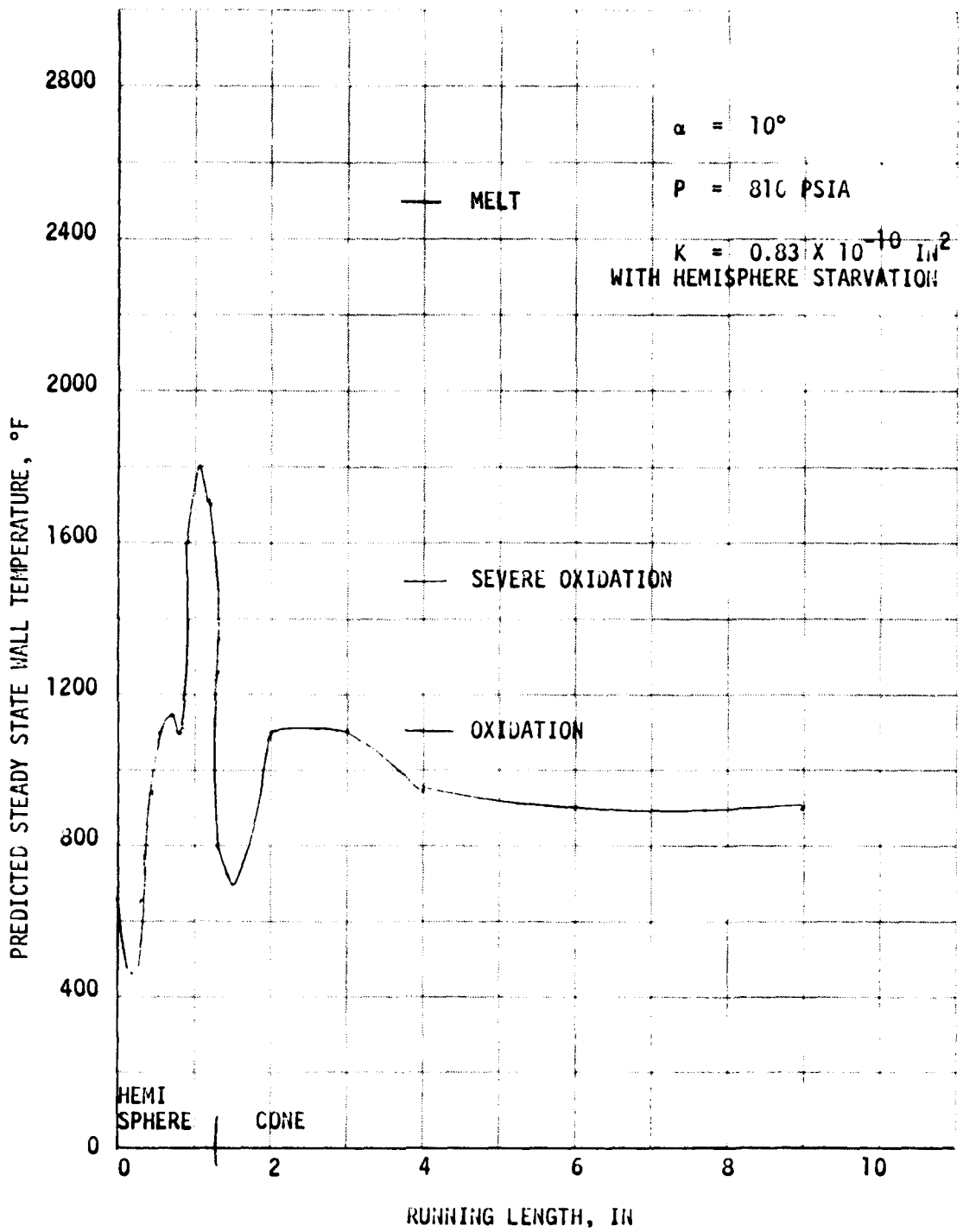Figure 9-18. Nosetip Temperature Distribution - 1050 psia

88

Figure 9-19.   AMMRC TCNT Test 2 – W = 2.25 lb/sec
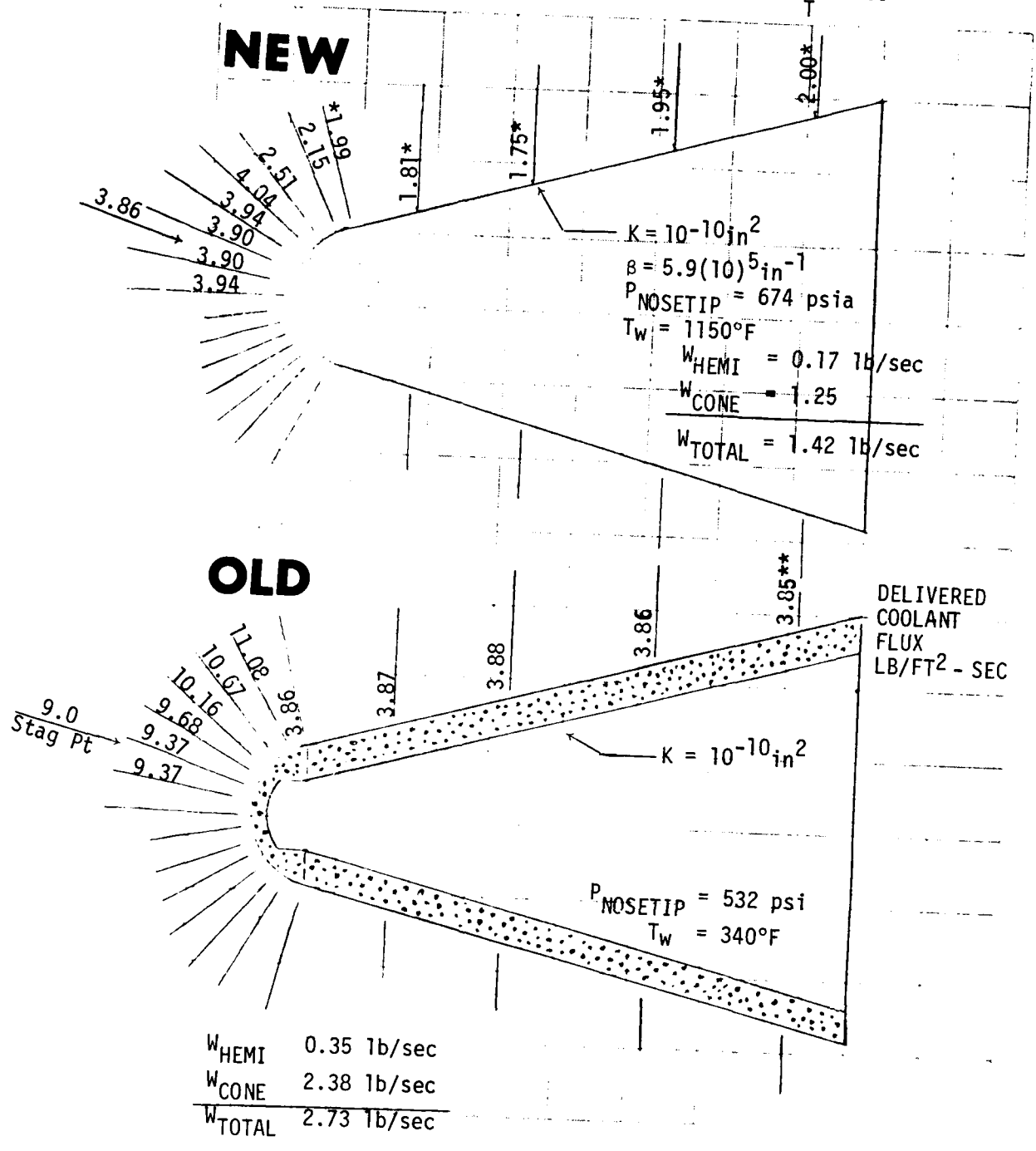
$u = 10$ KFT/SEC
$\alpha = 15°$
$h = 50$ KFT
$RE_T = 100$

NEW

$*1.99$
2.15
4.04
3.94
3.86
3.90
3.90
3.94

$1.81*$
$1.75*$
$1.95*$
$2.00*$

$K = 10^{-10}$ in^2
$\beta = 5.9(10)^5$ in^{-1}
$P_{NOSETIP} = 674$ psia
$T_W = 1150°F$
$W_{HEMI} = 0.17$ lb/sec
$W_{CONE} = 1.25$
$W_{TOTAL} = 1.42$ lb/sec

OLD

$3.85**$
3.86
3.88
3.87
11.08
10.67
10.16
9.68
9.37
9.37
3.98
9.0
Stag Pt

DELIVERED
COOLANT
FLUX
LB/FT^2 - SEC

$K = 10^{-10}$ in^2

$P_{NOSETIP} = 532$ psi
$T_W = 340°F$

W_{HEMI} 0.35 lb/sec
W_{CONE} 2.38 lb/sec
W_{TOTAL} 2.73 lb/sec

Figure 9-20.   Revised Flight Requirements

MCDONNELL DOUGLAS
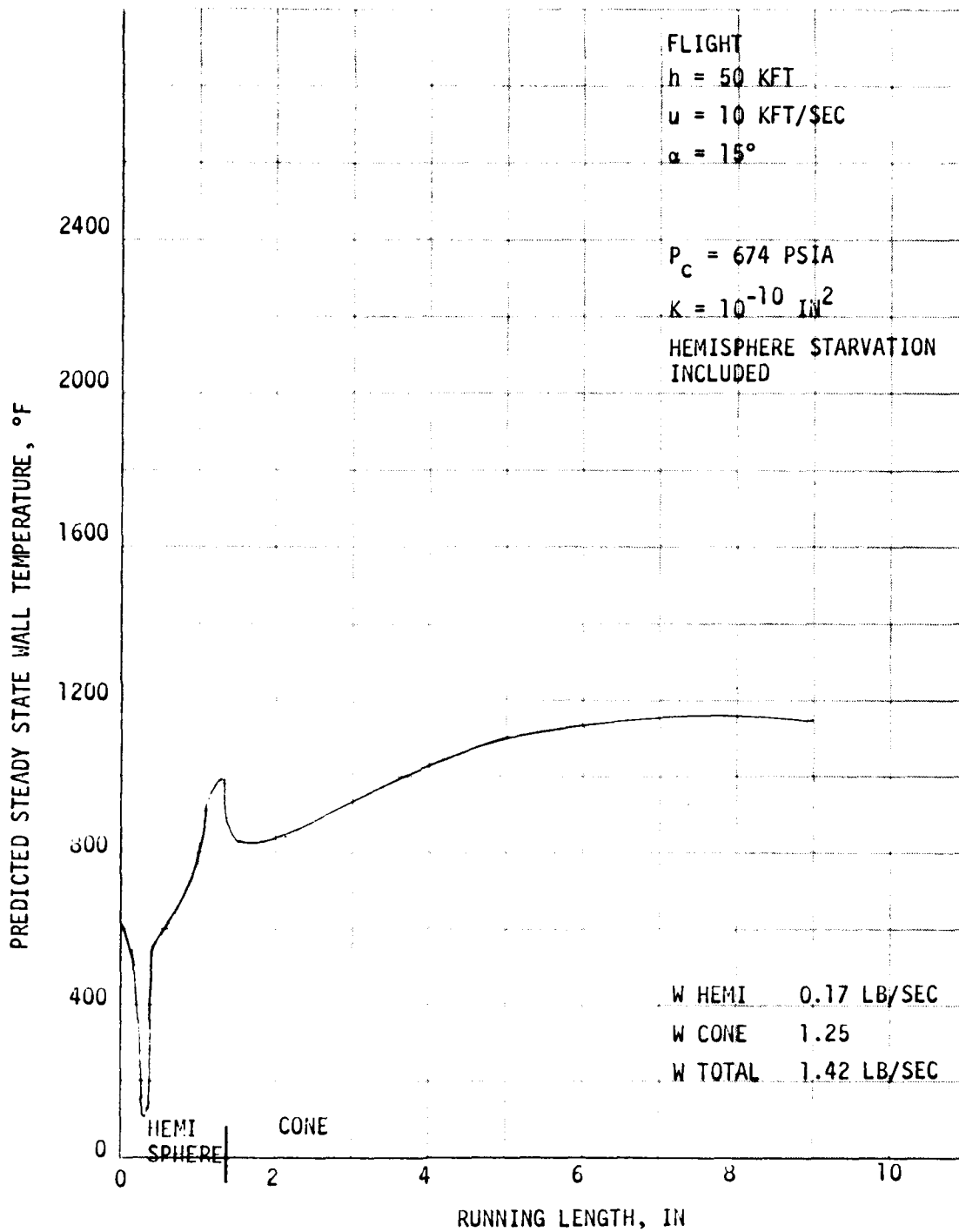
Figure 9-21. TCNT Flight Requirements

91

Section 10
CONCLUSIONS

The development program for a transpiration cooled nosetip applicable to endohoming interceptors was successful:

(1) The feasibility of manufacturing a large scale porous nosetip was demonstrated.

(2) The permeability range required for an endohoming nosetip was achieved. The nosetip designer has considerable flexibility in selection of permeability.

(3) Ground tests demonstrated nosetip survivability to 10° angle of attack. There is no reason to believe that higher angles of attack are not achievable.

(4) Ground tests demonstrated that the analytical model is adequate.

 ɔ) Ground tests demonstrated that the nosetip can be operated at nosetip surface temperatures in the oxidation regime of stainless steel.

MCDONNELL DOUGLAS

REFERENCES

2-1 Hoshizaki, H., "Heat Transfer in Planetary Atmosphere at Super-Satellite Speeds," ARS Journal, 32, 1544, October 1962.

2-2 Lees, Lester, "Laminar Heat Transfer Over Blunt-Nosed Bodies at Hypersonic Flight Speeds," Jet Propulsion, 26, 259, April 1956.

2-3 Detra, R. W. and H. Hidalgo, Generalized Heat Transfer Formulae and Graphs. ARCO Research Report 72, March 1960.

2-4 Arne, C. L. "Ablative Materials Subject to Combustion and Thermal Radiation Phenomena," Douglas Paper 1852, January 1964.

2-5 "Maneuvering Re-entry Control and Ablation Studies (MARCAS) Final Report," Vol. III, BSD-TR-65-312, July 1965.

2-6 Rosenwasser, S. N. et al, "Development of Porous Beryllium," AFML-TR-71-241, January 1972.

MCDONNELL DOUGLAS

PRECEDING PAGE BLANK-NOT FILMED

Appendix A

316L STAINLESS STEEL POWDER SPECIFICATION

PRECEDING PAGE BLANK-NOT FILMED

POWDER, 316L STAINLESS STEEL

1. SCOPE

1.1 Scope – This specification establishes the minimum requirements for one type and grade of 316L stainless steel powder for use in preparation of porous stainless steel parts.

1.2 Requirements identification number – This specification shall be called out on design drawings by means of the requirements identification number consisting of the ST specification number followed by the suffix 01.

Example of requirements identification number:

STM0543-01 ⎵—— Suffix

2. APPLICABLE DOCUMENTS

2.1 Government-furnished documents – The following documents (and subsidiaries thereof) of issue in effect on date of invitation for bid, unless otherwise indicated, form a part of this specification to the extent specified herein.

SPECIFICATIONS

    FEDERAL

PPP-B-601	Boxes, Wood, Cleated-Plywood
PPP-B-621	Box, Wood, Nailed and Lock-Corner
PPP-B-636	Box, Fiberboard
PPP-P-704	Pails: Shipping, Steel (1 through 12 gallons)

STANDARDS

    FEDERAL

Federal Test Method Standard No. 151	Metals; Test Methods

Copies of specifications, standards, drawings and publications required by contractors in connection with specific procurement functions should be obtained from the procuring activity or as directed by the contracting activity.

REVISION A 6 NOVEMBER 1978
APPROVAL DATE 20 AUGUST 1969

PROCUREMENT SPECIFICATION	TITLE	CLASSIFICATION
NONE	POWDER, 316L STAINLESS STEEL	MATERIAL SPECIFICATION
		STM0543 SHEET 1 of 7

2.2 <u>Other publications</u> - The following publications (and subsidiaries thereof) form a part of this specification to the extent specified herein. Unless otherwise specified, the issue in effect on date of invitation for bid shall apply.

AMERICAN SOCIETY FOR TESTING AND MATERIALS

ASTM B212	Standard Methods of Test for Apparent Density of Metal Powders
ASTM B214	Standard Methods of Test for Sieve Analysis of Granular Metal Powders
ASTM B215	Standard Methods of Sampling Finished Lots of Metal Powders
ASTM E11	Wire-Cloth Sieves for Testing Purposes

(Application for copies of ASTM standards should be addressed to the American Society for Testing and Materials, 1916 Race Street, Philadelphia, Pennsylvania 19103.)

3.   REQUIREMENTS

3.1 <u>Qualification</u> - The material furnished shall be a product that has been tested and has passed the qualification tests specified herein. The qualification testing need not be accomplished for repeat orders, provided the materials and process have not been changed and a certified statement to this effect is furnished to the procuring activity.

3.2 <u>Manufacturing method</u> - The powder shall be manufactured by using a high pressure water atomization process. Nitrogen gas or its equivalent shall be used in the atomization chamber to minimize oxidation of the powder.

3.3 <u>Chemical composition</u> - The chemical composition of the as-received powder shall meet the requirements of Table I, and shall be rechecked after powder classification to verify compliance with Table I.

CODE IDENT 18355   APPROVAL DATE   20 AUGUST 1969   REVISION A)   6 NOVEMBER 1978

TABLE I

CHEMICAL COMPOSITION OF TYPE 316L POWDER

ELEMENT	PERCENT
Carbon	0.03 max
Chromium	16.0 - 18.0
Nickel	10.0 - 14.0
Molybdenum	2.0 - 3.0
Manganese	0.40 max
Silicon	1.0 max
Phosphorus	0.04 max
Sulfur	0.03 max
Oxygen	0.30 max
Nitrogen	0.05 max
Iron	Remainder

3.4 **Powder size** - Nominal powder size shall be designated using U.S. standard mesh size numbers or given in micron size range with the powder complying in size distribution with Table II. A powder size distribution other than that shown may be acceptable depending on the desired use of the powder.

TABLE II

TYPE 316L POWDER SIZE SCREENING TOLERANCES

NOMINAL POWDER SIZE		PERCENT RETAINED	
MESH SIZE	MICRON SIZE	-200	-325
+200	+74	Remainder	
+230 -200	+63 -74	10 min.	
+325 -230	+44 -63	20 min.	Remainder
	+25 -44	20 min.	35 min.
	+7 -25	10 min.	20 min.
	-7	Remainder	Remainder

3.5 **Apparent density** - The apparent density of the powder shall be within the range of 2.6 to 2.9 grams per cubic centimeter for -200 powder and 2.9 to 3.3 grams per cubic centimeter for -325 mesh powder.

STMU543

OO-1733-02 (17 MAR 72)

3.6 Powder shape - The shape of the powder shall be similar to that shown in Figure 1. The powder should consist of a combination of smooth, round, and oblong-shaped particles intermixed with numerous irregular particles.
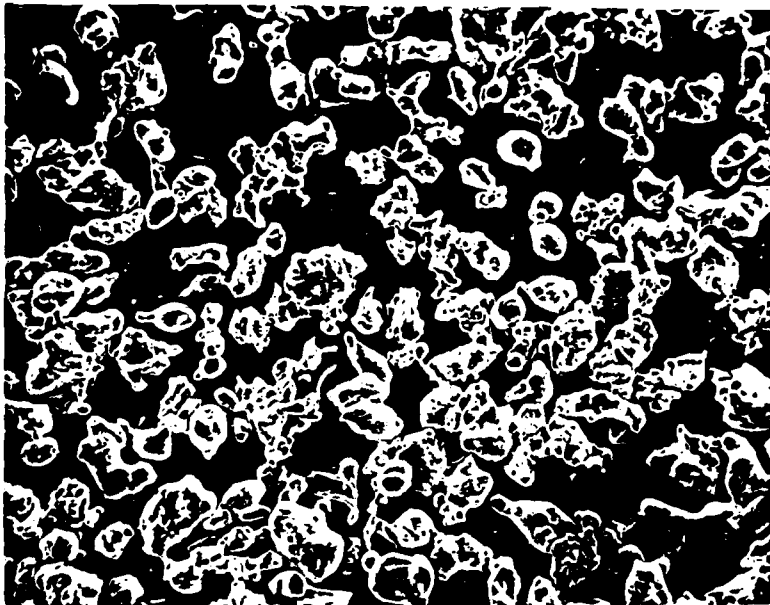
Mag: 200X

FIGURE 1.   SEM PHOTOGRAPH OF TYPE 316L POWDER

3.7 Powder heat treatment and microstructure - The powder shall be in the annealed condition and have a microstructure indicative of material that was rapidly cooled from a melt, as shown in Figure 2.
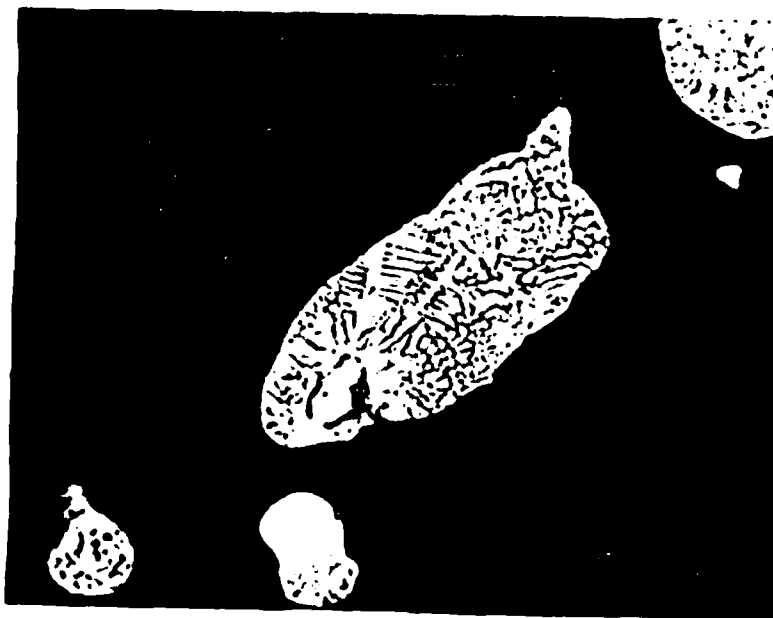
Mag: 1040X

FIGURE 2.   MICROSTRUCTURE OF TYPE 316L POWDER

STM0543

DD-1739-02 (17 MAR 72)

3.8 <u>Workmanship</u> - The powder shall be uniform in appearance and quality. It shall be dry, clean, and free of all contaminants detrimental to its intended use in fabrication of porous stainless steel parts.

4. <u>QUALITY ASSURANCE PROVISIONS</u>

4.1 <u>Inspection responsibility</u> - The supplier is responsible for the performance of all inspection requirements as specified herein. Except as otherwise specified, the supplier may utilize his own or any other inspection facilities and services acceptable to the procuring activity. Inspection records of the examination and tests shall be kept complete and available to the procuring activity as specified in the contract or order. The procuring activity reserves the right to perform any of the inspections set forth in this specification where such inspections are deemed necessary to assure that material and process conform to the prescribed requirements.

4.2 <u>Lot</u> - For purposes of sampling, inspection, and tests, a lot shall consist of all containers of a given lot number of powder submitted for acceptance at one time.

4.3 <u>Sampling</u> - Samples shall be taken in accordance with ASTM B215.

4.4 <u>Classification of tests</u>

4.4.1 <u>Qualification tests</u> - Qualification tests are those tests which enable the procuring agency to determine that the material complies with the specification requirements. The qualification tests consist of all inspections and tests included in Section 4, except the inspection of packaging.

4.4.2 <u>Quality conformance tests</u> - Quality conformance tests are those tests and examinations which shall be conducted by the supplier to assure continuing compliance with the requirements of this specification and enable the supplier to certify the conformance of his product to the procuring activity.

Test	Paragraph
(a) Chemical analysis	4.5.1
(b) Powder size screening test	4.5.2
(c) Apparent density	4.5.3
(d) Examination	4.6

4.5 <u>Test methods and procedures</u>

4.5.1 <u>Chemical analysis</u> - Chemical composition shall be determined in accordance with Federal Test Method Standard No. 151, Method 111.2 for compliance to the requirements of Table I.

CODE IDENT 76301 APPROVAL DATE 20 AUGUST 1969 REVISION (A) 6 NOVEMBER 1978

4.5.2 <u>Powder size screening test</u> - Size distribution shall be determined by using either sieves per ASTM E11, an air classification system, or a laser Microtrac system. Sieve analysis using a sieve shaker shall be performed per the methods of ASTM B214 for compliance to the requirements of Table II.

4.5.3 <u>Apparent density</u> - The apparent density shall be determined in accordance with ASTM B212 for compliance to the requirements of 3.5.

4.5.4 <u>Powder shape</u> - The powder shape shall be determined by using a Scanning Electron Microscope (SEM) or equivalent technique for compliance to the requirements of 3.6.

4.5.5 <u>Microstructure</u> - The microstructure of the powder shall be determined using metallographic techniques for compliance to the requirements of 3.7.

4.6 <u>Examination</u>

4.6.1 <u>Inspection of product</u> - Each lot of powder shall be inspected to determine conformance to the requirements of 3.2 and 3.8.

4.6.2 <u>Inspection of packaging</u> - The supplier shall make such inspections as are necessary to assure that the requirements for preservation, packaging, packing, and marking are met.

5. <u>PREPARATION FOR DELIVERY</u>

5.1 <u>Preservation and packaging</u>

5.1.1 <u>Level A</u> - The powder shall be packaged in PPP-P-704, Type II, Class 3 steel pails, utilizing polyethylene bag liners when net weight exceeds 50 pounds.

5.1.2 <u>Level C</u> - The powder shall be preserved and packaged in a manner that will afford protection against deterioration, contamination, and physical damage during shipment from supply source to the first receiving activity.

5.1.3 Unless otherwise specified in the contract or order, Level A preservation and packaging shall be provided.

5.2 <u>Packing</u>

5.2.1 <u>Level A</u> - Powder packaged per 5.1.1 shall be packed in containers meeting Level A requirements of PPP-B-636, PPP-B-601, or PPP-B-621.

5.2.2 <u>Level C</u> - Packages which require overpacking for acceptance by common carriers shall be packed in uniform quantities in a manner to assure carrier acceptance at the lowest freight rates and to assure safe delivery from the supply source to the first receiving activity.

OS-1732-02 (17 MAR 72)

5.2.3 Unless otherwise specified in the contract or order, Level A packing shall be provided.

5.3 <u>Marking</u> - All containers shall be marked in accordance with the requirements of applicable federal and state shipping regulations.

5.3.1 <u>Non-governmental agencies</u> - Unit, intermediate, and shipping containers shall be durably and legibly marked with the following information:

    (a) Number, suffix and change letter of this specification

    (b) Order number

    (c) Manufacturer's name and product designation

    (d) Lot or batch number

    (e) Date of manufacture

    (f) Quantity

6.   <u>NOTES</u>

6.1 <u>Intended use</u> - The material described in this specification is intended for fabrication of porous metal parts for use in missiles and space vehicles.

6.2 <u>Ordering data</u> - Orders or contracts should specify the following information:

    (a) Title, number, suffix and change letter of this specification

    (b) Quantity of material

    (c) Level of packaging and packing required

    (d) Test report required, listing chemistry, particle distribution, and apparent density of powder. Chemistry to include oxygen, nitrogen, and manganese content.

No. of Copies

Commander
U.S. Army Materiel Development and Readiness Command   1
ATTN: DRCLDC, Office of Laboratory Management,
       R. Gonano
5001 Eisenhower Avenue
Alexandria, VA 22333

Ballistic Missile Defense Program Office
ATTN: DACS-BMT   1
5001 Eisenhower Avenue
Alexandria, VA 22333

Director
Ballistic Missile Defense Advanced Technology Center
ATTN: W. Davis   1
      J. Carlson   1
      Col. J. W. Gillespie   1
      W. Davies   1
      D. Harmon   1
      J. Papadopoulos   1
      S. Brockway   1
      M. Whitfield   1
P.O. Box 1500
Huntsville, AL 35807

Ballistic Missile Defense Systems Technology Program
ATTN: J. Katechis   1
      E. Martz   1
P. O. Box 1500
Huntsville, AL 35807

Commander
U.S. Army Ballistic Missile Defense Systems Command
ATTN: N. J. Hurst   1
P. O. Box 1500
Huntsville, AL 35807

Commander
U.S. Army Missile Reseach and Development Command
ATTN: DRDMI-EAM, W. K. Patterson   1
Redstone Arsenal
Huntsville, AL 35809

Director
Defense Nuclear Agency
ATTN: SPAS, D. Kohler   1
      SPAS, Lt. J. Sommers   1
Washington, DC 20305

MCDONNELL DOUGLAS

PRECEDING PAGE BLANK-NOT FILMED

Office of Deputy Under Secretary of Defense
for Research and Engineering (ET)
ATTN: J. Persh, Staff Specialist for   1
      Materials and Structures
The Pentagon, Room 3D1089
Washington, DC 20301

Office of Deputy Chief of Research Development
and Acquisition
ATTN: DAMA-CSS, J. Bryant   1
The Pentagon, Room 3D424
Washington, DC 20310

Commander
Harry Diamond Laboratories
ATTN: DRXDO-NP, F. Wimenitz   1
      DRXDO-NP, J. Gwaltney   1
2800 Powder Mill Road
Adelphi, MD 20783

Commander
Air Force Flight Dynamics Laboratory
ATTN: AFFDL/FBC, H. A. Wood   1
Wright-Patterson Air Force Base, OH 45433

Commmander
U.S. Army Combat Development Command
Institute of Nuclear Studies
ATTN: Technical Library   1
Fort Bliss, TX 79916

Commander
AFWAL Materials Laboratory
Air Force Systems Command
ATTN: W. Kessler   1
      H. Materne   1
      D. Schmidt   1
      G. Schmitt   1
Wright-Patterson Air Force Base, OH 45433

Commander
BMO/ABRES Office
ATTN: BMO/MNTR, Col. R. Smith   1
      BMO/MNRTE, Maj. J. Sikra   1
      BMO/MNRTE, Maj. K. Yelmgren   1
Norton Air Force Base, CA 92409

Commander
Naval Sea Systems Command
ATTN: ORD-03331, M. Kinna   1
Washington, DC 20360

Commander
Naval Surface Weapons Center
ATTN: W. Carson Lyons   1
      C. Rowe   1
      R. Feldhuhn   1
      W. Messick   1
Silver Springs, MD 20910

Sandia Laboratories
ATTN: J. K. Cole   1
P.O. Box 5800
Albuquerque, NM 87115

Aerospace Corporation
ATTN: W. Riley   1
      R. Meyers   1
      L. Rubin   1
P.O. Box 92957
Los Angeles, CA 90009

Aerotherm Acurex Corporation
ATTN: J. Arnold   1
485 Clyde Avenue
Mountain View, CA 94042

AVCO Systems Division
ATTN: P. G. Rolincik   1
201 Lowell Street
Wilmington, MA 01887

Battelle Columbus Laboratories
ATTN: B. Noton   1
505 King Avenue
Columbus, OH 43201

Boeing Aerospace Company
ATTN: M. Kushner   1
P.O. Box 3999
Seattle, Washington 98124

Effects Technology, Inc.
ATTN: R. Wengler   1
      J. Green   1
5383 Hollister Avenue
Santa Barbara, CA 93111

Fiber Materials, Inc.
ATTN: L. Lander   1
      G. Williams   1
Biddeford Industrial Park
Biddeford, ME 04005

MCDONNELL DOUGLAS

General Dynamics Corporation
Convair Division
ATTN: J. Hertz   1
5001 Kearny Villa Road
San Diego, CA 92138

General Electric Company
Advanced Materials Development Laboratory
ATTN: P. Gorsuc, Room 4466   1
      J. Brazel, Room 4466   1
3198 Chestnut Street
Philadelphia, PA 19101

Hughes Aircraft Company
ATTN: R. W. Jones   1
Centinela and Teale Streets
Culver City, CA 90230

Lockheed Missiles and Space Company
Palo Alto Research Laboratory
ATTN: E. C. Burke   1
      D. Aspinwall   1
      T. Tietz   1
Dept. 5230, Bldg. 201
3251 Hanover Street
Palo Alto, CA 94304

Lockheed Missiles and Space Company
ATTN: D. Kenworty   1
      A. Mietz   1
      M. Jacobson   1
P.O. Box 504
Sunnyvale, CA 94088

Martin Marietta Corporation
ATTN: D. Easter   1
      L. Gilbert   1
      J. Madden   1
      G. Wannell   1
      V. Hewitt   1
      A. Ossin   1
      W. Spencer   1
      K. Hansen   1
P.O. Box 5837
Orlando, FL 32805

MCDONNELL DOUGLAS

McDonnell Douglas Astronautics Company
ATTN: N. Campbell   1
      F. Pittinato   1
      M. Martin   1
      A. Eykholt   1
      R. Fristoe   1
      W. Olson   1
      I. Richman   1
      R. Zemer   1
5301 Bolsa Avenue
Huntington Beach, CA 92647

New Technology, Inc.   1
Research Park
P.O. Box 5245
Huntsville, AL 35805

Prototype Development Associates
ATTN: J. Schutzler   1
1740 Garry Avenue, Suite 201
Santa Ana, CA 92705

R&D Associates
ATTN: A. Field   1
P.O. Box 9695
Marina de Rey, CA 90291

Science Applications, Inc.
ATTN: I. Osofsky   1
One Continental Plaza, Suite 310
101 Continental Blvd.
El Segundo, CA 90245

Science Applications, Inc.
ATTN: K. Kratsch   1
18872 Bardeen Avenue
Irvine, CA 92715

Southwest Research Institute
ATTN: A. Wenzel   1
8500 Culebra Road
San Antonio, TX 78206

Terra Tek, Inc.
ATTN: A. H. Jones   1
University Research Park
420 Wakara Way
Salt Lake City, Utah 84108

TRW Defense and Space Systems
ATTN: L. Berger   1
P.O. Box 1310
San Bernardino, CA 92402

Defense Docmentation Center   1
Cameron Station, Bldg. 5
5010 Duke Station
Alexandria, VA 22314

Director
Army Materials & Mechanics Research Center
ATTN: DRXMR-H, J. F. Dignam   1
      DRXMR-H, L. R. Aronin   2
      DRXMR-H, S. C. Chou   1
      DRXMR-AP   1
      DRXMR-PL   1
      DRXMR-PR   2
Watertown, MA 02172

MCDONNELL DOUGLAS

Army Materials and Mechanics Research Center,
Watertown Massachusetts 02172
TRANSPIRATION-COOLED NOSETIP
DEVELOPMENT - N. C. Campbell,
M. T. Martin, G. F. Pittinato

Technical Report AMMRC TR 80-30, August 1980, 112 pp -
illus-table, D/A Project 1W162113A661
AMCMS Code 62113.11 07000

A 316L stainless steel transpiration-cooled nosetip for a high-performance missile system was designed and fabricated using powder metallurgy techniques. The geometry of the nosetip was established, and permeability requirements were analytically defined. A parametric study of subscale billets determined permeability as a function of powder size and sintering temperature. Near-netshape billets were fabricated, and machining procedures for the porous material were established. A comparison was made between the actual and calculated gas flow through the nosetip over its entire surface. Two nosetips were successfully tested in a thermal environment approximating the flight environment at the Edward's Air Force Base Rocket Propulsion Laboratory (RPL). Tests were conducted at 0-degree and 10-degree angles of attack.

AD ___

Army Materials and Mechanics Research Center,
Watertown Massachusetts 02172
TRANSPIRATION-COOLED NOSETIP
DEVELOPMENT - N. C. Campbell,
M. T. Martin, G. F. Pittinato

UNCLASSIFIED
UNLIMITED DISTRIBUTION

Key Words

Nosetips   Fabrication
Cooling   Interceptors
            Transpiration

Technical Report AMMRC TR 80-30, August 1980, 112 pp -
illus-table. D/A Project 1W162113A661
AMCMS Code 62113.11 07000

A 316L stainless steel transpiration-cooled nosetip for a high-performance missile system was designed and fabricated using powder metallurgy techniques. The geometry of the nosetip was established, and permeability requirements were analytically defined. A parametric study of subscale billets determined permeability as a function of powder size and sintering temperature. Near-netshape billets were fabricated, and machining procedures for the porous material were established. A comparison was made between the actual and calculated gas flow through the nosetip over its entire surface. Two nosetips were successfully tested in a thermal environment approximating the flight environment at the Edward's Air Force Base Rocket Propulsion Laboratory (RPL). Tests were conducted at 0-degree and 10-degree angles of attack.